國立交通大學

電子工程學系　　電子研究所

碩 士 論 文

快速計算的二維反轉層模擬器

A Fast Quantum Simulator for the Two-Dimensional Inversion Layers

研究生: 鄭寬豪 Kuan-Hao Cheng

指導教授: 陳明哲 博士 Prof. Ming-Jer Chen

中華民國 九十九 年 九 月

快速計算的二維反轉層模擬器

研究生: 鄭寬豪　　指導教授: 陳明哲 博士

國立交通大學

電子工程學系 電子研究所碩士班

摘要

在 N 型金屬氧化物場效電晶體，非均勻的運算格子間距中，透過牛頓-里曼的疊帶法來解薛丁格和波松方程式自洽。這目的是為了在奈米元件中，模擬比三角位能井近似來的更真實的物理環境，而模擬顯示與 Schred 軟體的結果是非常相近的。然而在 P 型金屬氧化物場效電晶體中，六層的 kp 模型在過去已經常被用在計算電洞的能帶與遷移率，包括應力與不同的晶向的效應。在此篇論文的研究中，我們介紹了一種新的模擬方法，透過 kp 的哈密爾敦矩陣來快速得到電洞的能帶結構。而為了確保我們研究的準確性，所以我們也建立了一個在反轉層中的簡單的遷移率模型，再進行在不同溫度下此模擬結果與實驗值比較。在這模型中我們考慮的機制有:聲學聲子散射、光學聲子散射與表面粗糙度散射。至於因為摻入雜質所產生的庫倫散射不在我們討論中。此外，我們也透過有效質量的方法，來萃取量子化的等效質量，至於能態密度的等效質量也將會與低溫 Shubnikov-de Haas 震盪實驗的數據互相比較。

A Fast Quantum Simulator for the Two-Dimensional Inversion Layers

Student: Kuan-Hao Cheng Advisor: Dr. Ming-Jer Chen

Department of Electronics Engineering and Institute of Electronics

National Chiao Tung University

Abstract

Self-consistent solving of Schrődinger and Poisson equations in n-channel MOSFETs (metal-oxide-semiconductor field-effect transistors) is obtained by using Newton-Raphson iteration technique with the non-uniform mesh arrangement. The method is applied to simulate more realistic physical environment than triangular potential well approximation in nano devices. The simulation results show excellent agreements with Schred's. However, in p-channel MOSFETs, a six-band $k \cdot p$ model has been used to calculate hole subband structure and mobility for different surface orientations and different strains. In this work, we introduce a new efficient model based on six-band $k \cdot p$ Hamiltonian to rapidly obtain accurate hole properties. In order to ensure the validity of our work, we build an effective mobility model in the hole inversion layer and compare the results with the experimental data concerning the *universal curves* at different temperatures. The different scattering mechanisms are included in this study: acoustic phonon scattering, optical phonon scattering and surface roughness scattering. To focus on the high surface field region, Coulomb scattering due to ionized impurities will be ignored. In addition, with the use of an equivalent effective mass model, the extracted quantization effective mass and density of states effective mass will be compared with low temperature (2 K) Shubnikov-de Haas oscillation experiment results published in the literature.

Acknowledgements

光陰似箭、時間飛逝之快，真讓我措手不及。兩年一下子就過去了，當初懵懵懂懂的進入交通大學，滿腔熱血地希望在這研究所的兩年可以有所蛻變，現在回想起來，我應該有所改變吧。這邊要感謝實驗室的大家長，陳明哲老師，當初大膽的決定讓我加入 Nano Electronics Physics (NEP) 實驗室，從一個完全不懂固態的學生到今天還是不很了解半導體物理的畢業生，希望老師不會太指責。畢竟想徜徉在這半導體的大海裡，除了有 NEP 這大船與船長之外，自己也需要非常的努力。再者，也要感謝實驗室李建志(阿志)博士班學長，因為有他，我才能站在他的肩膀上，一窺半導體的世界，對於這世界，我就像小孩一般有十萬個為什麼，而阿志學長卻能細心地解答我的疑問，讓我有不一樣的想法與見識，有今天的成就要多半感謝他的幫忙。而實驗室博士班學長，許志育(許博)、李韋漢(dorun)，也常常讓我問一些奇奇怪怪的問題，真的是不好意思。至於同屆的詹益先、蔡濬澤、張華罡，有他們三個平常與我打打鬧鬧，在有壓力的研究生活裡也充滿一些樂趣。另外學弟妹，彭霖祥、張洛豪、光心君、林煜翔也謝謝他們常常幫我處理一些雜事。還有與一起共事的研究助理張碩榮，也常常幫我解答半導體上的諸多疑問，其功勞也不小於阿志學長。另外特別感謝口試委員，林鴻志老師與張智勝經理，提醒我論文上的一些缺失與研究上的問題，讓我的畢業論文更趨於完善。最後要感謝我的父母親有他們才有今天的我，我大哥鄭銘龍先生，以過來人的身分提醒我，我女朋友鐘翊瑄小姐，忍受我研究時情緒的不耐煩，還有我學弟沈佑任，陪我去運動聊天。太多太多人要感謝了，最後就感謝老天讓我順利畢業。

Contents

Figure Captions

Figure 3.4.1 Impurity ionization rate and band diagram at extremely low temperature about 2 K.

Figure 5.9. Subband energy (a) and equienergy lines (b)-(d) in the lowest –lying HH, LH and SO subbands for the (001) surface compared with Fischetti's [3]. The doping concentration is 1×10^{17} cm^{-3} and temperature is 300 K. It is noticd that our subband energy is higher than Fischetti's about 15meV.

Figure 5.10. Subband energy (a) and equienergy lines (b) and (c) in the lowest –lying HH and LH subbands for the (011) surface compared with Fischetti's [3]. The doping concentration is 1×10^{17} cm^{-3} and temperature is 300 K.

Figure 5.11. Subband energy (a) and equienergy lines (b) and (c) in the lowest –lying HH and SO subbands for the (111) surface compared with Fischetti's [3]. The doping concentration is 1×10^{17} cm^{-3} and temperature is 300 K. It notices that our subband energy is higher than Fischetti's [3] about 10meV.

Figure 5.12. Energy of the subbands (a) and equienergu lines (b) in the lowest-lying HH, LH and SO subbands for the (100) surface with 1% of tensile in-plane stress applied on the (x,y) plane. It notices that our subband energy is higher than Fischetti's [3] about 20meV.

Figure 5.13. Energy of the subbands (a) and equienergu lines (b) in the lowest-lying HH, LH and SO subbands for the (100) surface with 1% of compressive in-plane stress applied on the (x,y) plane. It notices that our subband energy is higher than Fischetti's [3] about 25meV.

Figure 5.14. Energy of the subbands for the (001) surface by our new model compared with Michielis's simulation results [15].

Table Captions

Chapter 1

Introduction

In more recent years, the MOSFETs (metal-oxide-semiconductor field-effect transistors) technology has undergone a scaling-down strategy. When the device gate length shrinks towards about nanometers or below, the MOSFET scaling rule is rapidly invalid. The reasons are that the quantum effect plays an important role in nano device, and must be taken into account.

Firstly, this work demonstrates the full self-consistent method for solving Schrodinger equation and Poisson equations in n-channel MOSFET. The simulation results have been compared well with Schred [1]. On the other hand, more challenging issues have been devotes to the pMOS transistors in terms of the mobility and its dependent on wafer orientation and strain engineering. Several researchers have significantly addressed the two dimensional hole behaviors (See Figure 1.1), such as Tompson's group [2] and Fischetti, et al. [3], [4], along with the other theories, for example, the pseudo potential method, 4×4 $k\cdot p$ method, Monte Carlo simulation and full self consistent method. Figure 1.2 is highlighted to describe the efficiency and accuracy for above cases. We introduce the two methods to deal with the hole gas in the inversion layer; one is to utilize the triangular potential approximation based on Fischetti's skill and the other, Nano Electronics Physics (NEP) simulator, is the proposed new and computational efficient technique with two motivations: to avoid spending too much calculation time through the self-consistent method and to simulate the operation conditions under very low temperature. Finally, we extract the density of states effective mass and compare it with cyclotron effective mass at 2 K [5], as well as and building a correct hole effective mobility model along with comparing with experimental data [6] at different temperatures.

Chapter 2

Numerical Technique and Physical Theory

2.1 Time-independent Schrödinger Equation: Matrix Techniques

It is well-recognized that the time-independent Schrödinger equation in the quantum mechanics can be expressed in terms of a matrix equation:

$$-\frac{\hbar^2}{2m}\nabla^2\Psi + V\Psi = E\Psi \quad . \tag{2.1.1}$$

This approach is widely adopted in the band-structure simulation when it is focused on bound or quasi-bound states in a spatially varying potential V inside the highly scaled semiconductor devices. Let us assume that the wave-function Ψ is confined in a small region of W. We divide this region into ℓ intervals of the equal-distance $\Delta x = W/\ell$. The ith mesh point is indexed as x_i. In general, the wave-function Ψ we are looking for can be expanded by an orthogonal basis set $\{\psi_n\}$

$$\Psi = \sum_n a_n \psi_n \,, \tag{2.1.2}$$

where the ψ_n is the normalized wave-function at the mesh point x_n and the existing probability of ψ_n is exactly zero outside the interval n. According to Eq. (2.1.1), the Schrödinger equation in the confined direct can be written numerically as

$$-\frac{\hbar^2}{2m}\left[\frac{\Psi(x-\Delta x) - 2\Psi(x) + \Psi(x+\Delta x)}{\Delta x^2}\right] + V(x)\Psi(x) = E\Psi(x) \,. \tag{2.1.3}$$

Substituting Eq. (2.1.2) into Eq. (2.1.3), we get a set of ℓ equations (we are assuming $a_0 = a_{\ell+1} = 0$, i.e., the wave-function is localized in the space W). After taking the outer product of $\psi_1, \psi_2, \psi_3, \ldots \psi_\ell$, the matrix form of the one

dimensional Schrödinger equation is presented by

$$\begin{bmatrix} A_{(x_1)} & B & 0 & \cdots & 0 \\ B & A_{(x_2)} & B & & 0 \\ 0 & B & A_{(x_3)} & B & \vdots \\ \vdots & & & \ddots & 0 \\ 0 & \cdots & 0 & B & A_{(x_\ell)} \end{bmatrix} \bullet \begin{bmatrix} a_1\psi_1 \\ a_2\psi_2 \\ \vdots \\ \vdots \\ a_n\psi_\ell \end{bmatrix}_{\ell\times 1} = 0 \qquad (2.1.4)$$

with

$$A_{(x_i)} = \frac{\hbar^2}{m(\Delta x)^2} + V(x_i) - E\,, \qquad (2.1.5)$$

$$B = -\frac{\hbar^2}{2m(\Delta x)^2}. \qquad (2.1.6)$$

Obviously, Eq. (2.1.4) turns the complex differential Schrödinger equation into a common eigen-value problem and we will get the ℓ eigen-values corresponding to the ℓ eigen-function. The smallest eigen-value refers to the ground state while the others refer to the excited states.

2.2 Six-band $k \cdot p$ Calculation for the Hole Subband Structure in p-channel MOSFETs: Strain and Surface Orientation Effects

2.2.1 Strained Quantum Simulation

By following the theoretical work by Fischetti, et al. [3], a six-band silicon $k \cdot p$ method, along with the solving of Schrödinger equation in a triangular potential well beneath the gate oxide of bulk p-MOSFET, will be employed here. In this simulation framework, we solve the wave equation:

$$\left[H_{\text{kp}}(k_x, k_y, k_z = -i\frac{d}{dz}) + qV(z) \right] \cdot \xi_{k_x,k_y}(z) = E(k_x, k_y) \cdot \xi_{k_x,k_y}(z). \qquad (2.2.1.1)$$

Here, the surface potential $V(z)$ is equal to the minus of the surface electric field F_s

times the depth from the silicon surface z; and the $k \cdot p$ Hamiltonian H_{kp} is the Luttinger-Kohn Hamiltonian H_{LK} plus the strain Hamiltonian H_{strain}. Those expressions are given in [2]. Therefore, the 6×6 Hamiltonian is given by

$$H_{kp} = H_{LK} + H_{strain} = \begin{bmatrix} -P-Q & L & -M & 0 & \frac{1}{\sqrt{2}}L & -\sqrt{2}M \\ L^{+} & -P+Q & 0 & -M & \sqrt{2}Q & -\sqrt{\frac{3}{2}}L \\ -M^{+} & 0 & -P+Q & -L & -\sqrt{\frac{3}{2}}L^{+} & -\sqrt{2}Q \\ 0 & -M^{+} & -L^{+} & -P-Q & \sqrt{2}M^{+} & \frac{1}{\sqrt{2}}L^{+} \\ \frac{1}{\sqrt{2}}L^{+} & \sqrt{2}Q^{+} & -\sqrt{\frac{3}{2}}L & \sqrt{2}M & -P-\Delta & 0 \\ -\sqrt{2}M^{+} & -\sqrt{\frac{3}{2}}L^{+} & -\sqrt{2}Q^{+} & \frac{1}{\sqrt{2}}L & 0 & -P-\Delta \end{bmatrix}, \quad (2.2.1.2)$$

where

$$\begin{aligned} P &= P_k + P_\varepsilon \\ Q &= Q_k + Q_\varepsilon \\ L &= L_k + L_\varepsilon \\ M &= M_k + M_\varepsilon \end{aligned}, \quad (2.2.1.3)$$

$$\begin{aligned} P_k &= \frac{\hbar^2}{2m_0}\gamma_1\left(k_x^2+k_y^2+k_z^2\right) \\ Q_k &= \frac{\hbar^2}{2m_0}\gamma_2\left(k_x^2+k_y^2-2k_z^2\right) \\ L_k &= \frac{\hbar^2}{m_0}\sqrt{3}\gamma_3\left(k_x-ik_y\right)k_z \\ M_k &= -\frac{\hbar^2}{2m_0}\sqrt{3}\left[\gamma_2\left(k_x^2-k_y^2\right)-2i\gamma_3 k_x k_y\right] \end{aligned} ; \quad \begin{aligned} P_\varepsilon &= -a_v\left(\varepsilon_{xx}+\varepsilon_{yy}+\varepsilon_{zz}\right) \\ Q_\varepsilon &= -\frac{b}{2}\left(\varepsilon_{xx}+\varepsilon_{yy}-2\varepsilon_{zz}\right) \\ L_\varepsilon &= -d\left(\varepsilon_{xz}-i\varepsilon_{yz}\right) \\ M_\varepsilon &= \frac{\sqrt{3}}{2}b\left(\varepsilon_{xx}-\varepsilon_{yy}\right)-id\varepsilon_{xy} \end{aligned} . \quad (2.2.1.4)$$

the P_k, Q_k, L_k and M_k are the $k\cdot p$ terms and the P_ε, Q_ε, L_ε and M_ε are the strain terms and Δ is the split-off energy. The Luttinger parameters γ_1, γ_2, γ_3 and strain deformation potentials a_v, b, d are both listed in Table I.

In the numerical calculation, the wave vector, k_z, is replaced by the operator,

$-i\frac{d}{dz}$, and the quantization z-direction length in the simulation is divided into a mesh of N_z points (N_z=101 in this work). Thus, Eq. (2.2.1.1) becomes the $6N_z \times 6N_z$ eigenvalue problem. Precisely speaking, this $6N_z \times 6N_z$ eigenvalue matrix can be expressed as the tridiagonal block form

$$\begin{bmatrix} \cdot & \cdot & \cdot & \cdot & \cdot & \cdot & \cdot \\ \cdot & D^- & D^0_{l-1} & D^+ & 0 & 0 & \cdot \\ \cdot & 0 & D^- & D^0_l & D^+ & 0 & \cdot \\ \cdot & 0 & 0 & D^- & D^0_{l+1} & D^+ & \cdot \\ \cdot & \cdot & \cdot & \cdot & \cdot & \cdot & \cdot \end{bmatrix} \begin{bmatrix} \cdot \\ \xi^{l-1}_{k_x,k_y} \\ \xi^{l}_{k_x,k_y} \\ \xi^{l+1}_{k_x,k_y} \\ \cdot \end{bmatrix} = E(k_x,k_y) \begin{bmatrix} \cdot \\ \xi^{l-1}_{k_x,k_y} \\ \xi^{l}_{k_x,k_y} \\ \xi^{l+1}_{k_x,k_y} \\ \cdot \end{bmatrix}, \qquad (2.2.1.5)$$

where each ξ_{k_x,k_y} is a six-component column vector. D^+, D^0 and D^- are 6×6 block-diagonal difference operators expressed as below

$$\begin{aligned} H_{kp} &= H_0 + H_1 \cdot k_z + H_2 \cdot k_z^2, \\ D^+ &= \frac{H_1}{2i\Delta z} - \frac{H_2}{(\Delta z)^2}, \\ D^0 &= H_0 + \frac{2H_2}{(\Delta z)^2}, \\ D^- &= -\frac{H_1}{2i\Delta z} - \frac{H_2}{(\Delta z)^2}. \end{aligned} \qquad (2.2.1.6)$$

The solving of Eq. (2.2.1.5) yields the same number of the eigenvalue matrices, $E(k_x,k_y)$, as well as the wave function $\xi_{kx,ky}(z)$.

2.2.2 Surface Orientation Effect

It is understood that in the $k\cdot p$ Hamiltonian, the appropriate rotations in k space is adopted to deal with (001), (110), and (111) surfaces [8] while $k_z \to \frac{-i\partial}{\partial z}$. For (110) surface, a rotation from the original (001) k space to (110) k' is required:

$$k_x^{'} = -k_z$$
$$k_y^{'} = \frac{1}{\sqrt{2}}(k_x - k_y), \qquad (2.2.2.1)$$
$$k_z^{'} = \frac{1}{\sqrt{2}}(k_x + k_y)$$

and similarly for (111) surface:

$$k_x^{'} = \frac{k_x}{\sqrt{6}} + \frac{ky}{\sqrt{6}} - \frac{2k_z}{\sqrt{6}}$$
$$k_y^{'} = \frac{1}{\sqrt{2}}(-k_x + k_y) \quad . \qquad (2.2.2.2)$$
$$k_z^{'} = \frac{k_x}{\sqrt{3}} + \frac{k_y}{\sqrt{3}} + \frac{k_z}{\sqrt{3}}$$

The coordinate rotations in k space as revealed by Eq. (2.2.2.1) and Eq. (2.2.2.2) revealing are shown in Figure 2.2.2.1.

2.2.3 Newton-Raphson Method

It is a well-known numerical analysis of the Newton-Raphson method (or Newton-Fourier method) for finding successively better approximations to the zeros (or roots) of a real-value function. Newton's method can converge remarkably quickly; especially if the iteration begins "sufficiently near" the desired root. First, see Figure 2.2.3.1, we start with an initial value, for example v_0, and look for the corresponding function of ***R***. And then, the function is approximated by its sloped line, and one computes the V-intercept of this tangent line (which is easily done with elementary algebra). This V-intercept will typically be a better approximation to the function's root than the original guess, and the method can be iterated. This iteration process can be expressed as

$$V_n = V_{n-1} - \Delta V \qquad (2.2.3.1)$$

$$\Delta V = \frac{R}{(\frac{\partial R}{\partial V})} \tag{2.2.3.2}$$

Now, we write the 1D Poisson's equation for $N \times N$ matrix case as below:

$$\frac{\partial^2 V}{\partial z^2} = -\frac{\rho}{\varepsilon}$$

$$\begin{bmatrix} -\frac{2}{\Delta z^2} & \frac{1}{\Delta z^2} & 0 & \cdots & 0 \\ \frac{1}{\Delta z^2} & -\frac{2}{\Delta z^2} & \frac{1}{\Delta z^2} & & 0 \\ 0 & \frac{1}{\Delta z^2} & -\frac{2}{\Delta z^2} & \frac{1}{\Delta z^2} & \vdots \\ \vdots & & & \ddots & 0 \\ 0 & \cdots & 0 & \frac{1}{\Delta z^2} & -\frac{2}{\Delta z^2} \end{bmatrix}_{N\times N} \bullet \begin{bmatrix} V_1 \\ V_2 \\ \vdots \\ \vdots \\ V_N \end{bmatrix}_{N\times 1} = \begin{bmatrix} \rho_1 \\ \rho_2 \\ \vdots \\ \vdots \\ \rho_N \end{bmatrix}_{N\times 1} \tag{2.2.3.3}$$

(2.2.3.4) and let $AV = \rho$, where $\boldsymbol{A}$ is second-order differential matrix, ρ is carrier charge density:

$$A = \begin{bmatrix} -\frac{2}{\Delta z^2} & \frac{1}{\Delta z^2} & 0 & \cdots & 0 \\ \frac{1}{\Delta z^2} & -\frac{2}{\Delta z^2} & \frac{1}{\Delta z^2} & & 0 \\ 0 & \frac{1}{\Delta z^2} & -\frac{2}{\Delta z^2} & \frac{1}{\Delta z^2} & \vdots \\ \vdots & & & \ddots & 0 \\ 0 & \cdots & 0 & \frac{1}{\Delta z^2} & -\frac{2}{\Delta z^2} \end{bmatrix}_{N\times N} \tag{2.2.3.5}$$

$$V = \begin{bmatrix} V_1 \\ V_2 \\ \vdots \\ \vdots \\ V_N \end{bmatrix}_{N\times 1} \tag{2.2.3.6}$$

$$\rho = \begin{bmatrix} \rho_1 \\ \rho_2 \\ \vdots \\ \vdots \\ \rho_N \end{bmatrix}_{N\times 1} . \qquad (2.2.3.7)$$

Finally, we apply Newton-Raphson method to solve Poisson and Schrődinger equations self-consistently. Therefore, we can hence express the Poisson equation as follows:

$$AV - \rho = R \qquad (2.2.3.8)$$

and differentiate the Eq. (2.2.3.7) by V, we can obtain the following:

$$A - \frac{\partial \rho}{\partial V} = \frac{\partial R}{\partial V} = NR \qquad (2.2.3.9)$$

and Eq. (2.2.3.2) can be rewritten as

$$\Delta V = \frac{R}{\frac{\partial R}{\partial V}} = \frac{R}{NR} \qquad (2.2.3.10)$$

2.4 Effective Mass Approximation (EMA) Algorithm

2.4.1 Introduction

It has been well recognized that in the context of the effective mass approximation (EMA), the motion of carriers in a crystal can be visualized and described in a quasi-classical manner. Considering the case in which one electron moves in a periodic potential firstly, the solutions of wave-functions can be written in the Bloch form $\psi_k(x) = e^{iKx}u_k(x)$ with the corresponding energy $E(k)$. In order to describe localized electrons, one may build a wave packet by linearly combining the group of Bloch wave-functions

$$\begin{aligned}\Psi(x,t) &= \sum_k A(k)\psi_k(x,t) \\ &= \sum_k A(k)\psi_k(x)e^{-i\frac{E(k)}{\hbar}t} \\ &= \sum_k A(k)u_k(x)e^{i\left(kx-\frac{E(k)}{\hbar}t\right)}.\end{aligned} \tag{2.4.1.1}$$

We expand the wave packet Ψ at k_0 with a small range Δk which is assumed to be sufficiently small than first Brillouin zone so that

$$E(k) \approx E(k_0) + (k-k_0)\left.\frac{dE(k)}{dk}\right|_{k=k_0} + \cdots,$$

$$u_k(x) \approx u_{k0}(x) + (k-k_0)\left.\frac{du_k(x)}{dk}\right|_{k=k_0} + \cdots. \tag{2.4.1.2}$$

$E(k)$ is expanded to the first-order term and $u_k(x)$ is expanded to the zero-order term because the significant alteration appears in the exponential function. Thus, with the Taylor expansions in Eq. (2.4.1.2) substituted into Eq. (2.4.1.1), $\Psi(x,t)$ can be approximated as

$$\Psi(x,t) = \psi_{k0}(x,t)\cdot\sum_k A(k)\cdot e^{i(k-k_0)[x-\frac{E'(k_0)}{\hbar}t]}, \tag{2.4.1.3}$$

$$\psi_{k0}(x,t) = u_{k0}(x)e^{i\left(k_0x-\frac{E(k_0)}{\hbar}t\right)}.$$

The group velocity at k_0 can be obtained from the motion of the slowly varying envelope function of the wave packet $\Psi(x,t)$ in Eq. (2.4.1.3), so that

$$x-\frac{E'(k_0)}{\hbar}t \approx \text{constant}, \tag{2.4.1.4}$$

and differentially both side, we have

$$\frac{d}{dt}x(t)-\frac{E'(k_0)}{\hbar}=0, \qquad v_g\Big|_{k_0} \equiv \frac{d}{dt}x(t) = \frac{1}{\hbar}\left.\frac{dE(k)}{dk}\right|_{k_0}. \tag{2.4.1.5}$$

Then, taking the time-varying wave vector $k(t)$ into account, we have

$$k(t) = \frac{1}{\hbar} eFt + k_0 , \tag{2.4.1.6}$$

where F is an additional external field and k_0 is the initial state at t=0. Furthermore, the acceleration rate is obtained by combining together with the group velocity v_g and time-varying wave vector $k(t)$

$$a \equiv \frac{dv_g(k)}{dt} = \frac{d}{dt}\frac{1}{\hbar}\frac{dE(k)}{dk} = \frac{1}{\hbar^2}\frac{d^2E(k)}{dk^2}\underbrace{\frac{d\hbar k}{dt}}_{\text{force}}, \tag{2.4.1.7}$$

with the effective mass

$$m^* \equiv \left[\frac{1}{\hbar^2}\frac{d^2E(k)}{dk^2}\right]^{-1}. \tag{2.4.1.8}$$

It is noticed that the assumption of $a = dv_g(k)/dt$ is only valid in the classical approximation. However, owing to the anisotropic and non-parabolic properties of the valence-band structure, the classical approximation fails and the ability to quantitatively deal with the hole effective masses as depicted in Eq. (2.4.1.8) is no longer available. Therefore, the reversely extracted hole effective masses will be introduced in the next section.

2.4.2 Density-of-States Effective Mass and Quantization Effective Mass

With our six-band $k \cdot p$ calculation for the hole subband structure in p-channel MOSFETs, the corresponding density-of-states (***DOS***) functions are determined in the Cartesian coordinate system by

$$DOS_j(E) = U(E - E_j)\frac{1}{(2\pi)^2} \times \frac{Area_j^{\text{k-space}}(E + dE) - Area_j^{\text{k-space}}(E)}{dE} \tag{2.4.2.1}$$

or in the polar coordinate system [3] by

$$DOS_j(E) = U(E - E_j)\frac{1}{(2\pi)^2}\int_0^{2\pi} \frac{K_j(E,\theta)}{\left|\frac{dE}{dK}\right|_{K_j(E,\theta)}} d\theta , \tag{2.4.2.2}$$

where the index j means the subband order up to the sixth lowest subband in this work

and $U(E)$ means the unit step function of energy. Then, the total ***DOS*** function is given by

$$DOS_{total}(E) = \sum_j DOS_j(E) . \tag{2.4.2.3}$$

In this sense, the energy dependent ***DOS*** effective mass of each subband, $m_{DOS}^j(E)$, can be extracted reversely from the simulated ***DOS***$_j$*(E)*:

$$m_{DOS}^j(E) = 2\pi\hbar^2 \times DOS_j(E) . \tag{2.4.2.4}$$

The resulted ***DOS*** effective mass of each subband is seen in Figure 2.4.2.1 and it is shown that the constant-like effective mass does not exist in this case. However, the averaged ***DOS*** effective mass can be obtained if we choose the correct average method. Consequently, the averaged ***DOS*** effective mass $\langle m_{DOS}^j \rangle$ is dependent on the carrier concentration, and our method to average the m_{DOS}^j is as follows:

$$\langle m_{DOS}^j \rangle = \frac{\int m_{DOS}^j(E) f(E) \cdot DOS_j(E) dE}{\int f(E) \cdot DOS_j(E) dE} . \tag{2.4.2.5}$$

In addition, the quantization effective mass, m_{QN}^j , can also be analytically assessed in the triangular potential approximation [9] :

$$E_j^{(0)} = \left(\frac{\hbar^2}{2m_{QN}^j} \right)^{1/3} \left(\frac{3}{2}\pi e F_s (i + \frac{3}{4}) \right)^{2/3} , \tag{2.4.2.6}$$

where $E_j^{(0)}$ represents the energy minimum of subband *j* and *i* is the states of the wave function (the ground state, the first excited state, or etc.). In summary, the averaged ***DOS*** effective mass $\langle m_{DOS}^j \rangle$ and the quantization effective mass m_{QN}^j both are the most important factors in our novel quantum simulation algorithm which will be discussed in Chapter 3.

Chapter 3

Quantum Simulator NEP for the Two-dimensional Inversion-layers

3.1 Schrődinger and Poisson Self-consistent NEP in n-MOSFETs

In this section, we introduce the fully Schrődinger and Poisson self-consistent solver in n-channel MOSFETs [10]. The schematic band diagram and physical environmental setup are given in Figure 3.1.1. We divide the band diagram of silicon substrate along the out-of-plane direction into two regions: one is the surface quantum confinement region (60 nm) and the other is the bulk classical region (200 nm). In the former region, the carriers are confined in this shallow region and we can mesh 300 intervals of width $dz_0 = 0.2$ nm to ensure simulation accuracy; in the later region, we adopt the conventional skill to deal with and it is divided into 50 intervals with width of $dz_1 = 4$ nm. It can significantly reduce the computational time but not losing the accuracy. Besides, the conduction band edge at the interface is set to be the zero of energy in n-MOSFETs.

Figure 3.1.2 is the flow-chart illustrating the common self-consistent procedure. First of all, we guess the surface band bending V_s into the Poisson equation subject to the boundary conditions $V_{(z=0)}=V_s$ and $V_{(z=bulk)}=0$. It would obtain the corresponding initial potential profile $V(z)$, and we start with the 1D Schrődinger equation, as revealed in Eq. (2.2.1), along with $V(z)$. As mentioned in Section 2.2, we would obtain the eigenvalues and the eigenfunction. Besides, we summarize the basic formulation and the iteration that we use for perform a self-consistent solution. In the surface

quantum confinement region, the three-dimensional carriers (both electrons and holes) density can be described by

$$n(z)=\sum_{i,j}\int_{E_{i,j}}^{\infty} DOS_{i,j}(E)_{2D}f(E)dE\cdot\left|\Psi_{i,j}(z)\right|^2$$

$$=\sum_{i,j} g_i\frac{m_{DOS}^i}{\pi\hbar^2}k_BT\ln\left(1+e^{\frac{E_f-E_{i,j}}{kT}}\right)\cdot\left|\Psi_{i,j}(z)\right|^2 \quad (3.1.1)$$

$$p(z)=\sum_{v,j}\int_{-\infty}^{E_{v,j}} DOS_{v,j}(E)_{2D}(1-f(E))dE\cdot\left|\Psi_{v,j}(z)\right|^2$$

$$=\sum_{v,j} g_v\frac{m_{DOS}^v}{\pi\hbar^2}k_BT\ln\left(1+e^{(\frac{E_{v,j}-E_f}{kT})}\right)\cdot\left|\Psi_{v,j}(z)\right|^2 \quad (3.1.2)$$

where i and v are the electron valley index and the hole type index, respectively. j is the subband index, and g_i and g_v are the degeneracy of the ith valley and vth type, respectively; m_{DOS}^i and m_{DOS}^v are the density of states electron and hole effective mass, respectively, and $E_{i,j}$ and $E_{v,j}$ are the electron and hole energy levels, . The corresponding wave-functions $\Psi_{i,j}$ and $\Psi_{v,j}$ are all normalized. In the bulk classical region, the carrier density is given by:

$$n(z)=n_0\cdot\exp(\frac{V(z)}{k_BT}) \quad (3.1.3)$$

$$p(z)=p_0\cdot\exp(\frac{-V(z)}{k_BT}), \quad (3.1.4)$$

where p_0 and n_0 are the carrier concentration under the thermal equilibrium. Substituting the above concentration in the 1D Poisson equation, we have

$$\frac{d^2V(z)}{dz}=-\frac{-q_0\cdot[-N_d^+(z)-n(z)+p(z)]}{\varepsilon_{si}}, \quad (3.1.5)$$

where $N_d^+(z)$ is the ionized donor density. Finally, we can obtain a new potential $V(z)$ to satisfy Eq. (3.1.5) and continuously iterate the procedure until the potential profile

$V(z)$ is equal for successive iterations, within a tolerable error range. The two-dimensional electron density can be written as

$$n_{i,j} = g_i \frac{m_{DOS}^i}{\pi\hbar^2} k_B T \ln\left(1+\mathrm{e}^{\frac{E_f - E_{i,j}}{kT}}\right) \tag{3.1.6}$$

and the total inversion layer charge density is thus given by

$$N_s = \sum_{i,j} n_{i,j} \ . \tag{3.1.7}$$

The average inversion layer thickness Z_{av} is described as

$$Z_{av} = \sum_{i,j}\left[\frac{n_{i,j}}{N_s} \cdot \int_0^{bulk} z \cdot \left|\Psi_{i,j}(z)\right|^2 dz\right]. \tag{3.1.8}$$

There are two kinds of the gate materials to be chosen in NEP: one is the high doping poly-silicon; the other is the metal. Here, we demonstrate the potential calculation for the high doping poly-silicon gate situation:

$$V_{fb} = -k_B T \ln\left(\frac{N_{ploy} N_d}{n_i^2}\right), \tag{3.1.9}$$

where V_{fb} is the flat band voltage, N_{poly} and N_d are the poly gate concentration and the substrate doping concentration, n_i is the intrinsic concentration and k_B is the Boltzmann's constant. The poly gate voltage and oxide voltage are the following:

$$V_{poly} = -\frac{\varepsilon_{Si} F_s^2}{2eN_{poly}}, \tag{3.1.10}$$

$$V_{ox} = \frac{t_{ox} \varepsilon_{Si} F_s}{\varepsilon_{ox}}, \tag{3.1.11}$$

where t_{ox} is the oxide thickness, ε_{si} and ε_{ox} are the dielectric constant of the silicon and oxide, respectively, and the surface electric field is given by $F_s = \frac{V_{(z=1)} - V_{(z=2)}}{\Delta z}$. The total gate voltage can be expressed as

$$V_g = V_s + V_{ox} + V_{poly} + V_{fb} \quad ,$$

(3.1.12)

where V_s indicates the surface band bending determined by the potential profile in the silicon substrate. Besides, we also examine the metal gate effect with the workfunction, (Φ_m = 4.05 eV), and the electron affinity, (χ = 4.05 eV), in our work. the Eq. (3.1.9) and (3.1.12) can be rewriten as:

$$V_{fb} = \Phi_m - \chi - E_g + kT \ln(\frac{N_V}{N_d}) \tag{3.1.13}$$

$$V_g = V_{ox} + V_s + V_{fb} \,. \tag{3.1.14}$$

where E_g is the energy band gap and N_v is the effective density of states in valence band. Figure 3.1.3. shows the energy band diagram for the metal/SiO_2/p-Si system.

3.2 Triangular Potential Well Approximation NEP in p-MOSFETs

Because of demanded computational time to calculate the hole subband structures with the six-band $k \cdot p$ method, the researchers usually use the triangular potential well approximation to solve the Schrődinger equation [3] instead of the fully Schrődinger and Poisson self-consistent method mentioned in the n-MOSFET NEP.

Firstly, we employ N_z=200 points along the z axis in the range of the potential well [0, Z_{max}] with $Z_{\max} = \frac{1.2}{q_0 F_s}$, energy points in the interval [E_0, E_0+0.2 eV]. Both Cartesian coordinate and polar coordinate are established in our simulator but the former one is adopted through the whole thesis. In order to keep the completeness of the work, we show the detailed polar and Cartesian coordinate systems for the comparison in Figure 3.2.1. Secondly, we start with 1D Schrődinger equation based on the six-band $k \cdot p$ Hamiltonian along with the potential profile $V(z)$ which can be

obtained from the surface field F_s as:

$$V(z) = -F_s \cdot z \tag{3.2.1}$$

and then we would get the hole subband structures $E(k_x,k_y)$ and corresponding wave functions according to the procedure of Section 2.2.1. The sixth lowest subbands are considered and for the convenience, we take j as the subband index in this section.

Thirdly, we determine the Fermi level location if the surface field outputs match with the input ones. The process is shown as below:

$$p_j = \int_{E_1}^{E_1+0.2} DOS_j(E) \cdot \frac{1}{1+\exp(\frac{E_j - Ef}{k_B T})} dE \tag{3.2.2}$$

$$P_{inv} = \sum_{j}^{6} p_j \quad . \tag{3.2.3}$$

The average inversion layer thickness z_{av} and band bending by the inversion layer are defined as

$$z_{av} = \sum_{j}^{6} \left[\frac{p_i}{P_{inv}} \cdot \int_{0}^{Z_{\max}} z \cdot \left| \Psi_j(z) \right|^2 dz \right] \tag{3.2.4}$$

$$V_{inv} = \frac{e \cdot P_{inv} \cdot z_{av}}{\varepsilon_{Si}} \quad . \tag{3.2.5}$$

Therefore, the surface band bending can be extracted by

$$V_s = E_g - (E_c - E_f)_{Bulk} + E_f \tag{3.2.6}$$

where E_g is the band gap of the semiconductor. The band bending by the depletion layer, V_{dep}, is described by

$$V_{dep} = V_s - V_{inv} - k_B T \, . \tag{3.2.7}$$

The sheet charge density of depletion layer is written as

$$p_{dep} = \sqrt{\frac{2\varepsilon_{Si} V_{dep} N_d}{e}} \, . \tag{3.2.8}$$

Finally, according to above results, the surface field is given by

$$F_s^{\text{output}} = \frac{-e\left(P_{inv} + P_{dep}\right)}{\varepsilon_{si}}. \tag{3.2.9}$$

The best solution of Fermi level location is found if the surface field is equal to the input one. We also represent the above process with the flow chart as shown in Figure 3.2.2.

3.3 Efficiently Improved NEP in p-MOSFETs

Here, the novel method rather than using the triangular potential well approximation is introduced to directly reduce the heavy computational burden from the full Schrődinger and Poisson self-consistent iteration in p-channel MOSFETs. The inspiration of this method is from the EMA algorithm in Section 2.4. The extracted *DOS* and quantization effective masses can be applied to enhance the converging speed. The first-order modification can provide the enough accuracy within the 1% error of the surface field and 10^{-6} V maximum error of the potential profile. The detailed procedure is discussed as following.

Firstly, in terms of the triangular potential approximation in the previous section, we solve the Schrődinger equation with six-band $k \cdot p$ Hamiltonian and would obtain corresponding *zero-order* DOS mass m_{DOS}^0, *zero-order* quantization mass m_{QM}^0, and *zero-order* surface band bending V_s^0. Secondly, we input these zero-order terms as the parameters of the n-MOS-like NEP appearing in Section 3.1, of course, the other parameters are all treated properly to satisfy the p-MOSFET condition. And then, we can get the *zero-order* surface potential profile $V_s^0(z)$ as the potential well shape (it can be seen as the more realistic potential profile than the triangular one) to solve the Schrődinger equation with six-band $k \cdot p$ Hamiltonian

again. Basically, the whole procedure follows the Section 3.2. Consequently, we would bring the first-order properties, such as *first-order* subband level $E^{(0)\,1st}$, *first-order* wave-function ξ^{1st}, the determined *first-order* Fermi-level E_f^{1st}, *first-order* inversion layer density p_{inv}^{1st}, *first-order* sheet density of depletion p_{dep}^{1st}, and *first-order* surface band bending V_s^{1st}. Finally, we use the above first-order physical properties along with Poisson equation to yield the first-order surface potential profile $V_s^{1st}(z)$ and the second-order surface band bending V_s^{2nd} in order to check whether surface potential profile converges or not. For the sake of providing a visual picture of above procedures, consider the flow-chart representation in Figure 3.3.1.

3.4 Low Temperature Effect: Impurity Ionization Rate

It is well known that for a semiconductor doped with donor or acceptor impurities, impurity energy levels are introduced [11]. When impurity atoms are introduced, the Fermi level must adjust itself to maintain charge neutrality. Consider the concentration of the donor impurities, N_d, are added to the crystal. In order to preserve electrical neutrality, the total negative charges (electrons and ionized acceptors) must be equal to the total positive charges (holes and ionized donors) as below

$$n = N_d^+ + p \tag{3.4.1}$$

where n is the electron density in the conduction band, p is the hole density in the valence band, and $N_d^+(z)$ is the ionized donors distribution as given by

$$N_d^+(z) = N_d \times \frac{1}{1+2e^{\left(\frac{E_D(z)-E_f}{k_BT}\right)}} \quad . \tag{3.4.2}$$

Rewriting the neutrality condition Eq. (3.4.1), we can obtain

$$N_c \exp(-\frac{E_c - E_{f,Bulk}}{k_BT}) = N_D \times \frac{1}{1+2e^{\left(\frac{E_{D,Bulk}-E_{f,Bulk}}{k_BT}\right)}} + N_v \exp(\frac{E_v - E_{f,\,Bulk}}{k_BT}) . \tag{3.4.3}$$

For a set of given correlated parameter with Eq. (3.4.3), the Fermi level, E_f, can be uniquely determined. From Eq. (3.4.3) we also know that the temperature condition alert the Fermi-level location strongly, so that the ionization rate must be taken into account at low temperature condition. Figure (3.4.1) shows that impurity ionization rate and band diagram at low temperature about 2 K. Therefore, at such low temperature, we have to face meaningless value and inaccurate approximation from simulator. Intrinsic carrier density, $n_i \approx 0$ and the ionization rate is almost 0% at 2 K. These will lead to the possibility of divergent calculations. So the net charges, at low temperature, via Eq. (3.4.1) have to use Fermi-Dirac integral $E_{\frac{1}{2}}$ rather than Boltzmann statistics case as below:

$$Q_{net}(z) = N_D^+(z) - N_C \frac{2}{\sqrt{\pi}} F_{1/2}\left(\frac{E_C(z)-E_f}{k_BT}\right) + N_V \frac{2}{\sqrt{\pi}} F_{1/2}\left(\frac{E_f - E_V(z)}{k_BT}\right) \tag{3.4.4}$$

and

$$Q_{net}(z) = N_D^+(z) - N_C e^{-\frac{E_f - E_{C0}}{k_BT}} + N_V e^{-\frac{E_{V0}-E_f}{k_BT}} \tag{3.4.5}$$

where Eq. (3.4.4) focus to non-neutral region and Eq. (3.4.5) is used in electrical neutral region. Above formula is to avoid the n_i to appear in the simulation process.

Chapter 4

Hole Mobility Model and Theory

Introduction

In this section, we calculate the hole mobility under the relaxation time approximation which uses the subband energy and the wavefunction provided by our new fast method. And we discuss the momentum relation rates caused by scattering with phonons and surface roughness. In this work, we will ignore the Coulomb scattering with ionized impurities in substrate. All the scattering parameters used in this work are listed on Table II.

4.1 Phonon Scattering

It is well known that at room temperature the vibrating atoms create pressure waves in crystal, thus bringing two types of phonon scattering that are important to describe Si mobility. Phonon scattering can be described in terms of the acoustic phonon scattering and optical phonon scattering, based on the phase of the vibration of the two different atoms in one primitive cell. Acoustic phonon energy is smaller than carrier energy, while optical phonon energy is about 61.2 meV for silicon. Using the phonon mobility formulation underlying the isotropic momentum approximation is derived from [3]. More precisely, for the acoustic phonons, the isotropic relaxation time in the subband μ to ν is gives by:

$$\frac{1}{\tau_{ac}^{(\mu)}(K)} \approx \frac{2\pi \bullet k_B T \bullet D_{ac}^2}{\hbar \rho u_l^2} \sum_{\nu} F_{\mu\nu} \bullet DOS_{\nu}[E_{\mu}(K)]$$

$$= \frac{k_B T \bullet D_{ac}^2}{\hbar^3 \rho u_l^2} \sum_v F_{\mu v} \bullet m_{DOS(v)}[E_\mu(K)] \tag{4.1.1}$$

$$F_{\mu v} = \int_0^W \left| \xi_0^{(\mu)}(z) \bullet \xi_0^{(v)}(z) \right|^2 dz \tag{4.1.2}$$

where $\boldsymbol{D}_{\text{ac}}$ denotes the deformation potential due to acoustic phonon, ρ is the crystal density, u_l is the longitudinal sound velocity, $F_{\mu v}$ is the form factor determined by the wavefunctions of the μ-th subband and the v-th subbands, $\hbar$ is the Planck constant divided by 2π, and k_B is the Boltzmann constant. For the optical phonons, the scattering rate can be described as

$$\frac{1}{\tau_{op}^{(\mu)}(K)} \approx \frac{\pi \bullet D_{op}^2}{\rho \varpi_{op}} \sum_v F_{\mu v} \bullet DOS_v[E_\mu(K) \mp E_K] \times \frac{1 - f_0[E_\mu(K) \mp E_K]}{1 - f_0[E_\mu(K)]} (n_{op} + \frac{1}{2} \pm \frac{1}{2})$$

$$= \frac{D_{op}^2}{2\hbar \rho E_K} \sum_v F_{\mu v} \bullet m_{DOS(v)}[E_\mu(K) \mp E_K] \times \frac{1 - f_0[E_\mu(K) \mp E_K]}{1 - f_0[E_\mu(K)]} (n_{op} + \frac{1}{2} \pm \frac{1}{2}) \tag{4.1.3}$$

where "+" means phonon emission and "—" means phonon absorption. $\boldsymbol{D}_{op}$ and $\boldsymbol{E}_K$ are the deformation potential and the optical phonon energy, respectively. n_{op} is the occupation number given by

$$n_{op} = \frac{1}{[\exp(\frac{E_K}{k_B T}) - 1]} \ . \tag{4.1.4}$$

4.2 Surface Roughness Scattering

At high effective field, the roughness scattering between Si and SiO_2 plays a very important role and this reduces the mobility in the inversion layer of a MOSFET device. Analysis of such mobility component usually involves two kinds of assumptions, one is the Gaussian autocovariance function and the other is exponential autovariance function. In this work, we prefer use of Gaussian autocovariance

function because the exponential model to calculate the scattering rate of inversion layer holes due to surface roughness needs larger values of the rms height Δ required to fit experimental mobility data than the Gaussian model for the autocovariance. Besides, we have to make an important assumption that the single subband approximation is quite accurate. Since surface roughness is anisotropic scattering, we only consider the intrasubband scattering. Under Yamakawa's surface roughness model [12], the scattering rate for a Gaussian function is written as

$$\frac{1}{\tau_G(E)} = \frac{m_{DOS}(E)\bullet e^2 \bullet E_{eff}^2 \bullet \Delta^2 \bullet \Lambda^2}{2\hbar^3} \int_0^{2\pi} e^{\frac{-q^2\Lambda^2}{4}} \bullet (1-\cos\theta) d\theta$$

$$= \frac{m_{DOS,j}(E)\bullet e^2 \bullet E_{eff}^2 \bullet \Delta^2 \bullet \Lambda^2}{2\times 2\hbar^3} \int_0^{2\pi} e^{\frac{-q^2\Lambda^2}{4}} \bullet (1-\cos\theta) d\theta \quad \text{[excluding spin]} \quad (4.2.1)$$

$$q^2 = 2k^2(1-\cos\theta) \quad (4.2.2)$$

$$k^2 = \frac{2m_{DOS,j}\cdot(\mathrm{E}-\mathrm{E}_j)}{\hbar^2} \quad (4.2.3)$$

where $\boldsymbol{m}_{DOS,j}$ is the density of states effective mass in the j-th subband, E_j is the hole subband energy and E_{eff} is the hole effective field by

$$E_{eff} = \frac{e\cdot(P_{dep} + \frac{1}{3}P_{inv})}{\varepsilon_{si}} . \quad (4.2.4)$$

4.3 Derivation of Two-Dimensional Mobility

The mobility calculation method in this work originates from the linearization of the Boltzmann transport equation where the total scattering rate can be expressed in terms of the phonon scattering and surface roughness scattering ones [4], [13]:

$$\frac{1}{\tau_{total}(E)} = \frac{1}{\tau_{phonon}(E)} + \frac{1}{\tau_{SR}(E)} . \quad (4.3.1)$$

It is important that we avoid Matthiessen's rule to calculate inaccurate total mobility

which may cause scattering parameter shift. The reasons are as follow:

$$<\frac{1}{\tau_{total}}>=<\frac{1}{\tau_{phonon}}+\frac{1}{\tau_{SR}}>\neq\left[<\frac{1}{\tau_{phonon}}>+<\frac{1}{\tau_{SR}}>\right] \tag{4.3.2}$$

Therefore, we have to sum up the total scattering rate and then to calculate mobility. It would lead to the accurate mobility. Besides, the inversion layer carriers in the MOS system are quantized along the *z* (out-of-plane) direction, and we have to consider the quasi-2D case when calculating the hole mobility of the MOS system. Now we derivate the two-dimensional mobility excluding the spin degeneracy (g=1). Starting with the Boltzmann equation and *n* carrier concentration, we can write

$$n=\int\frac{fd^3k}{(\frac{2\pi}{L_x}\frac{2\pi}{L_y}\frac{2\pi}{L_z})}/(L_xL_yL_z)$$

$$=\int\frac{f\,d^3k}{8\pi^3} \tag{4.3.3}$$

$$f=f_0+\frac{\partial f_0}{\partial E}(-\mathbf{v}\tau q\boldsymbol{\varepsilon}) \tag{4.3.4}$$

$$f_0=\frac{1}{1+e^{\frac{E-E_f}{k_BT}}} \tag{4.3.5}$$

where f_0 is the Fermi-Dirac distribution function under equilibrium and f is the first-order Taylor series expansion with respect to energy E, i.e., f_0 is the Fermi-Dirac distribution function under applied electric field $\boldsymbol{\varepsilon}$. And then we use the current density per unit length *J* (*J*=I/W):

$$\mathbf{J_i}=en\mathbf{v_i}$$

$$=e\int\frac{f\,d^3k}{8\pi^3}\mathbf{v_i}$$

$$=e\int f_0\mathbf{v_i}\frac{d^3k}{8\pi^3}+e\int(-\frac{\partial f_0}{\partial E})(\tau e\mathbf{v_j}\boldsymbol{\varepsilon_j})\mathbf{v_i}\frac{d^3k}{8\pi^3}$$

$$=[\frac{e^2}{8\pi^3}\int\mathbf{v_i}\mathbf{v_j}\tau(-\frac{\partial f_0}{\partial E})d^3k]\boldsymbol{\varepsilon_j} \tag{4.3.6}$$

where $e\int f_0 \mathbf{v_i}\frac{d^3k}{8\pi^3}$ term is zero since no current under equilibrium and i and j are the carrier transport direction. Using the concept of conductivity σ , the current density can be expressed as follows:

$$\mathbf{J_i} = \sigma_{ij}\boldsymbol{\varepsilon}_\mathbf{j}$$

$$\Rightarrow \sigma_{ij} = \frac{e^2}{8\pi^3}\int \mathbf{v_i}\mathbf{v_j}\tau(-\frac{\partial f_0}{\partial E})d^3k \tag{4.3.7}$$

$$\sigma_{ij} = en_s\mu_{ij}$$

$$n_s \equiv \int f_0 \frac{d^3k}{8\pi^3} \text{ (excluding spin)} \tag{4.3.8}$$

$$\mu_{ij} = \frac{\sigma_{ij}}{qn_s} = \frac{e\int \mathbf{v_i}\mathbf{v_j}\tau(-\frac{\partial f_0}{\partial E})d^3k}{8\pi^3\int f_0\frac{d^3k}{8\pi^3}}. \tag{4.3.9}$$

Now we only focus on 2D case with the spin degeneracy factor of unity along *xx* direction can be rewritten as:

$$\sigma_{xx}^{v} = \frac{e^2}{4\pi^2}\int \mathbf{v_x}\mathbf{v_x}\tau_x(-\frac{\partial f_0}{\partial E})d^2k$$

$$= \frac{e^2}{4\pi^2}\int \frac{1}{\hbar^2}(\frac{\partial E}{\partial k_x})^2\tau_v f_0(E)[1-f_0(E)]\frac{1}{k_BT}d\phi\frac{KdE}{(\frac{\partial E}{\partial K})}$$

$$= \frac{e^2}{4\pi^2\hbar^2k_BT}\int_0^{2\pi} d\phi\int_{E_v}^{\infty} dE\frac{K_v(E,\phi)}{(\frac{\partial E}{\partial K})}(\frac{\partial E}{\partial k_x})^2\tau_v f_0(E)[1-f_0(E)] \tag{4.3.10}$$

$$\mu_{xx}^{v} = \frac{\sigma_{xx}^{v}}{en_{vs}}$$

$$= \frac{e}{4\pi^2\hbar^2k_BTn_{vs}}\int_0^{2\pi} d\phi\int_{E_v}^{\infty} dE\frac{K_v(E,\phi)}{(\frac{\partial E}{\partial K})}(\frac{\partial E}{\partial k_x})^2\tau_v(E)f_0(E)[1-f_0(E)] \tag{4.3.11}$$

$$\mu_{xx} = \sum_{v=1}^{6} N^v \times \mu_{xx}^v$$
$$= \sum_{v=1}^{6} \frac{n_{vs}}{n_s} \times \mu_{xx}^v$$
$$= \frac{e}{4\pi^2 \hbar^2 k_B T n_s} \sum_{v=1}^{6} \int_0^{2\pi} d\phi \int_{E_v}^{\infty} dE \frac{K_v(E,\phi)}{(\frac{\partial E}{\partial K})} (\frac{\partial E}{\partial k_x})^2 \tau_v(E) f_0(E)[1 - f_0(E)] \qquad (4.3.12)$$

where $\boldsymbol{n}_{\mathrm{S}}$ is the total hole density per unit area and $\tau_v(E)$ is the energy dependent total scattering rate for subband *v*. In this work, the detailed expressions above are derived in the polar coordinate, and we have used the definition in Section 2.4 (Eq. (2.4.1.5) and Eq. (2.4.2.2)) as a result, Eq. (4.3.12) can be rewritten as below:

Let $\mathrm{Velocity_G(E)} = \sum_{\mathrm{k=states}} \mathrm{v}_{\mathrm{g,k}}^2(E)$

$$\mu_{xx} = \frac{e}{k_B T n_s} \sum_{v=1}^{6} \int_{E_v}^{\infty} dE \cdot \mathrm{Velocity_G(E)} \times DOS_v(E) \times \tau_v(E) f_0(E)[1 - f_0(E)]$$
$$= \frac{e}{2\pi\hbar^2 k_B T n_s} \sum_{v=1}^{6} \int_{E_v}^{\infty} dE \cdot \mathrm{Velocity_G(E)} \times m_{DOS}(E) \times \tau_v(E) f_0(E)[1 - f_0(E)] \quad (4.3.13)$$

That is the first formalism for the hole mobility calculation, derived in the EMA picture and expressed as functions of a handful of accessible parameters: the inversion layer carrier density, the subband level and *DOS* effective masses, the energy dependent total scattering rate, and the Fermi-Dirac distribution function. In next chapters, we use above formula to calculate the hole mobility.

Chapter 5

Simulation Results and Discussion

In this section, the simulation results in n-MOSFETs, which are mentioned in section 3.1, are compared with these of Schred's [1] in Figure 5.1 to Figure 5.4. The model parameters are shown as follows: temperature is 300K, oxide thickness is 2.8nm, n+ ploy gate doping concentration is 2.2×10^{20} cm^{-3} and p-substrate doping concentration is 2×10^{16} cm^{-3}. We also examine the metal gate effect with a work-function 4.05 eV as shown in Figure 5.5 to Figure 5.8. Based on these results, our model come to be reasonable for calculating properties in n-MOSFETs. In the future work, we will use this simulator to calculate strain effect on the electron mobility. Besides, in p-MOSFETs, we also present calculations using the approximation of triangular potential well for the (001), (110) and (111) surface and strain effect along with comparing with Fischetti's [3] as are shown in Figure 5.9 to Figure 5.13. The model parameters are shown as follows: Temperature is 300K and substrate doping is 1×10^{17} cm^{-3}. Figures for 5.14 to 5.16 show the simulation results of subband level and density of states comparing with Li's [14] and Michielis's [15]. Furthermore, it is clarified that subband level is defined at subband minimum in this work rather than at gamma point. Figure 5.17 and Figure 5.18 can summarize the subband energy and calculation time compared with three techniques (triangular potential approximation, conventional self-consistent method, and fast self-consistent method in this work). Because of strong confinement with the triangular potential well, the subbands are higher than others. According to above simulated results, they point out that subband structure through our new model is more efficienct and correct. Based on the simulation results, the equivalent effective mass, i.e., quantization

effective mass (m_z) and density of states effective mass (m_{DOS}) for different temperatures and strains can all be extracted as shown in Figure 5.19 to Figure 5.20. They show that quantization effective mass is independent on temperature while density of states effective mass exhibits a strong dependent. It is also verified in Figure 5.21 that the simulation results of density of states effective mass reasonably match the cyclotron effective mass (m_c) by Shubnikov-de Haas (SdH) oscillation expect [5] under extremely low temperature, 2K, in Figure 5.21.

According to the assumptions, when calculating the hole subband level and effective mass of p-MOSFETs, we further present a simplified physics based model to describe the hole mobility, which mainly consists of the phonon-limited mobility, μ_{ph}, [13] and the surface roughness limited mobility, μ_{SR}, [12]. Figure 22 shows the scattering rate of phonon and surface roughness at different temperatures. This study also compares the simulation results by EMA with the experimental data [6] in three different temperatures of 77 K, 153 K and 300 K in Figure 23. We adjust the model parameters by the best fitting those curves. All the parameters are shown in Table 2. At extremely low temperature and high effective electric field region, the surface roughness scattering would dominate the scattering mechanisms, so we can determine the surface roughness parameters. However, at low electric field, the phonon scattering mechanisms become a dominative feature. It is noticeable that there is a considerable deviation between simulation results and experimental data at 153 K. A reasonable physical explanation of this discrepancy is that we have eliminated Coulomb scattering mechanisms in our model and the experimental data is not *universal curve* at 153 K.

Chapter 6

Conclusion

In summary, we have presented the self-consistent for solving Schrődinger and Poisson equations in n-channel MOSFETs which were applied us to simulate more realistic physical environment in nano devices. The simulation results show excellent agreements with Schred's [1]. However, we also have introduced a new technique based on six-band $k \cdot p$ Hamiltonian to avoid spending too much calculation time through the self-consistent method and to simulate the operation conditions under very low temperature. In order to ensure the validity of our work, we as well as have built a simplified effective model for the hole mobility in the inversion layer of p-MOSFETs. In fact, the parameters are extracted by best curve-fitting to the experimental data as cited in Takagi's paper [6]. It is noticeable that the Coulomb scattering was not included in our model. In addition, we extract the density of states effective mass and compare it well with cyclotron effective mass at 2 K [5]

For the further research in the future, the important issues could be listed as follows: The strain-induced enhancement of the mobility in p-channel MOSFETs [16]-[20], gate direct tunneling current [21], [22] and mobility enhancement in one-dimensional silicon nanowires, specially, the physical fluctuations (like surface roughness) may have a strong impact on the transport of silicon nanowires.

Appendix

A Fast Quantum Simulator for the Two-Dimensional Inversion Layers

Student: Kuan-Hao Cheng 鄭寬豪

Advisor: Dr. Ming-Jer Chen 陳明哲 博士

Outline

- Introduction
- Numerical Technique and Physical Theory
- Quantum Simulator NEP for the Two-dimensional Inversion-layers
- Hole Mobility
- Simulation Results and Discussion
- Conclusion

Outline

- **Introduction**
  - Motivation
- **Numerical Technique and Physical Theory**
- **Quantum Simulator NEP for the Two-dimensional Inversion-layers**
- **Hole Mobility**
- **Simulation Results and Discussion**
- **Conclusion**

Motivation I

- To compensate inaccuracy at the interface between oxide layer and substrate caused by triangular potential well approximation.

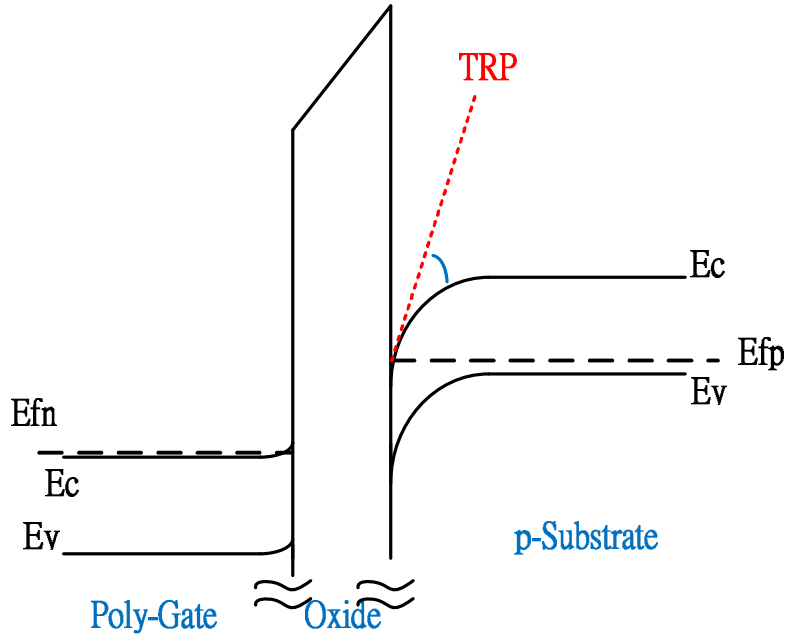

- Use self-consistent method to simulate more realistic environment at the interface.

Motivation II

- The Schrödinger and Poisson self-consistent procedure will lead to the ***intolerable computation time*** in pMOS.

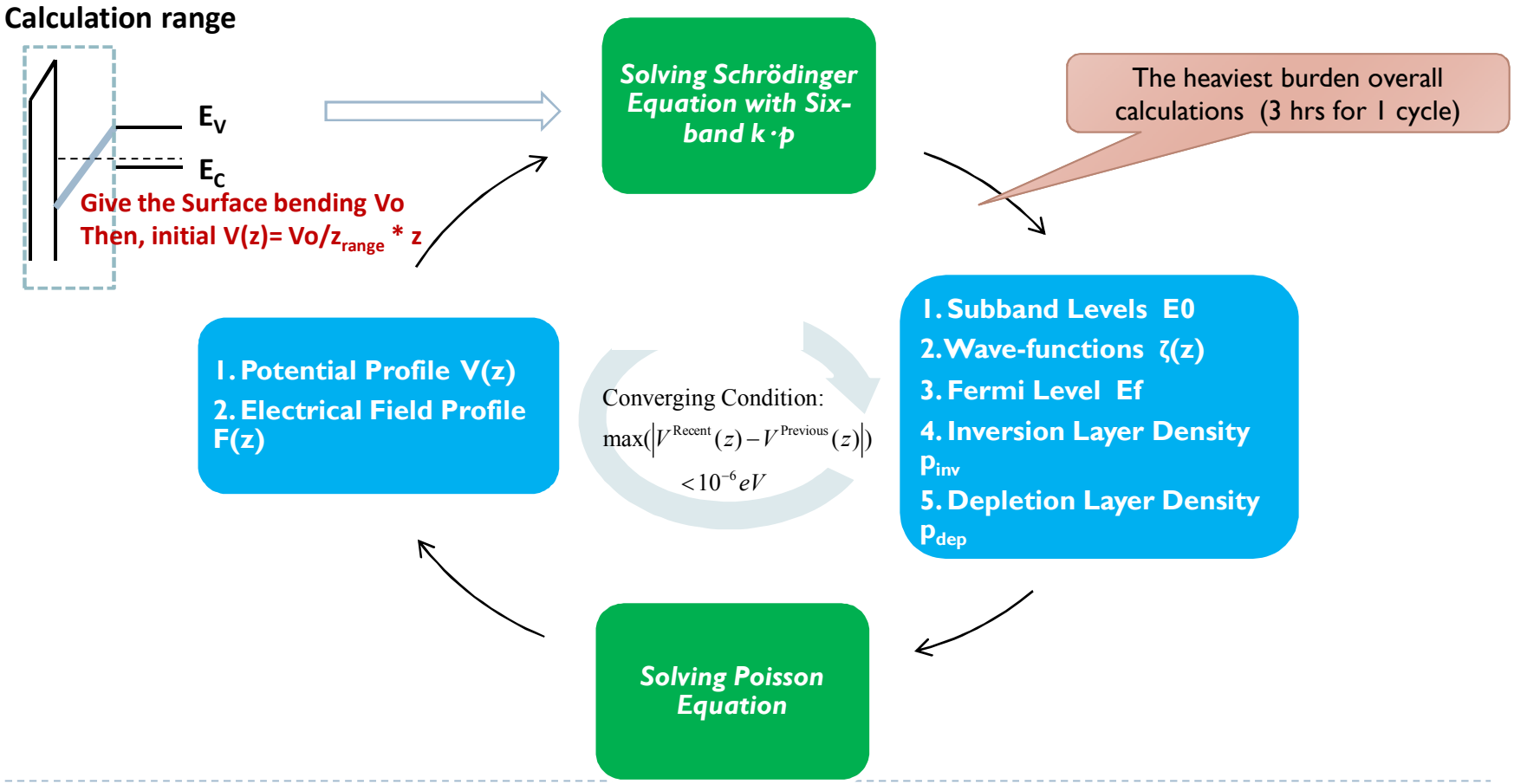

Outline

- Introduction
- **Numerical Technique and Physical Theory**
  - Time-independent Schrödinger Equation: Matrix Techniques
  - Six-band $k \cdot p$ Calculation for the Hole Subband Structure in p-MOSFETs
  - Newton-Raphson Method
  - Effective Mass Approximation (EMA)
- Quantum Simulator NEP for the Two-dimensional Inversion-layers
- Hole Mobility Model and Theory
- Simulation Results and Discussion
- Conclusion

Outline

- Introduction
- **Mathematical Technique and Theory**
  - Time-independent Schrödinger Equation: Matrix Techniques
  - Six-band $k \cdot p$ Calculation for the Hole Subband Structure in p-MOSFETs
  - Newton-Raphson Method
  - Effective Mass Approximation (EMA)
- **Quantum Simulator NEP for the Two-dimensional Inversion-layers**
- **Hole Mobility**
- **Simulation Results and Discussion**
- **Conclusion**

Time-independent Schrödinger Equation: Matrix Techniques

Time independent Schrödinger equation:

$$H\Psi = E\Psi$$

$$-\frac{\hbar^2}{2m}\nabla^2\Psi + V\Psi = E\Psi$$

$$\Psi = \sum_n a_n \psi_n$$

$$H\psi = -\frac{\hbar^2}{2m}\frac{\partial^2}{\partial x}\psi + V\psi$$

$$\boxed{H\psi = -\frac{\hbar^2}{2m}\left[\frac{\psi_{(x_{i-1})}}{\Delta x^2} - 2\frac{\psi_{(x_i)}}{\Delta x^2} + \frac{\psi_{(x_{i+1})}}{\Delta x^2}\right] + V_{(x_{i+1})}\psi_{(x_{i+1})}}$$

Boundary Condition: $\psi_{(0)} = \psi_{(n+1)} = 0$

$$ex:\ \mathrm{i}=1 \Rightarrow -\frac{\hbar^2}{2\mathrm{m}}\left[\frac{\psi_{(0)}}{\Delta x^2} - 2\frac{\psi_{(1)}}{\Delta x^2} + \frac{\psi_{(2)}}{\Delta x^2}\right] + V_{(1)}\ \psi_{(1)}$$

$$= -\frac{\hbar^2}{2\mathrm{m}}\left[\ 0\ \ - 2\frac{\psi_{(1)}}{\Delta x^2} + \frac{\psi_{(2)}}{\Delta x^2}\right] + V_{(1)}\ \psi_{(1)}$$

$$\mathrm{i}=2 \Rightarrow -\frac{\hbar^2}{2\mathrm{m}}\left[\frac{\psi_{(1)}}{\Delta x^2} - 2\frac{\psi_{(2)}}{\Delta x^2} + \frac{\psi_{(3)}}{\Delta x^2}\right] + V_{(2)}\ \psi_{(2)}$$

$$\mathrm{i}=3 \Rightarrow -\frac{\hbar^2}{2\mathrm{m}}\left[\frac{\psi_{(2)}}{\Delta x^2} - 2\frac{\psi_{(3)}}{\Delta x^2} + \frac{\psi_{(4)}}{\Delta x^2}\right] + V_{(3)}\ \psi_{(3)}$$

$$\mathrm{i}=4 \Rightarrow -\frac{\hbar^2}{2\mathrm{m}}\left[\frac{\psi_{(3)}}{\Delta x^2} - 2\frac{\psi_{(4)}}{\Delta x^2} + \frac{\psi_{(5)}}{\Delta x^2}\right] + V_{(4)}\ \psi_{(4)}$$

$$\vdots$$

$$\mathrm{i}=\mathrm{n} \Rightarrow -\frac{\hbar^2}{2\mathrm{m}}\left[\frac{\psi_{(\mathrm{n}+1)}}{\Delta x^2} - 2\frac{\psi_{(n)}}{\Delta x^2} + \frac{\psi_{(n-1)}}{\Delta x^2}\right] + V_{(n)}\psi_{(n)}$$

$$= -\frac{\hbar^2}{2\mathrm{m}}\left[\ 0\ \ - 2\frac{\psi_{(n)}}{\Delta x^2} + \frac{\psi_{(n-1)}}{\Delta x^2}\right] + V_{(n)}\psi_{(n)}$$

Time-independent Schrödinger Equation: Matrix Techniques

$$-\frac{\hbar^2}{2m}\left[\frac{\Psi(x-\Delta x)-2\Psi(x)+\Psi(x+\Delta x)}{\Delta x^2}\right]+V(x)\Psi(x)-E\Psi(x)=0$$

$$\begin{bmatrix} A_{(x_1)} & B & 0 & \cdots & 0 \\ B & A_{(x_2)} & B & & 0 \\ 0 & B & A_{(x_3)} & B & \vdots \\ \vdots & & & \ddots & 0 \\ 0 & \cdots & 0 & B & A_{(x_n)} \end{bmatrix} \bullet \begin{bmatrix} a_1\psi_1 \\ a_2\psi_2 \\ \vdots \\ \vdots \\ a_n\psi_n \end{bmatrix}_{n\times 1} = 0$$

$$A_{(x_i)} = \frac{\hbar^2}{m(\Delta x)^2} + V(x_i) - E$$

$$B = -\frac{\hbar^2}{2m(\Delta x)^2}$$

Outline

- Introduction
- **Numerical Technique and Physical Theory**
  - Time-independent Schrödinger Equation: Matrix Techniques
  - Six-band $k \cdot p$ Calculation for the Hole Subband Structure in p-MOSFETs
  - Newton-Raphson Method
  - Effective Mass Approximation (EMA)
- **Quantum Simulator NEP for the Two-dimensional Inversion-layers**
- **Hole Mobility**
- **Simulation Results and Discussion**
- **Conclusion**

Quantum Simulation in p-MOSFETs

By following the theoretical work by Fischetti, et al. [3]

$$\left[H_{k\cdot p}(k_x, k_y, k_z = -i\frac{d}{dz}) + qV(z) \right] \cdot \xi_{k_x,k_y}(z) = E(k_x, k_y) \cdot \xi_{k_x,k_y}(z)$$

$$H_{k\cdot p} = H_{LK} + H_{strain} = \begin{bmatrix} -P-Q & L & -M & 0 & \frac{1}{\sqrt{2}}L & -\sqrt{2}M \\ L^+ & -P+Q & 0 & -M & \sqrt{2}Q & -\sqrt{\frac{3}{2}}L \\ -M^+ & 0 & -P+Q & -L & -\sqrt{\frac{3}{2}}L^+ & -\sqrt{2}Q \\ 0 & -M^+ & -L^+ & -P-Q & \sqrt{2}M^+ & \frac{1}{\sqrt{2}}L^+ \\ \frac{1}{\sqrt{2}}L^+ & \sqrt{2}Q^+ & -\sqrt{\frac{3}{2}}L & \sqrt{2}M & -P-\Delta & 0 \\ -\sqrt{2}M^+ & -\sqrt{\frac{3}{2}}L^+ & -\sqrt{2}Q^+ & \frac{1}{\sqrt{2}}L & 0 & -P-\Delta \end{bmatrix}$$

$$P = P_k + P_\varepsilon$$
$$Q = Q_k + Q_\varepsilon$$
$$L = L_k + L_\varepsilon$$
$$M = M_k + M_\varepsilon$$

$k \bullet p$ terms (001)

$$P_k = \frac{\hbar^2}{2m_0}\gamma_1\left(k_x^2 + k_y^2 + k_z^2\right)$$
$$Q_k = \frac{\hbar^2}{2m_0}\gamma_2\left(k_x^2 + k_y^2 - 2k_z^2\right)$$
$$L_k = \frac{\hbar^2}{m_0}\sqrt{3}\gamma_3\left(k_x - ik_y\right)k_z$$
$$M_k = -\frac{\hbar^2}{2m_0}\sqrt{3}\left[\gamma_2\left(k_x^2 - k_y^2\right) - 2i\gamma_3 k_x k_y\right]$$

Strain terms (001)

$$P_\varepsilon = -a_v\left(\varepsilon_{xx} + \varepsilon_{yy} + \varepsilon_{zz}\right)$$
$$Q_\varepsilon = -\frac{b}{2}\left(\varepsilon_{xx} + \varepsilon_{yy} - 2\varepsilon_{zz}\right)$$
$$L_\varepsilon = -d\left(\varepsilon_{xz} - i\varepsilon_{yz}\right)$$
$$M_\varepsilon = \frac{\sqrt{3}}{2}b\left(\varepsilon_{xx} - \varepsilon_{yy}\right) - id\varepsilon_{xy}$$

Quantum Simulation in p-MOSFETs

Matrix Techniques:

$$\begin{bmatrix} \cdot & \cdot & \cdot & \cdot & \cdot & \cdot & \cdot \\ \cdot & D^- & D^0_{l-1} & D^+ & 0 & 0 & \cdot \\ \cdot & 0 & D^- & D^0_l & D^+ & 0 & \cdot \\ \cdot & 0 & 0 & D^- & D^0_{l+1} & D^+ & \cdot \\ \cdot & \cdot & \cdot & \cdot & \cdot & \cdot & \cdot \end{bmatrix}_{6l\times 6l} \begin{bmatrix} \cdot \\ \xi^{l-1}_{k_x,k_y} \\ \xi^{l}_{k_x,k_y} \\ \xi^{l+1}_{k_x,k_y} \\ \cdot \end{bmatrix} = E(k_x,k_y) \begin{bmatrix} \cdot \\ \xi^{l-1}_{k_x,k_y} \\ \xi^{l}_{k_x,k_y} \\ \xi^{l+1}_{k_x,k_y} \\ \cdot \end{bmatrix}$$

$$H_{k\cdot p}=H_0+H_1\cdot k_z+H_2\cdot k_z^2$$

$$D^+=\frac{H_1}{2i\Delta z}-\frac{H_2}{(\Delta z)^2}$$

$$D^0=H_0+\frac{2H_2}{(\Delta z)^2}$$

$$D^-=-\frac{H_1}{2i\Delta z}-\frac{H_2}{(\Delta z)^2}$$

Surface Orientation Effect

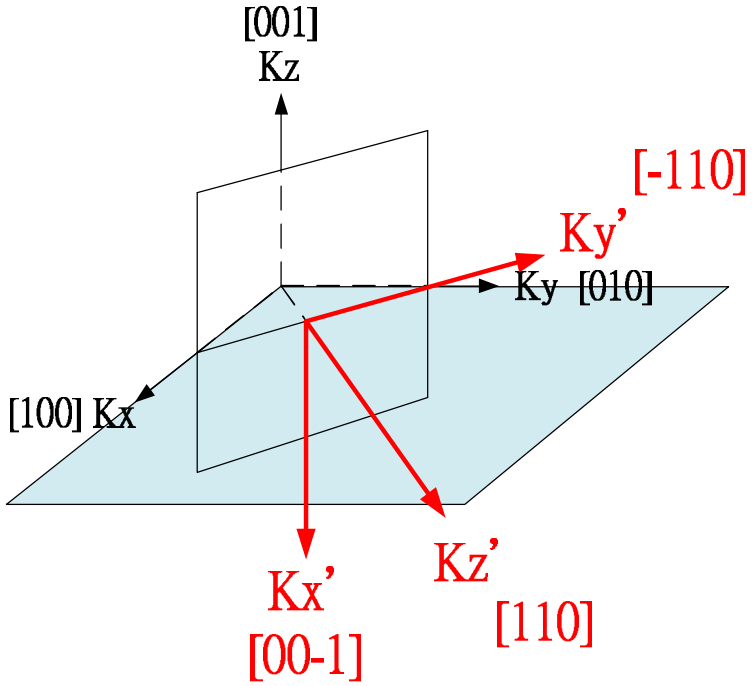

(011) Wafer

$$k_x' = -k_z$$

$$k_y' = \frac{1}{\sqrt{2}}(k_x - k_y)$$

$$k_z' = \frac{1}{\sqrt{2}}(k_x + k_y)$$

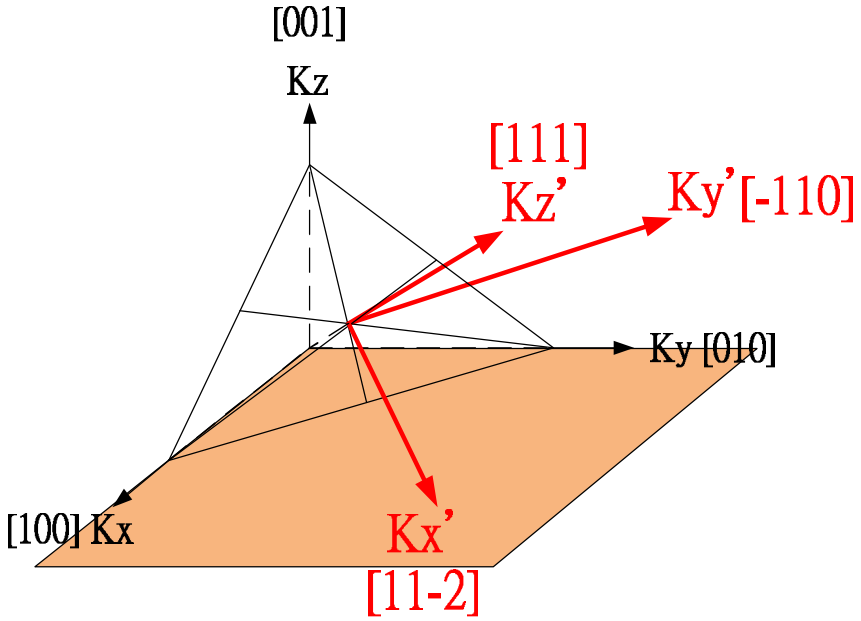

(111) Wafer

$$k_x' = \frac{k_x}{\sqrt{6}} + \frac{ky}{\sqrt{6}} - \frac{2k_z}{\sqrt{6}}$$

$$k_y' = \frac{1}{\sqrt{2}}(-k_x + k_y)$$

$$k_z' = \frac{k_x}{\sqrt{3}} + \frac{k_y}{\sqrt{3}} + \frac{k_z}{\sqrt{3}}$$

Outline

- Introduction
- **Numerical Technique and Physical Theory**
  - Time-independent Schrödinger Equation: Matrix Techniques
  - Six-band $k \cdot p$ Calculation for the Hole Subband Structure in p-MOSFETs
  - Newton-Raphson Method
  - Effective Mass Approximation (EMA)
- **Quantum Simulator NEP for the Two-dimensional Inversion-layers**
- **Hole Mobility**
- **Simulation Results and Discussion**
- **Conclusion**

Newton-Raphson Method

Derive :

$$f(x_0+\varepsilon)=f(x_0)+f'(x_0)\varepsilon+\frac{1}{2}f''(x_0)\varepsilon^2+\cdots$$

$$f(x_0+\varepsilon)\approx f(x_0)+f'(x_0)\varepsilon$$

Setting $f(x_0+\varepsilon)=0$

$$\varepsilon=-\frac{f(x_0)}{f'(x_0)}$$

$$x_1=x_0+\varepsilon=x_0-\frac{f(x_0)}{f'(x_0)}$$

$$x_{n+1}=x_n-\frac{f(x_0)}{f'(x_0)}$$

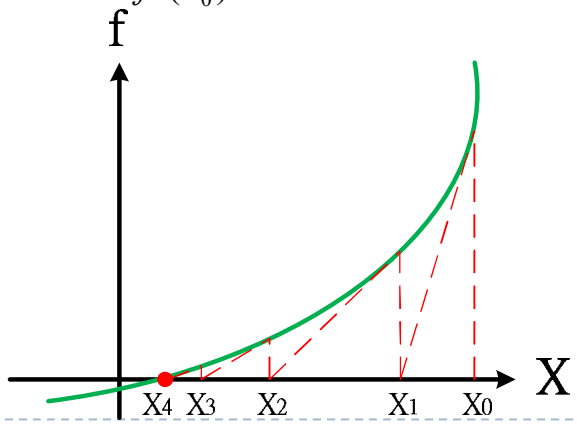

For Poisson equation

$$\nabla\cdot\vec{D}=\rho\rightarrow\nabla\cdot\vec{E}=\frac{\rho}{\varepsilon}\rightarrow\boxed{\nabla^2V=-\frac{\rho}{\varepsilon}}$$

For 1-D,

$$\nabla^2V=-\frac{\rho}{\varepsilon}\rightarrow\frac{\partial^2V}{\partial x^2}=-\frac{\rho}{\varepsilon}$$

$$\frac{\partial V}{\partial x}=\frac{V(x_{i+1})-V(x_i)}{\Delta x}\rightarrow\frac{\partial^2V}{\partial x^2}=\frac{\dfrac{V(x_{i+1})-V(x_i)}{\Delta x}-\left(\dfrac{V(x_i)-V(x_{i-1})}{\Delta x}\right)}{\Delta x}$$

$$=\frac{V(x_{i+1})-2V(x_i)+V(x_{i-1})}{(\Delta x)^2}$$

Therefore, the original equation $\nabla^2V=-\frac{\rho}{\varepsilon}$

can be written in matrix form as

Ex: 3×3 matrix

$$\begin{pmatrix}-2/(\Delta x)^2 & 1/(\Delta x)^2 & 0\\ 1/(\Delta x)^2 & -2/(\Delta x)^2 & 1/(\Delta x)^2\\ 0 & 1/(\Delta x)^2 & -2/(\Delta x)^2\end{pmatrix}\begin{pmatrix}V_1\\V_2\\V_3\end{pmatrix}=-\frac{\rho}{\varepsilon}$$

Newton-Raphson Method

For initial conditions V(1)=Vs and V(N)=0

$$\begin{pmatrix} 1/(\Delta x)^2 & \cdots & \cdots \\ \vdots & \ddots & \vdots \\ \vdots & \cdots & 1/(\Delta x)^2 \end{pmatrix}\begin{pmatrix} V_1 \\ \vdots \\ V_N \end{pmatrix} = \begin{pmatrix} V_s/(\Delta x)^2 \\ \vdots \\ 0 \end{pmatrix} = \begin{pmatrix} Rho(1) \\ \vdots \\ Rho(N) \end{pmatrix}$$

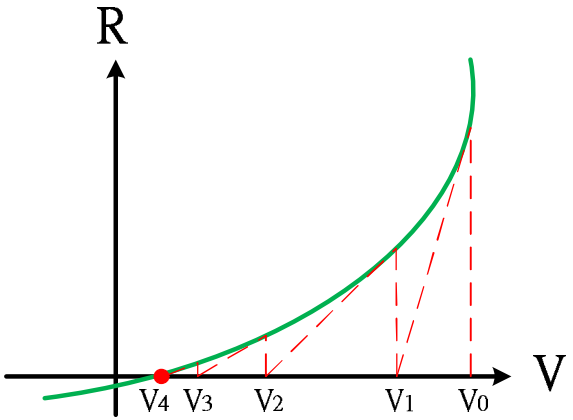

To get the initial V0

$$V_0 = \begin{pmatrix} V_1 \\ \vdots \\ V_N \end{pmatrix}_0 = \begin{pmatrix} 1/(\Delta x)^2 & \cdots & \cdots \\ \vdots & \ddots & \vdots \\ \vdots & \cdots & 1/(\Delta x)^2 \end{pmatrix}^{-1}\begin{pmatrix} Rho(1) \\ \vdots \\ Rho(N) \end{pmatrix}$$

For we have second-order differentail matrix A,

$AV_0 = Rho,$ where $Rho = -q_0 N_e / \varepsilon_0 \varepsilon_1$, and $N_e = -N_{ad} - N_{en} + N_{pn}$ (For n-MOSFETs)

$\rightarrow AV - Rho = 0,$ Let $AV - Rho = R \rightarrow$ Set initial conditions for R(1)=0 and R(N)=0

$\rightarrow \dfrac{\partial R}{\partial V} = A - \dfrac{\partial Rho}{\partial V} \rightarrow \because V_N = V_{N-1} + \dfrac{R}{\dfrac{\partial R}{\partial V}}$

And NR is a matrix to realize $\dfrac{\partial R}{\partial V}$, which is equal to $A - \dfrac{\partial Rho}{\partial V}$

$$\Delta V = \frac{R}{\dfrac{\partial R}{\partial V}} = \frac{R}{NR} \rightarrow V = V_0 + \Delta V$$

Outline

- Introduction
- **Numerical Technique and Physical Theory**
  - Time-independent Schrödinger Equation: Matrix Techniques
  - Six-band $k \cdot p$ Calculation for the Hole Subband Structure in p-MOSFETs
  - Newton-Raphson Method
  - Effective Mass Approximation (EMA)
- **Quantum Simulator NEP for the Two-dimensional Inversion-layers**
- **Hole Mobility**
- **Simulation Results and Discussion**
- **Conclusion**

Effective Mass Approximation

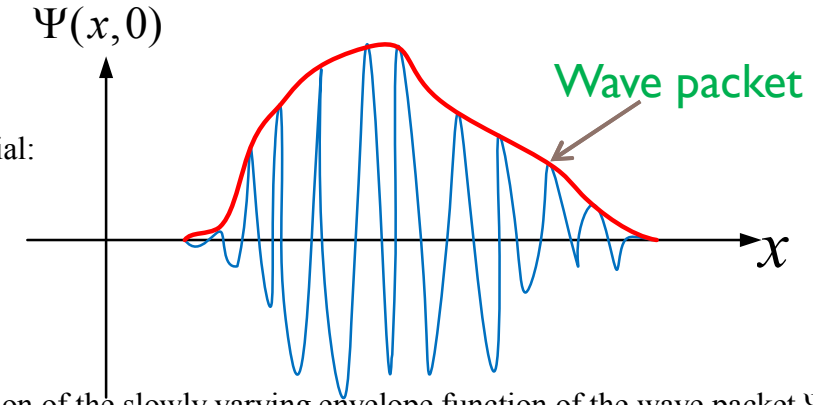

Considering the case in which one electron moves in a periodic potential:

$\psi_k(x) = e^{iKx}u_k(x)$ with the corresponding energy $E(k)$

A wave packet by linear combination:

$$\Psi(x,t) = \sum_k A(k)\psi_k(x,t)$$

$$= \sum_k A(k)\psi_k(x)e^{-i\frac{E(k)}{\hbar}t}$$

$$= \sum_k A(k)u_k(x)e^{i\left(kx-\frac{E(k)}{\hbar}t\right)}$$

Taylor expansions above equaitons:

$$E(k) \approx E(k_0) + (k-k_0)\left.\frac{dE(k)}{dk}\right|_{k=k_0} + \cdots$$

$$u_k(x) \approx u_{k0}(x) + (k-k_0)\left.\frac{du_k(x)}{dk}\right|_{k=k_0} + \cdots$$

Therefore :

$$\Psi(x,t) = \psi_{k0}(x,t)\cdot\sum_k A(k)\cdot e^{i(k-k_0)[x-\frac{E'(k_0)}{\hbar}t]}$$

$$\psi_{k0}(x,t) = u_{k0}(x)e^{i\left(k_0x-\frac{E(k_0)}{\hbar}t\right)}$$

From the motion of the slowly varying envelope function of the wave packet Ψ:

$$x - \frac{E'(k_0)}{\hbar}t \approx \text{constant}$$

$$\frac{d}{dt}x(t) - \frac{E'(k_0)}{\hbar} = 0$$

$$\boxed{v_g\big|_{k_0} \equiv \frac{d}{dt}x(t) = \frac{1}{\hbar}\left.\frac{dE(k)}{dk}\right|_{k_0}}$$

The time-varying wave vector:

$$k(t) = \frac{1}{\hbar}eFt + k_0$$

$$a \equiv \frac{dv_g(k)}{dt} = \frac{d}{dt}\frac{1}{\hbar}\frac{dE(k)}{dk} = \frac{1}{\hbar^2}\frac{d^2E(k)}{dk^2}\underbrace{\frac{d\hbar k}{dt}}_{\text{force}}$$

$$\boxed{m^* \equiv \left[\frac{1}{\hbar^2}\frac{d^2E(k)}{dk^2}\right]^{-1}}$$

Density-of-States Effective Mass and Quantization Effective Mass

Density-of-states (DOS) function:[3]

Mesh area= ΔKy*ΔKx

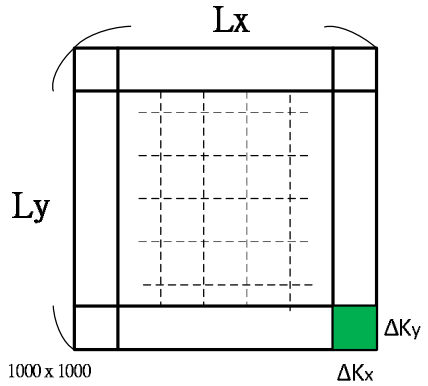

Cartesian Coordinate

Mesh area=dK* K*ɵ

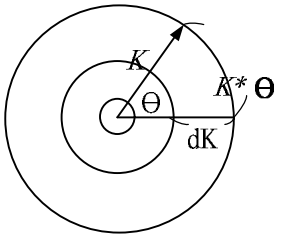

Polar Coordinate

Polar coordinate➔

$$DOS_j(E) = U(E - E_j)\frac{1}{(2\pi)^2}\int_0^{2\pi}\frac{K_j(E,\theta)}{\left|\frac{dE}{dK}\right|_{K_j(E,\theta)}}d\theta$$

Cartesian coordinate➔

$$DOS_j(E) = U(E - E_j)\frac{1}{(2\pi)^2}\times\frac{Area_j^{\text{k-space}}(E+dE) - Area_j^{\text{k-space}}(E)}{dE}$$

Therefore: $m_{DOS}^j(E) = 2\pi\hbar^2 \times DOS_j(E)$

Average density-of-states effective mass: $\left\langle m_{DOS}^j \right\rangle = \dfrac{\int m_{DOS}^j(E) f(E)\cdot DOS_j(E)dE}{\int f(E)\cdot DOS_j(E)dE}$

Quantization effective mass: $m_{QN}^j = \left(\frac{1}{E_j^{(0)}}\right)^3\left(\frac{\hbar^2}{2}\right)\left(\frac{3}{2}\pi e F_s(i+\frac{3}{4})\right)^2$

Outline

- Introduction
- Numerical Technique and Physical Theory
- **Quantum Simulator NEP for the Two-dimensional Inversion-layers**
  - Schrödinger and Poisson Self-consistent NEP in n-MOSFETs
  - Triangular Potential Well Approximation NEP in p-MOSFETs
  - Efficiently Boosted NEP in p-MOSFETs
  - Low Temperature Effect: Impurity Ionization Rate
- Hole Mobility
- Simulation Results and Discussion
- Conclusion

Outline

- Introduction
- Numerical Technique and Physical Theory
- **Quantum Simulator NEP for the Two-dimensional Inversion-layers**
  - Schrödinger and Poisson Self-consistent NEP in n-MOSFETs
  - Triangular Potential Well Approximation NEP in p-MOSFETs
  - Efficiently Boosted NEP in p-MOSFETs
  - Low Temperature Effect: Impurity Ionization Rate
- Hole Mobility
- Simulation Results and Discussion
- Conclusion

Schrödinger and Poisson Self-consistent NEP in n-MOSFETs

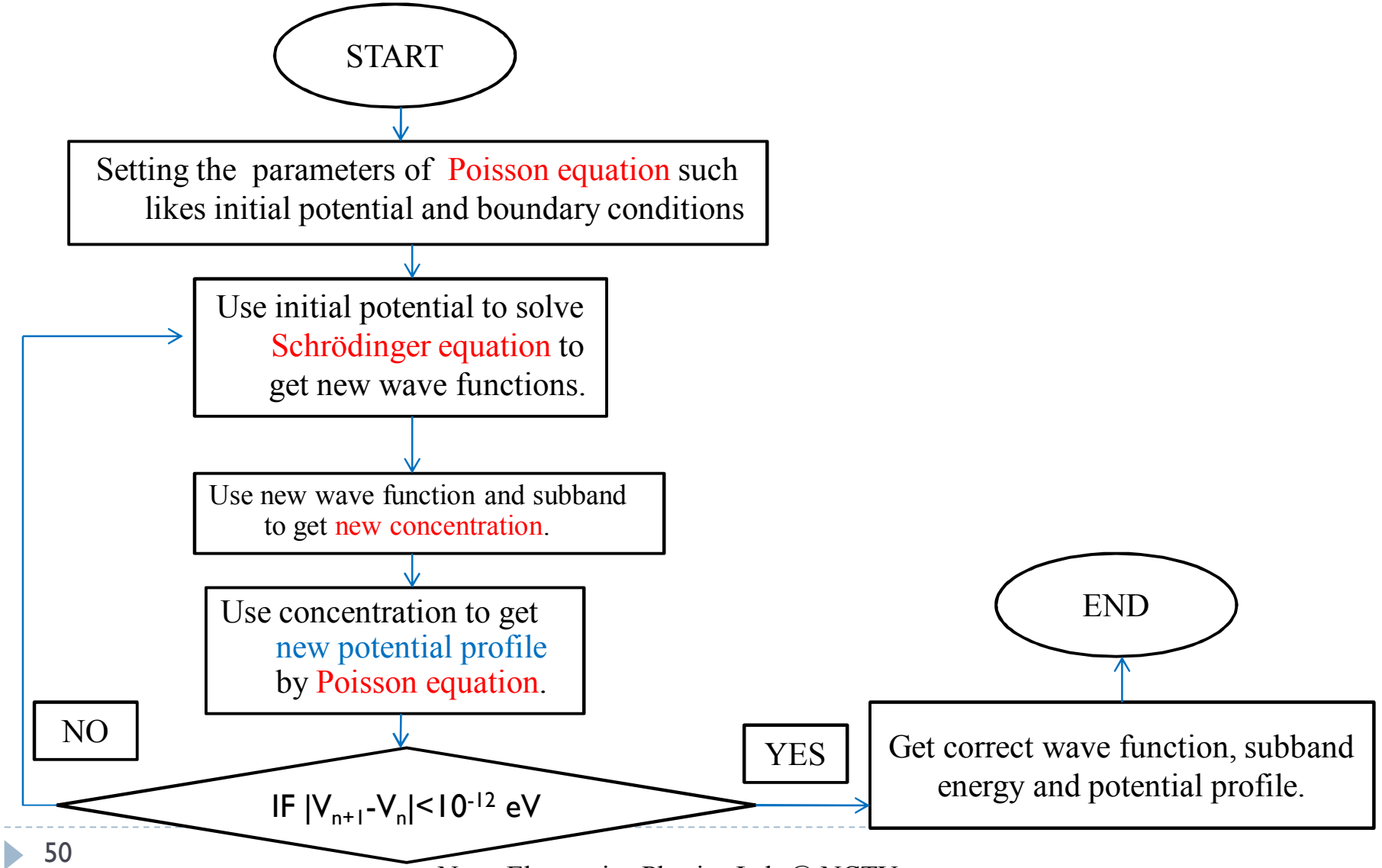

Schrödinger and Poisson Self-consistent NEP in n-MOSFETs

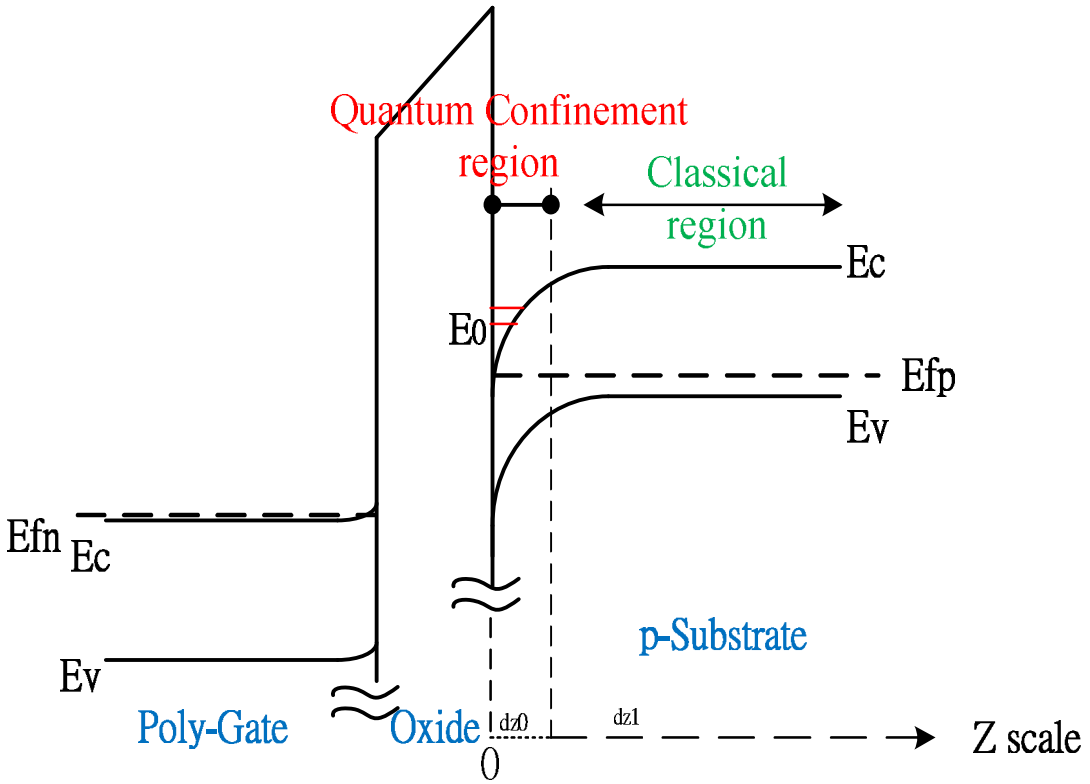

Quantum Confinement Region:

$$n(z)=\sum_{i,j} g_i \frac{m_{DOS}^{i}}{\pi\hbar^2} k_B T \ln\left(1+e^{\frac{E_f-E_{i,j}}{kT}}\right)\cdot\left|\Psi_{i,j}(z)\right|^2$$

$$p(z)=\sum_{v,j} g_v \frac{m_{DOS}^{v}}{\pi\hbar^2} k_B T \ln\left(1+e^{(\frac{E_{v,j}-E_f}{kT})}\right)\cdot\left|\Psi_{v,j}(z)\right|^2$$

Classical Region:

$$n(z)=n_0\cdot\exp(\frac{V(z)}{k_B T})$$

$$p(z)=p_0\cdot\exp(\frac{-V(z)}{k_B T})$$

Poisson Equation:

$$\frac{d^2V(z)}{dz}=-\frac{-q_0\cdot[-N_d^{+}(z)-n(z)+p(z)]}{\varepsilon_0\varepsilon_{si}}$$

Schrödinger and Poisson Self-consistent NEP in n-MOSFETs

The two-dimensional electron density:

$$n_{i,j} = g_i \frac{m_{DOS}^i}{\pi\hbar^2} k_B T \ln\left(1+\mathrm{e}^{\frac{E_f - E_{i,j}}{kT}}\right)$$

The total inversion layer charge density:

$$N_s = \sum_{i,j} n_{i,j}$$

The total inversion layer charge density:

$$Z_{av} = \sum_{i,j}\left[\frac{n_{i,j}}{N_s}\cdot\int_0^{bulk} z\cdot\left|\Psi_{i,j}(z)\right|^2 dz\right]$$

The flat band voltage:

$$V_{fb} = -k_B T \ln\left(\frac{N_{ploy}N_d}{n_i^2}\right)$$

The poly gate voltage and oxide voltage:

$$V_{poly} = -\frac{\varepsilon_{Si}F_s^2}{2eN_{poly}}$$

$$V_{ox} = \frac{t_{ox}\varepsilon_{Si}F_s}{\varepsilon_{ox}} \quad \text{where} \quad F_s = \frac{V_{(z=1)} - V_{(z=2)}}{\Delta z}$$

The gate voltage:

$$V_g = V_s + V_{ox} + V_{poly} + V_{fb}$$

Schrödinger and Poisson Self-consistent NEP in n-MOSFETs

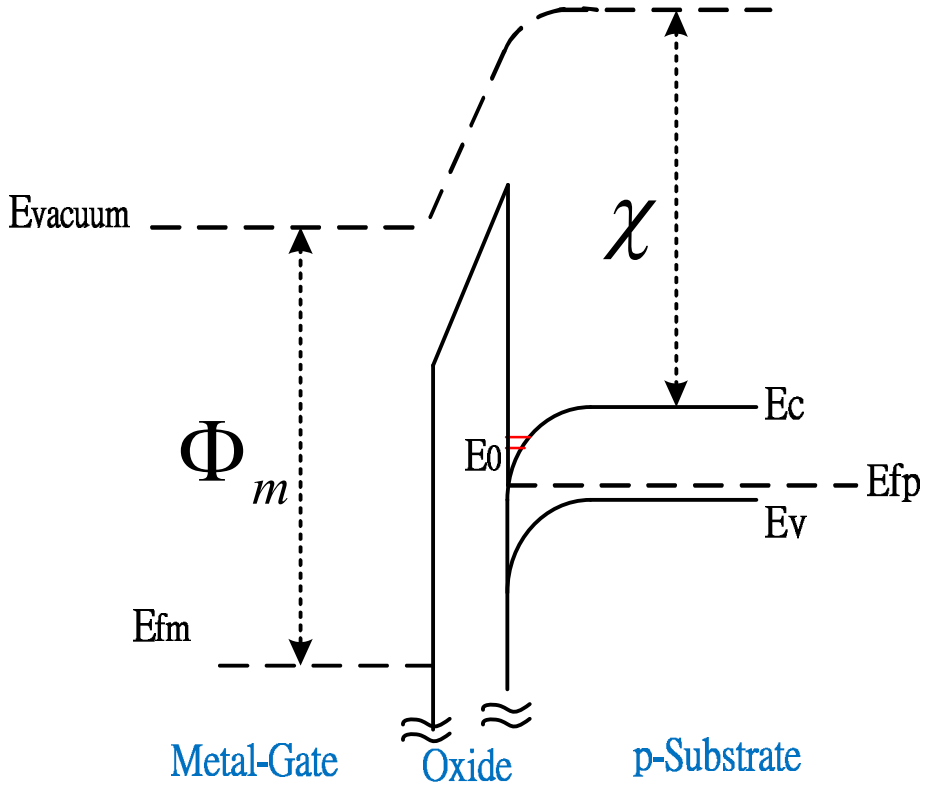

The flat band voltage:

$$V_{fb} = \Phi_m - \chi - E_g + kT \ln(\frac{N_V}{N_d})$$

The gate voltage:

$$V_g = V_{ox} + V_s + V_{fb}$$

Outline

- Introduction
- Numerical Technique and Physical Theory
- **Quantum Simulator NEP for the Two-dimensional Inversion-layers**
  - Schrödinger and Poisson Self-consistent NEP in n-MOSFETs
  - Triangular Potential Well Approximation NEP in p-MOSFETs
  - Efficiently Boosted NEP in p-MOSFETs
  - Low Temperature Effect: Impurity Ionization Rate
- Hole Mobility
- Simulation Results and Discussion
- Conclusion

Triangular Potential Well Approximation NEP in p-MOSFETs

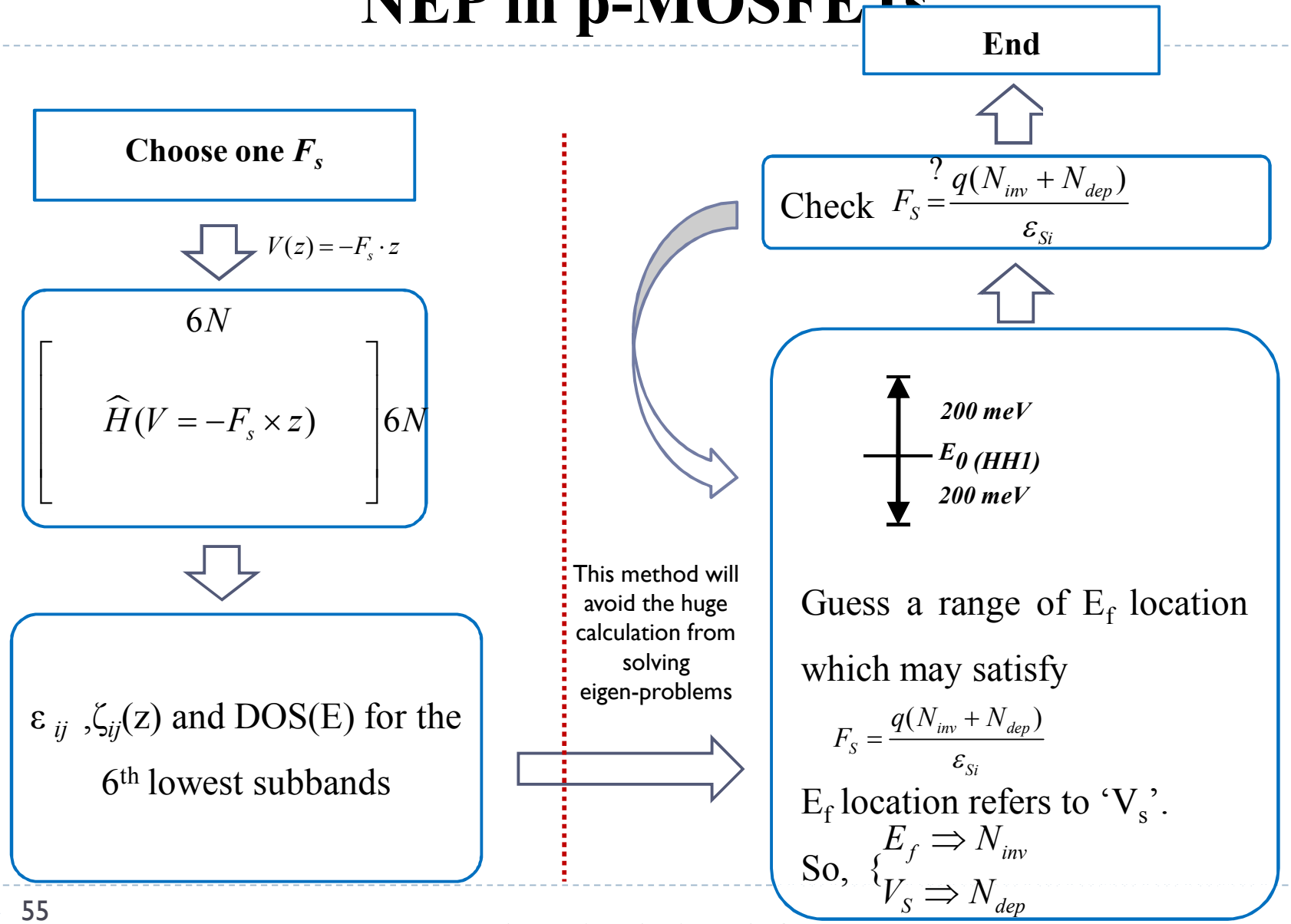

Triangular Potential Well Approximation
NEP in p-MOSFETs

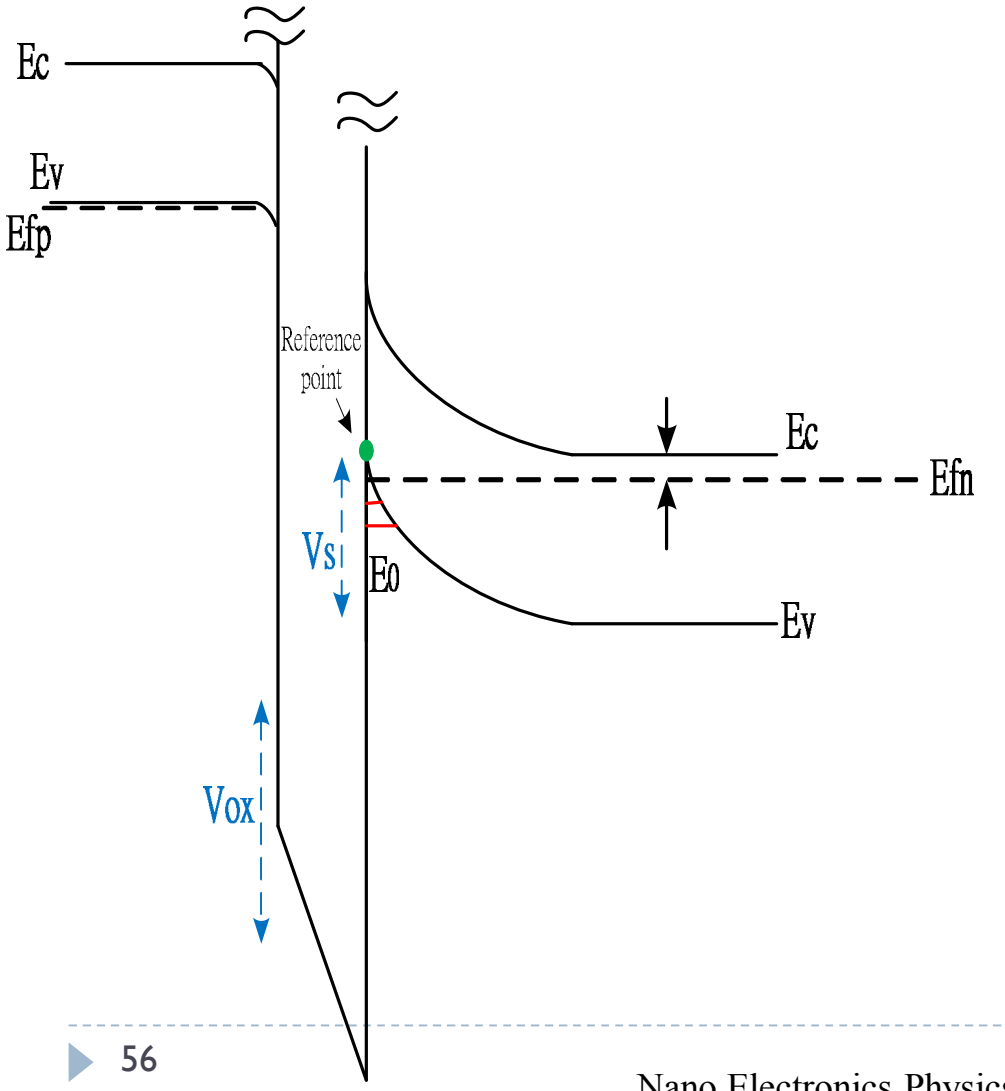

The surface and depletion band bending:

$$V_s = E_g - (E_c - E_f)_{Bulk} + E_f$$

$$V_{dep} = V_s - V_{inv} - k_B T$$

The depletion layer density:

$$p_{dep} = \sqrt{\frac{2\varepsilon_{Si} V_{dep} N_d}{e}}$$

The inversion band bending:

$$V_{inv} = \frac{e \cdot P_{inv} \cdot z_{av}}{\varepsilon_{Si}}$$

The electric field: $F_s^{\text{output}} = \dfrac{-e\left(P_{inv} + P_{dep}\right)}{\varepsilon_{si}}$

Outline

- Introduction
- Numerical Technique and Physical Theory
- **Quantum Simulator NEP for the Two-dimensional Inversion-layers**
  - Schrödinger and Poisson Self-consistent NEP in n-MOSFETs
  - Triangular Potential Well Approximation NEP in p-MOSFETs
  - Efficiently Boosted NEP in p-MOSFETs
  - Low Temperature Effect: Impurity Ionization Rate
- Hole Mobility
- Simulation Results and Discussion
- Conclusion

Efficiently Boosted NEP in p-MOSFETs

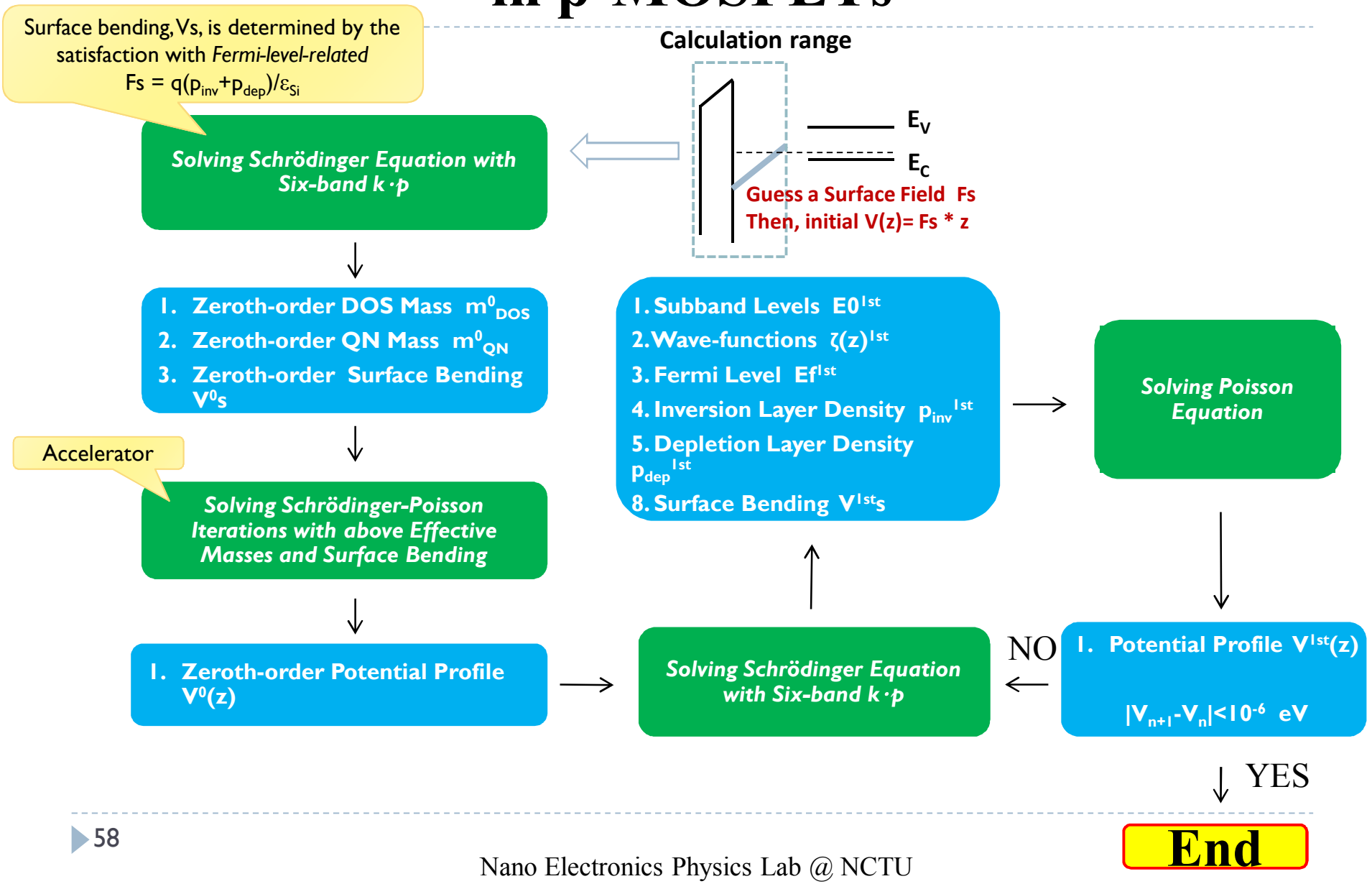

Efficiently Boosted NEP in p-MOSFETs

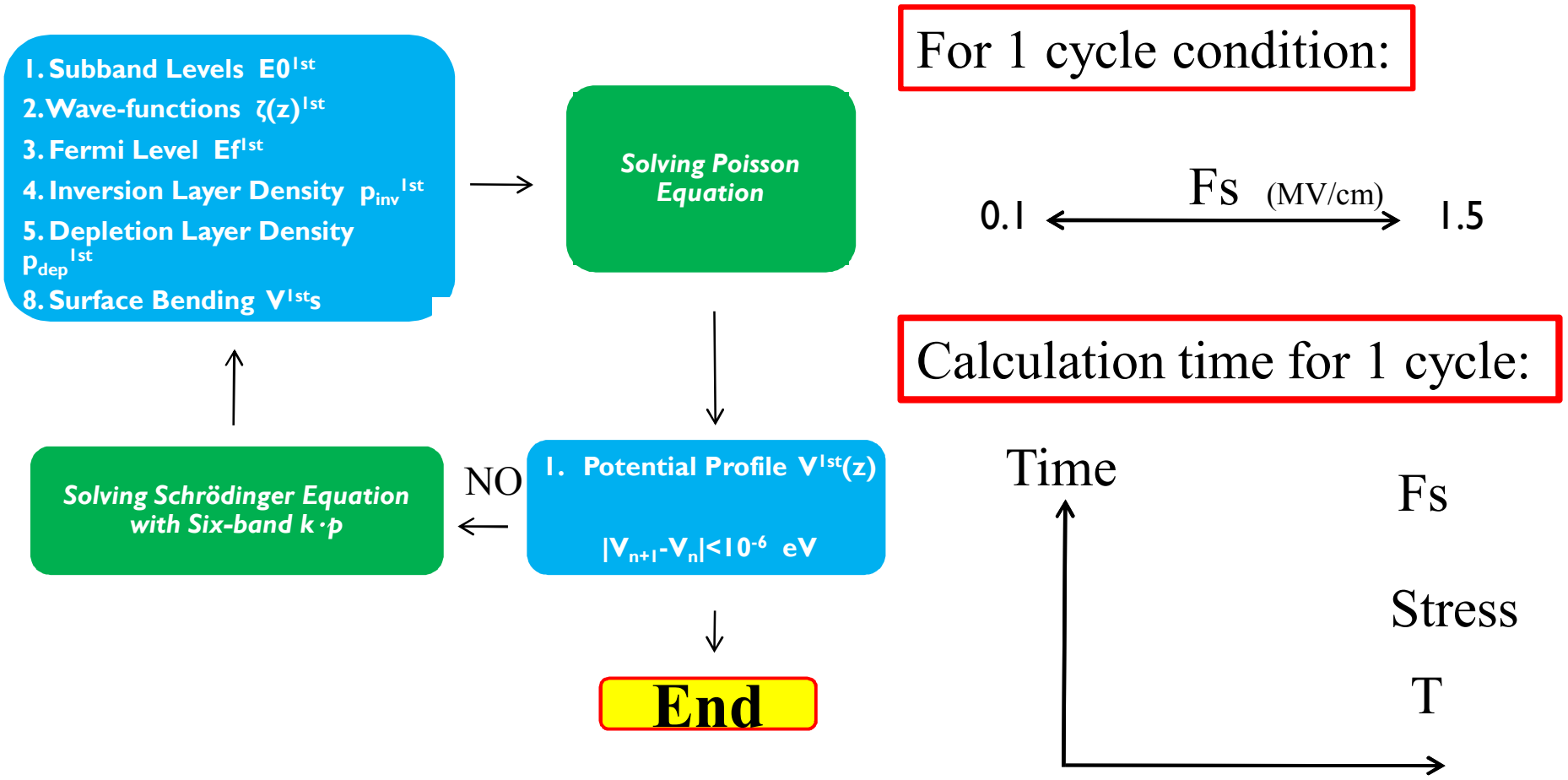

Outline

- Introduction
- Numerical Technique and Physical Theory
- **Quantum Simulator NEP for the Two-dimensional Inversion-layers**
  - Schrödinger and Poisson Self-consistent NEP in n-MOSFETs
  - Triangular Potential Well Approximation NEP in p-MOSFETs
  - Efficiently Boosted NEP in p-MOSFETs
  - Low Temperature Effect: Impurity Ionization Rate
- Hole Mobility
- Simulation Results and Discussion
- Conclusion

Low Temperature Effect:
Impurity Ionization Rate

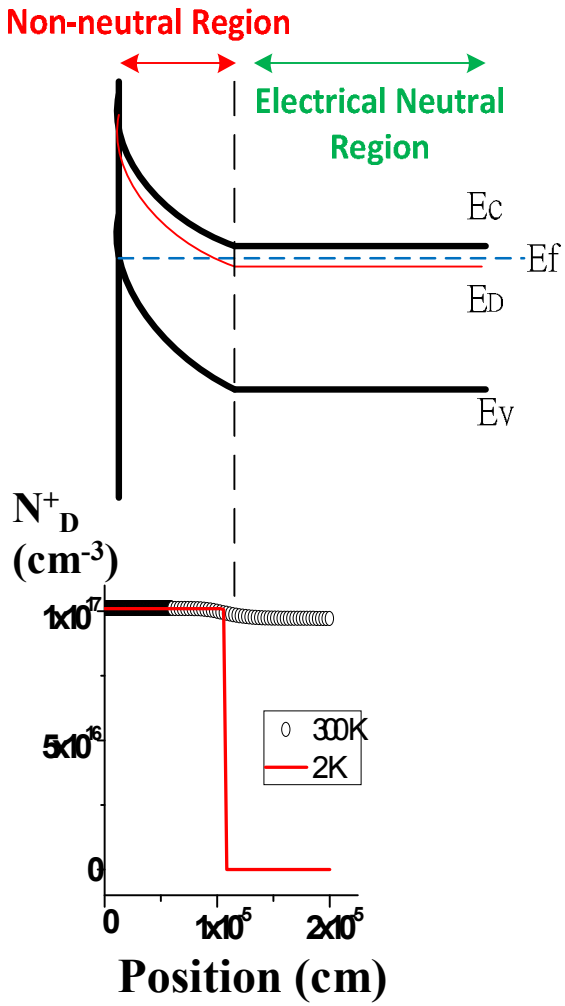

Electrical neutrality:

$$n = N_d^+ + p \qquad (1)$$

The ionized donors distribution:

$$N_d^+(z) = N_d \times \frac{1}{1 + 2e^{\left(\frac{E_D(z) - E_f}{k_B T}\right)}}$$

Therefore, Eq. (1) can be rewirtten as:

$$N_c \exp\left(-\frac{E_c - E_{f,Bulk}}{k_B T}\right) = N_D \times \frac{1}{1 + 2e^{\left(\frac{E_{D,Bulk} - E_{f,Bulk}}{k_B T}\right)}} + N_v \exp\left(\frac{E_v - E_{f,Bulk}}{k_B T}\right)$$

we have to face meaningless value and inaccurate approximation from simulator.

So we use Fermi-Dirac integral rather than Boltzmann statistics case as below:

- In non-neutral region:

$$Q_{net}(z) = N_D^+(z) - N_C \frac{2}{\sqrt{\pi}} F_{1/2}\left(\frac{E_C(z) - E_f}{k_B T}\right) + N_V \frac{2}{\sqrt{\pi}} F_{1/2}\left(\frac{E_f - E_V(z)}{k_B T}\right)$$

- Electrical neutral region:

$$Q_{net}(z) = N_D^+(z) - N_C e^{-\frac{E_f - E_{C0}}{k_B T}} + N_V e^{-\frac{E_{V0} - E_f}{k_B T}}$$

Outline

- Introduction
- Numerical Technique and Physical Theory
- Quantum Simulator NEP for the Two-dimensional Inversion-layers
- **Hole Mobility**
  - Phonon Scattering
  - Surface Roughness Scattering
  - Derivation of Two-Dimensional Mobility
- Simulation Results and Discussion
- Conclusion

Phonon Scattering Rate

For the acoustic phonon, the isotropic relaxation time in the subband μ to ν [3]:

$$\frac{1}{\tau_{ac}^{(\mu)}(K)} \approx \frac{2\pi \bullet k_B T \bullet D_{ac}^2}{\hbar \rho u_l^2} \sum_{\nu} F_{\mu\nu} \bullet DOS_{\nu}[E_{\mu}(K)]$$

$$= \frac{k_B T \bullet D_{ac}^2}{\hbar^3 \rho u_l^2} \sum_{\nu} F_{\mu\nu} \bullet m_{DOS(\nu)}[E_{\mu}(K)]$$

For the optical phonon, the scattering rate [3]:

$$\frac{1}{\tau_{op}^{(\mu)}(K)} \approx \frac{\pi \bullet D_{op}^2}{\rho \varpi_{op}} \sum_{\nu} F_{\mu\nu} \bullet DOS_{\nu}[E_{\mu}(K) \mp E_K] \times \frac{1 - f_0[E_{\mu}(K) \mp E_K]}{1 - f_0[E_{\mu}(K)]} \times (n_{op} + \frac{1}{2} \pm \frac{1}{2})$$

$$= \frac{D_{op}^2}{2\hbar \rho E_K} \sum_{\nu} F_{\mu\nu} \bullet m_{DOS(\nu)}[E_{\mu}(K) \mp E_K] \times \frac{1 - f_0[E_{\mu}(K) \mp E_K]}{1 - f_0[E_{\mu}(K)]} \times (n_{op} + \frac{1}{2} \pm \frac{1}{2})$$

$\{$ +: phonon emission
- : phonon absorption

$F_{\mu\nu}$ is the form factor determined by the wavefunctions of the μ-th subband and the ν-th subbands

$$F_{\mu\nu} = \int_0^W \left| \xi_0^{(\mu)}(z) \bullet \xi_0^{(\nu)}(z) \right|^2 dz$$

n_{op} is the occupation number

$$n_{op} = \frac{1}{[\exp(\frac{E_K}{k_B T}) - 1]}$$

Surface Roughness Scattering Rate

Assumption that the single subband approximation [12]:

$$\frac{1}{\tau_G(E)} = \frac{m_{DOS}(E)\bullet e^2 \bullet E_{eff}^2 \bullet \Delta^2 \bullet \Lambda^2}{2\hbar^3} \int_0^{2\pi} e^{\frac{-q^2\Lambda^2}{4}} \bullet (1-\cos\theta) d\theta$$

$$= \frac{m_{DOS,j}(E)\bullet e^2 \bullet E_{eff}^2 \bullet \Delta^2 \bullet \Lambda^2}{2\times 2\hbar^3} \int_0^{2\pi} e^{\frac{-q^2\Lambda^2}{4}} \bullet (1-\cos\theta) d\theta \qquad \text{[excluding spin]}$$

where

$$q^2 = |k_i|^2 + |k_j|^2 - 2|k_i|\cdot|k_j|\cos\theta = 2k^2(1-\cos\theta)$$

$$k^2 = \frac{2m_{DOS,j}\cdot(E-E_j)}{\hbar^2}$$

$$E_{eff} = \frac{e\cdot(P_{dep} + \frac{1}{3}P_{inv})}{\varepsilon_{si}}$$

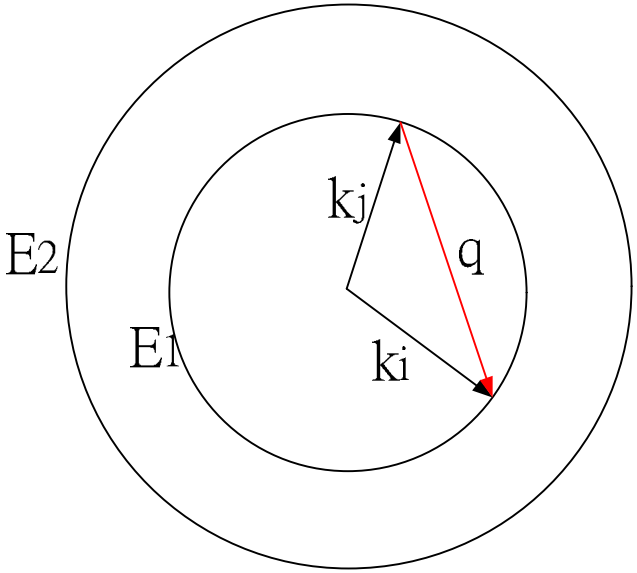

Two-Dimensional Mobility

Derivation of Two-Dimensional Mobility from Fischetti's [3]:

$$\mu_{xx}^{v} = \frac{e}{4\pi^2\hbar^2 k_B T n_{vs}} \int_0^{2\pi} d\phi \int_{E_v}^{\infty} dE \frac{K_v(E,\phi)}{(\frac{\partial E}{\partial K})} (\frac{\partial E}{\partial k_x})^2 \tau_v(E) f_0(E)[1-f_0(E)]$$

$$\text{Let : Velocity}_{\text{G}}(\text{E}) = \sum_{\text{k=states}} \text{v}_{\text{g,k}}^2(E)$$

$$\mu_{xx} = \sum_{v=1}^{6} N^v \times \mu_{xx}^{v}$$

$$= \frac{e}{4\pi^2\hbar^2 k_B T n_s} \sum_{v=1}^{6} \int_0^{2\pi} d\phi \int_{E_v}^{\infty} dE \frac{K_v(E,\phi)}{(\frac{\partial E}{\partial K})} (\frac{\partial E}{\partial k_x})^2 \tau_v(E) f_0(E)[1-f_0(E)]$$

$$= \frac{e}{k_B T n_s} \sum_{v=1}^{6} \int_{E_v}^{\infty} dE \cdot \text{Velocity}_{\text{G}}(\text{E}) \times DOS_v(E) \times \tau_v(E) f_0(E)[1-f_0(E)]$$

$$\boxed{\mu_{xx} = \frac{e}{2\pi\hbar^2 k_B T n_s} \sum_{v=1}^{6} \int_{E_v}^{\infty} dE \cdot \text{Velocity}_{\text{G}}(\text{E}) \times m_{DOS}(E) \times \tau_v(E) f_0(E)[1-f_0(E)]}$$

It is important that we avoid using Matthiessen's rule to calculate inaccurate total mobility which may cause scattering parameter shift. $\frac{1}{\tau_{total}(E)} = \frac{1}{\tau_{phonon}(E)} + \frac{1}{\tau_{SR}(E)}$

Outline

- Introduction
- Numerical Technique and Physical Theory
- Quantum Simulator NEP for the Two-dimensional Inversion-layers
- Hole Mobility
- **Simulation Results and Discussion**
  - n-MOSFETs
  - p-MOSFETs with Triangular Potential Well Approximation
  - Efficiently Boosted Model in p-MOSFETs
  - Density-of-States and Quantization Effective Mass
  - Mobility
- Conclusion

Outline

- Introduction
- Numerical Technique and Physical Theory
- Quantum Simulator NEP for the Two-dimensional Inversion-layers
- Hole Mobility
- **Simulation Results and Discussion**
  - n-MOSFETs
  - p-MOSFETs with Triangular Potential Well Approximation
  - Efficiently Boosted Model in p-MOSFETs
  - Density-of-States and Quantization Effective Mass
  - Mobility
- Conclusion

n-MOSFETs comparison with Schred[1]

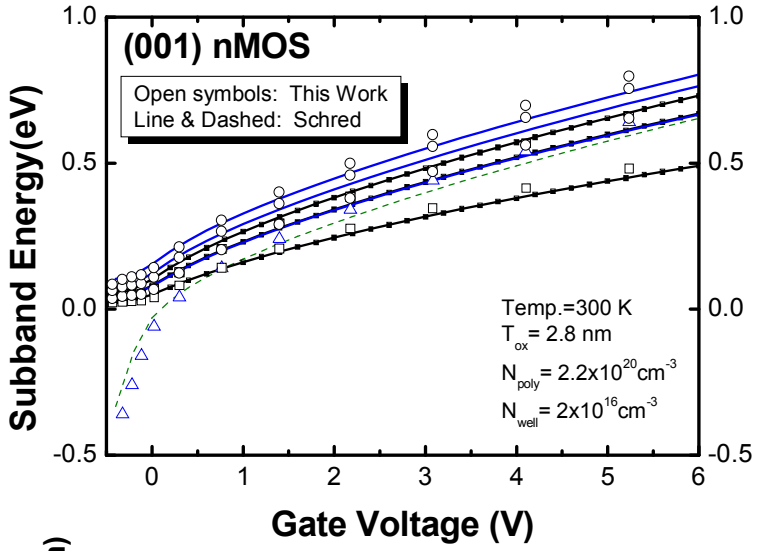

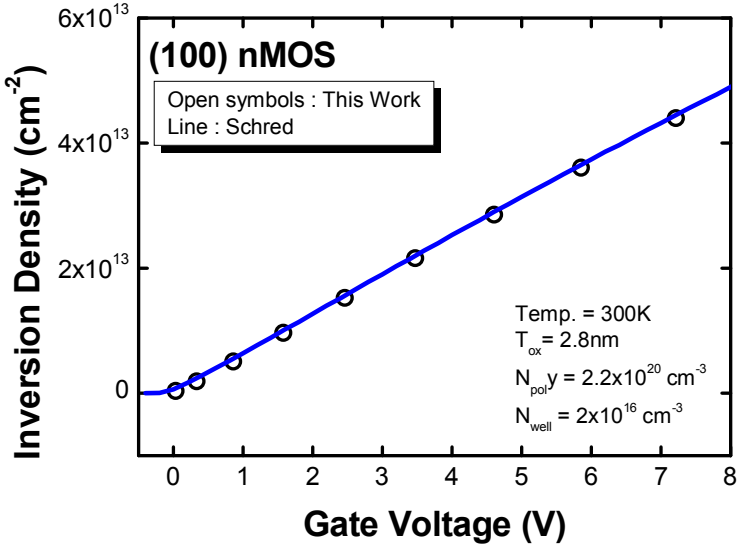

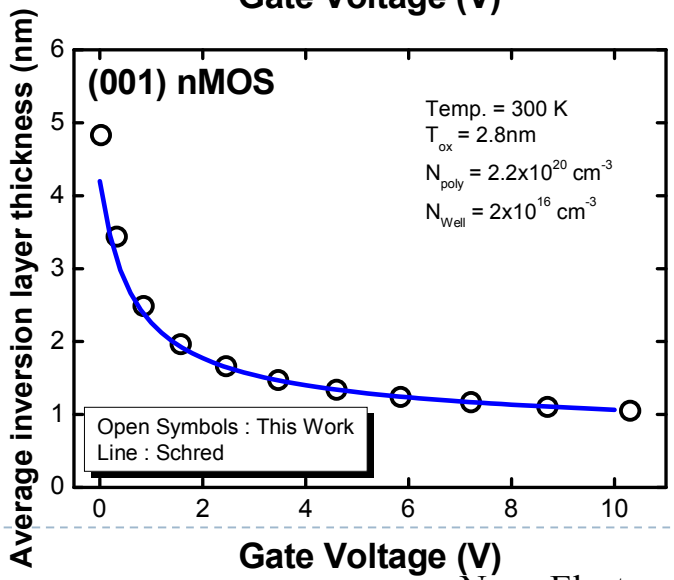

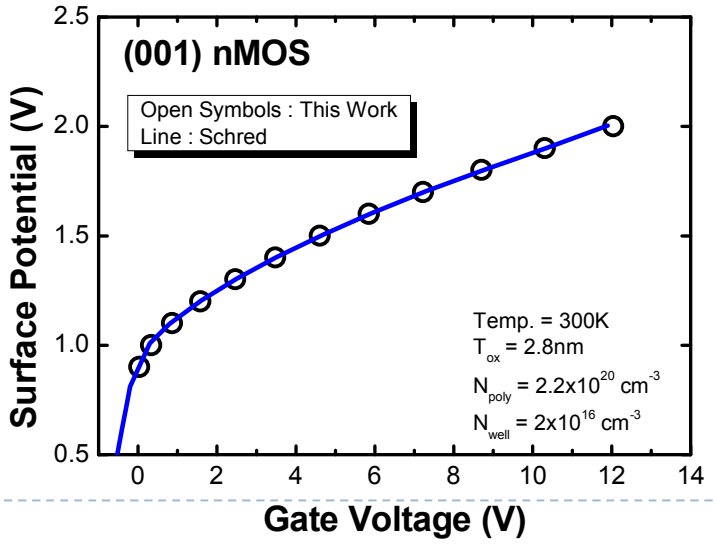

Metal/SiO_2/p-Si comparison with Schred[1]

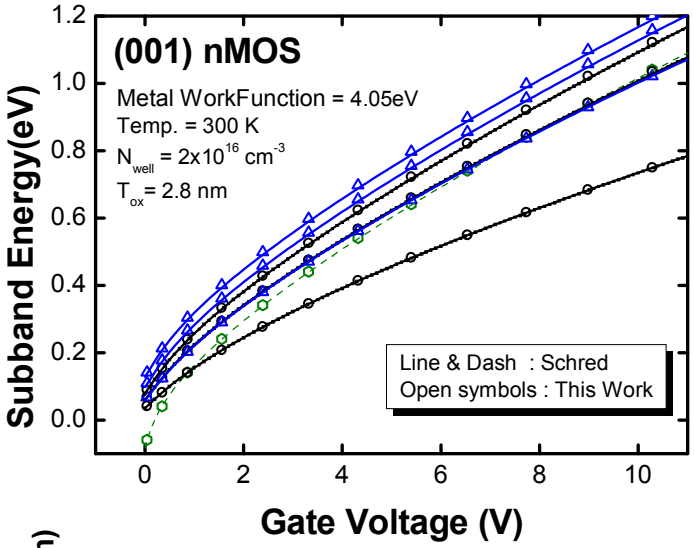

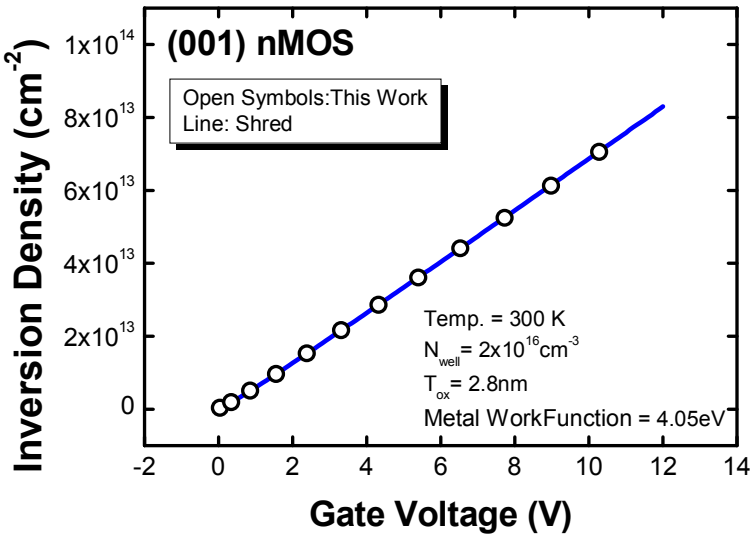

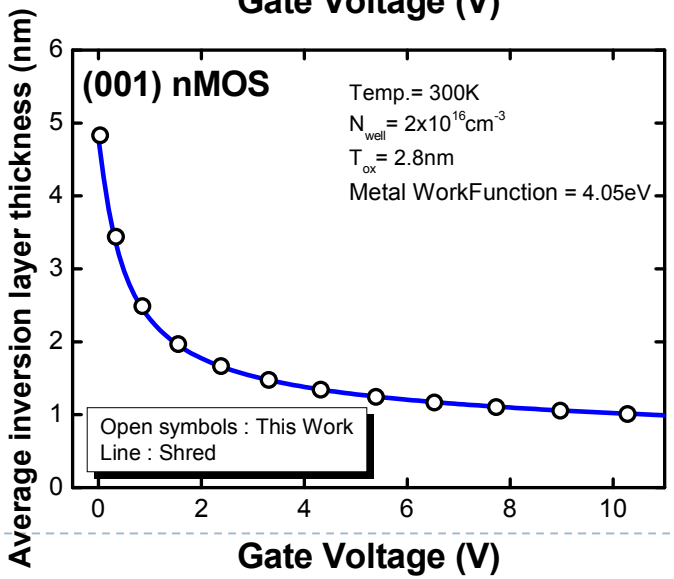

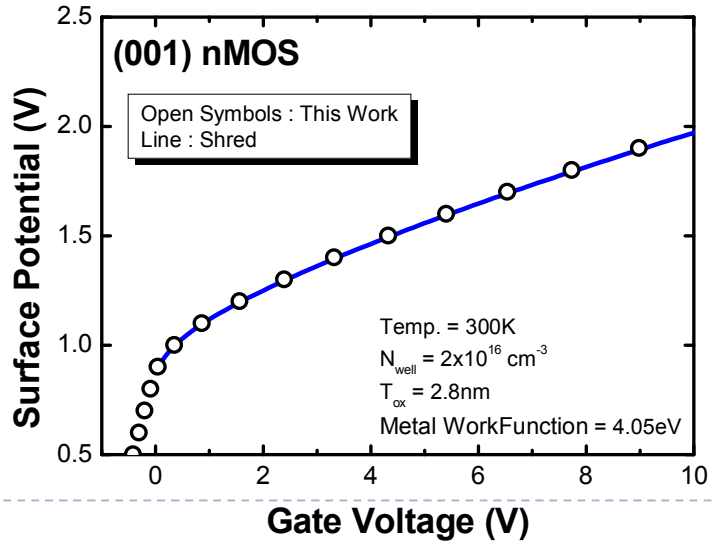

Outline

- Introduction
- Numerical Technique and Physical Theory
- Quantum Simulator NEP for the Two-dimensional Inversion-layers
- Hole Mobility
- **Simulation Results and Discussion**
  - n-MOSFETs
  - p-MOSFETs with Triangular Potential Well Approximation
  - Efficiently Boosted Model in p-MOSFETs
  - Density-of-States and Quantization Effective Mass
  - Mobility
- Conclusion

(001) p-MOSFETs

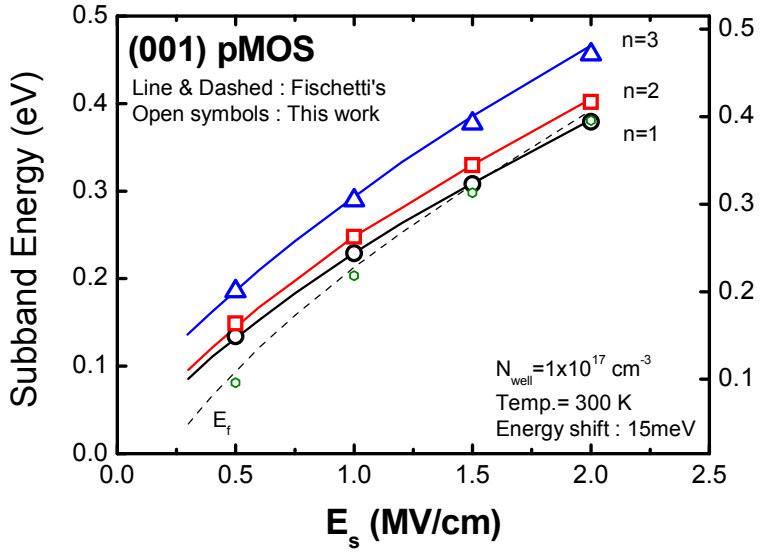

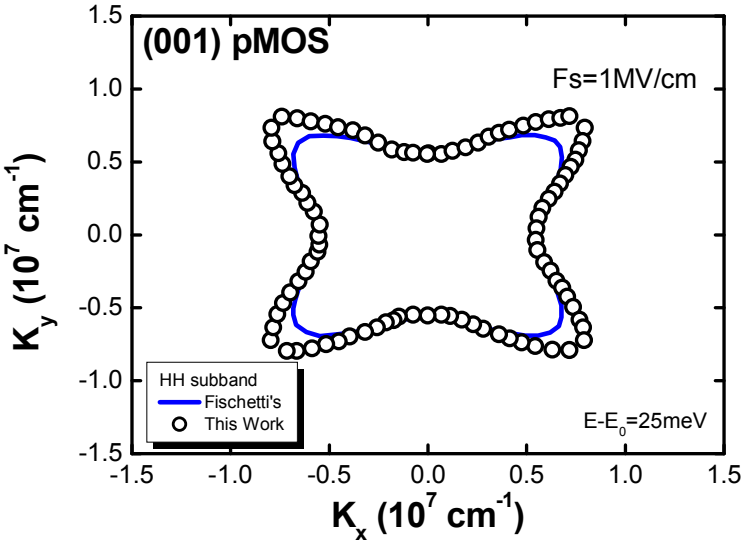

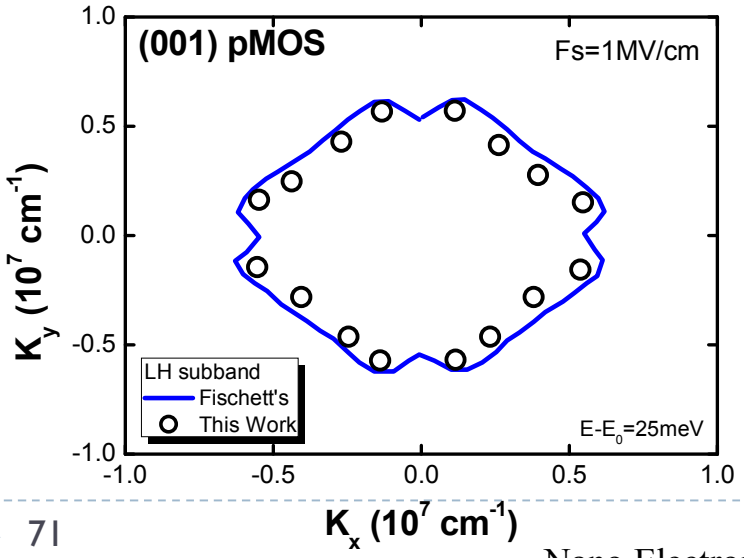

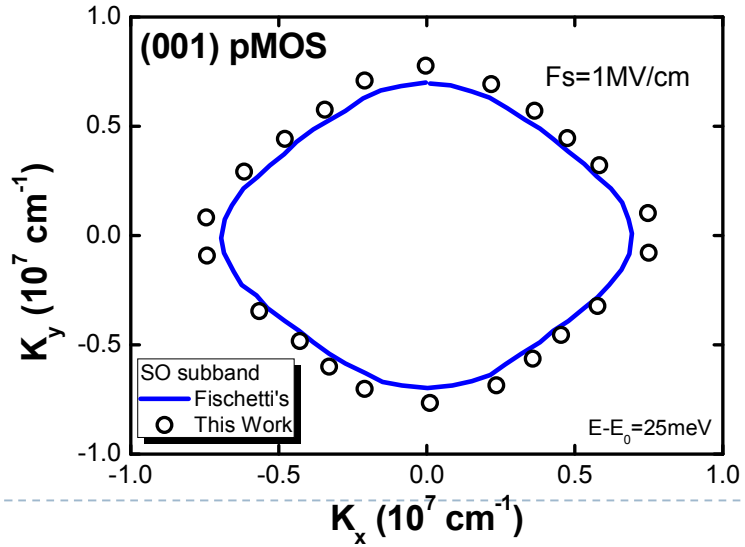

(011) p-MOSFETs

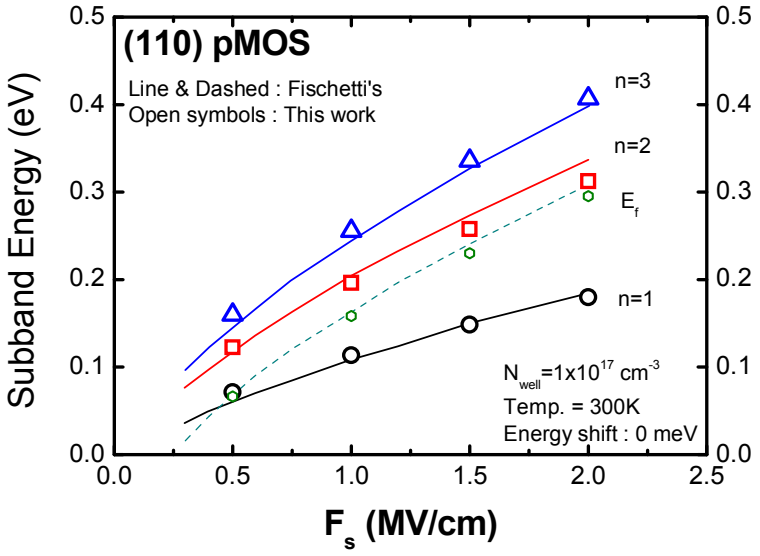

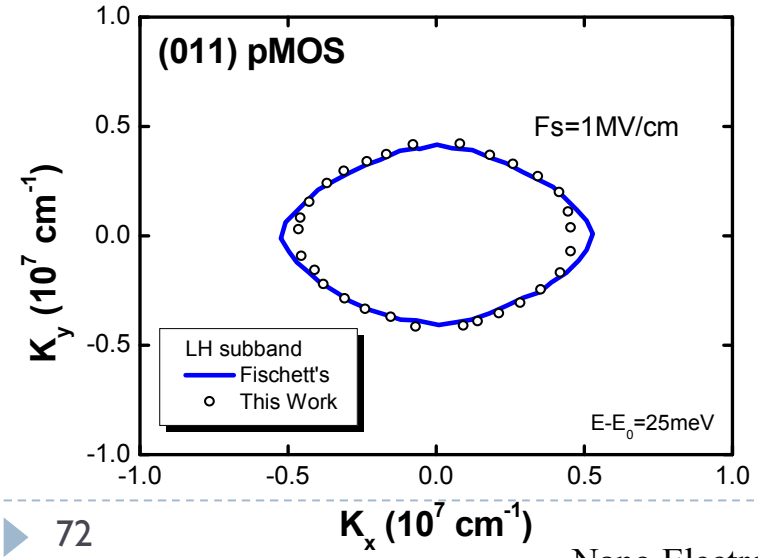

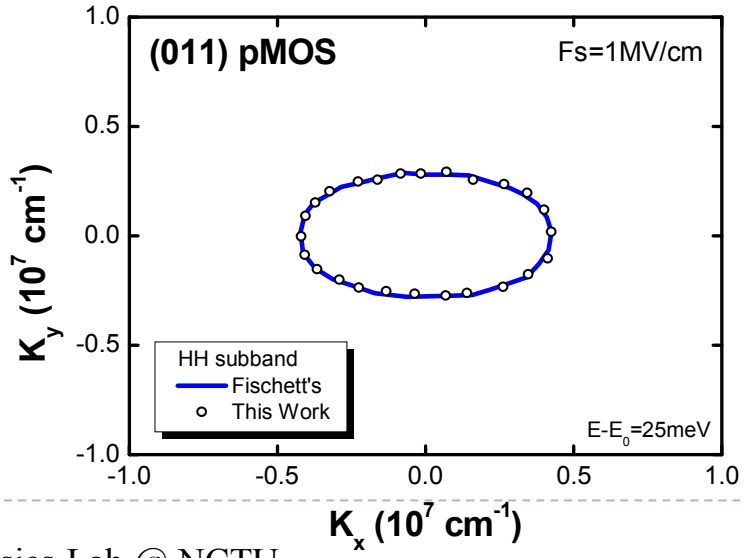

(111) p-MOSFETs

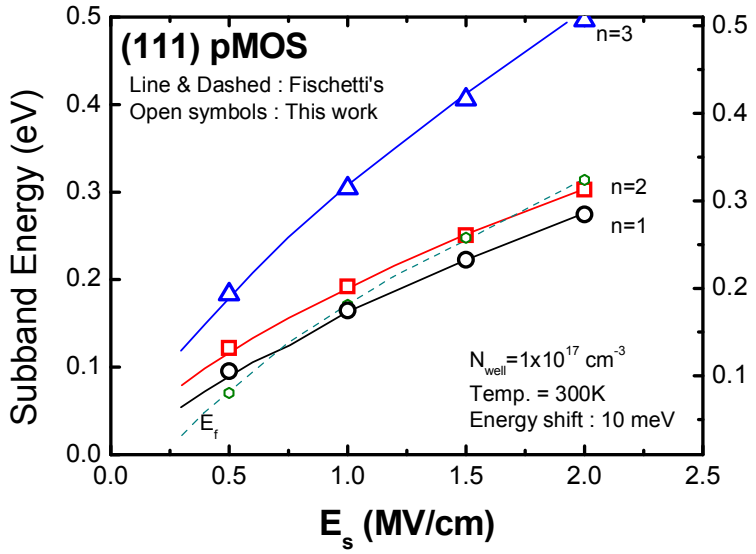

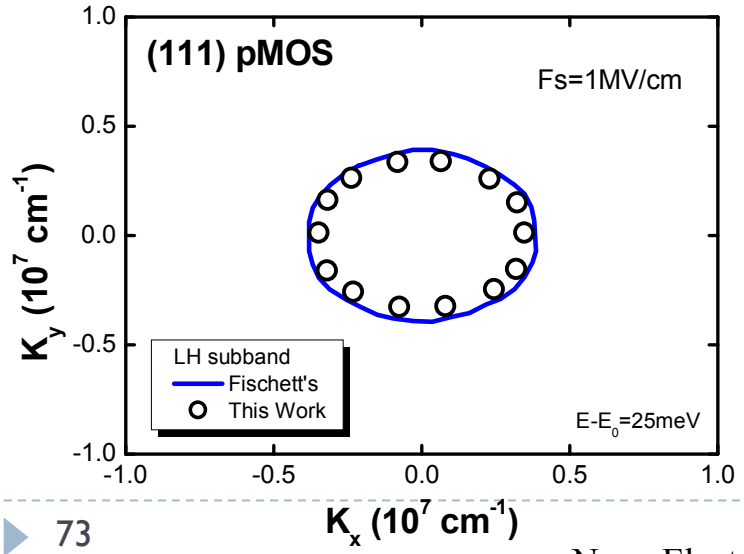

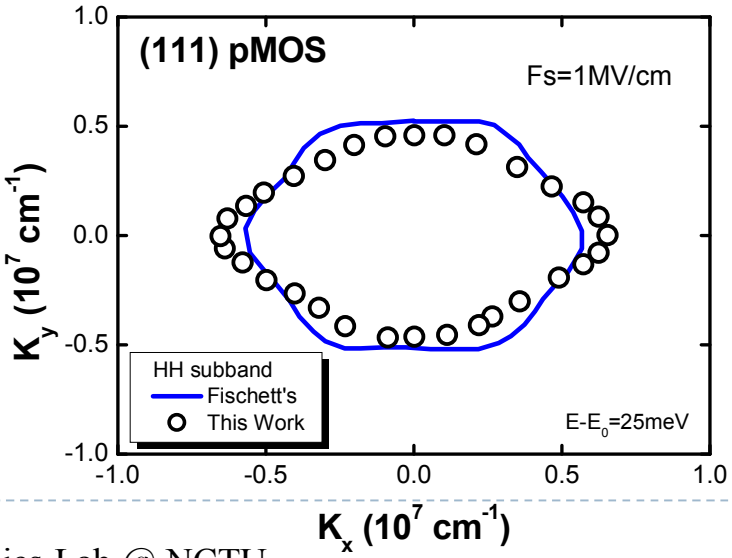

(001) p-MOSFETs

1% in-plane tensile stress

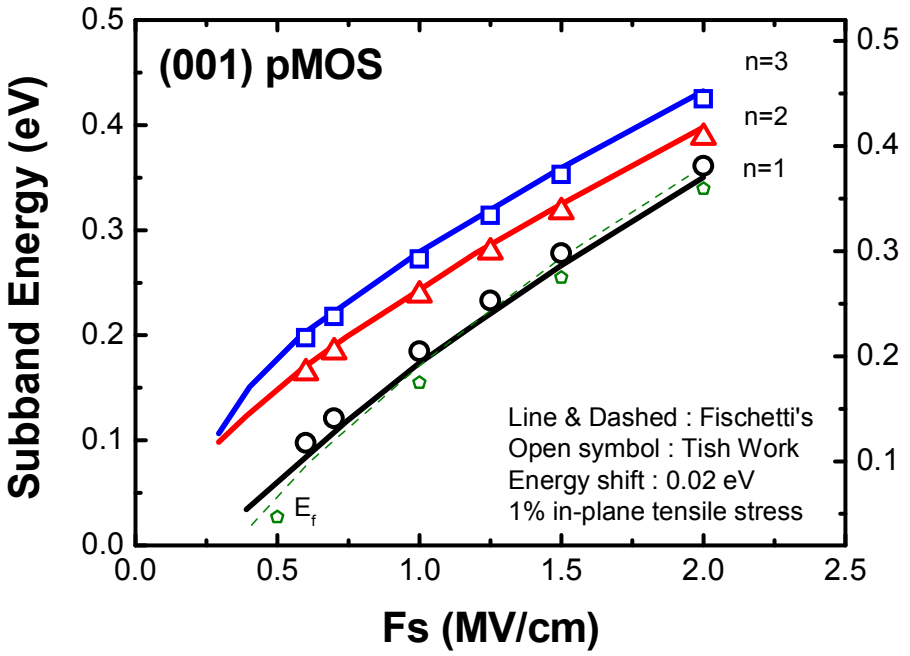

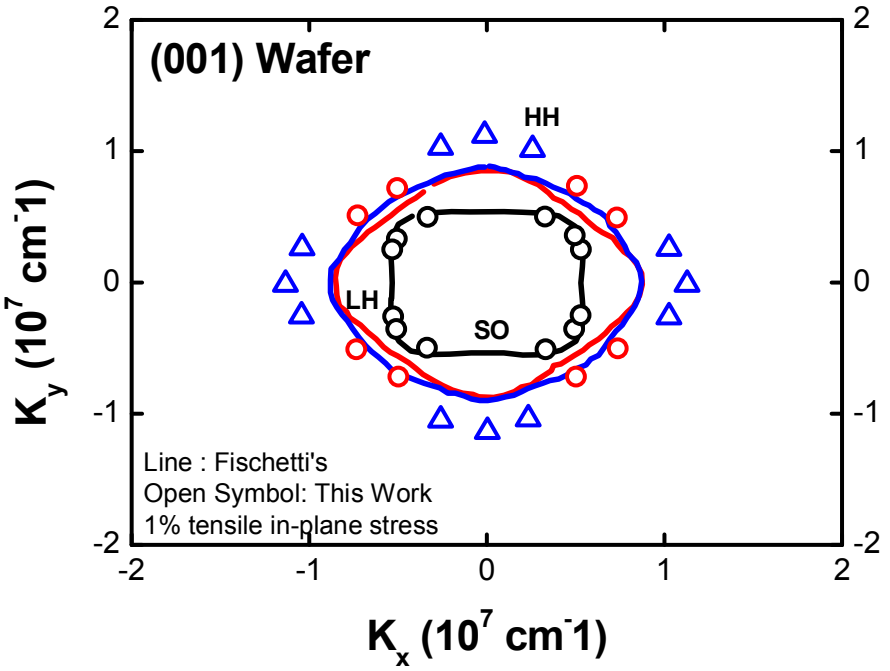

(001) p-MOSFETs

1% in-plane compressive stress

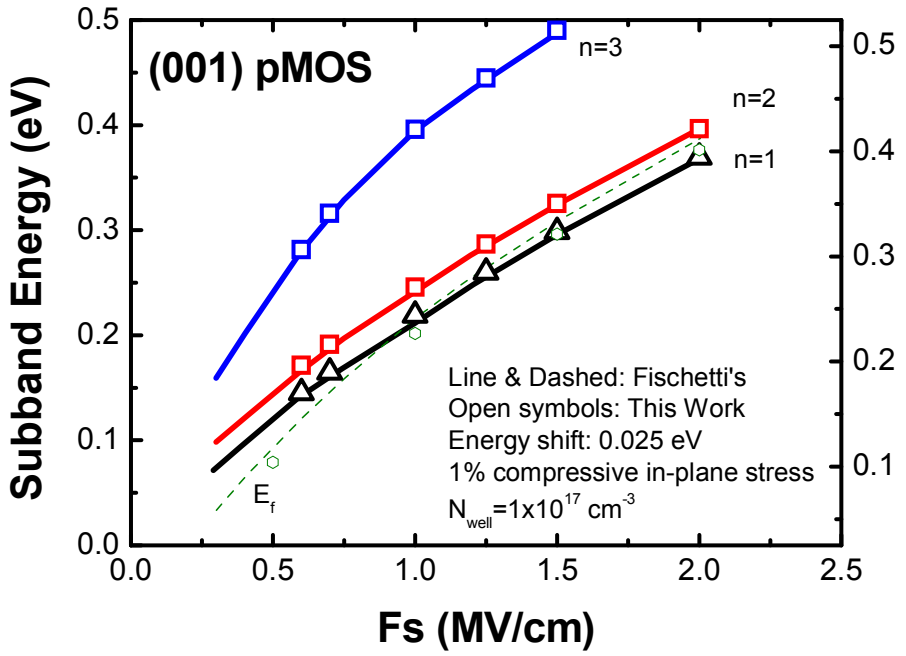

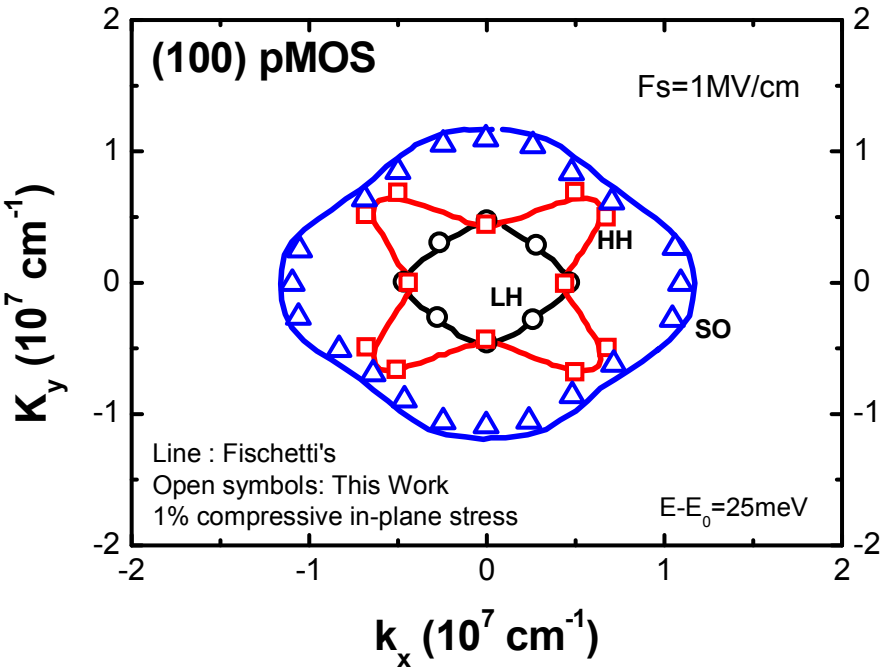

Outline

- Introduction
- Numerical Technique and Physical Theory
- Quantum Simulator NEP for the Two-dimensional Inversion-layers
- Hole Mobility
- **Simulation Results and Discussion**
  - n-MOSFETs
  - p-MOSFETs with Triangular Potential Well Approximation
  - Efficiently Boosted Model in p-MOSFETs
  - Density-of-States and Quantization Effective Mass
  - Mobility
- Conclusion

p-MOSFETs for (001) and (011)

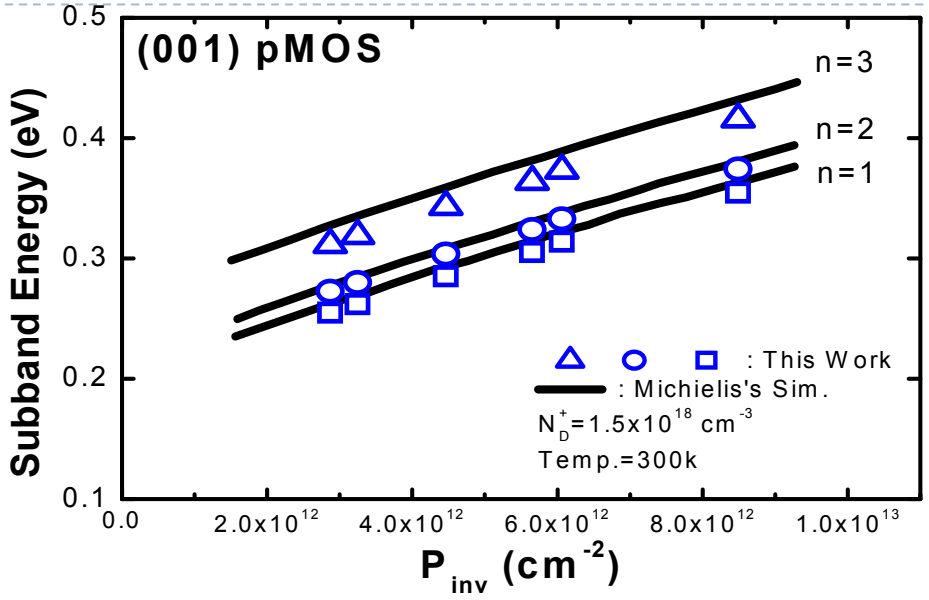

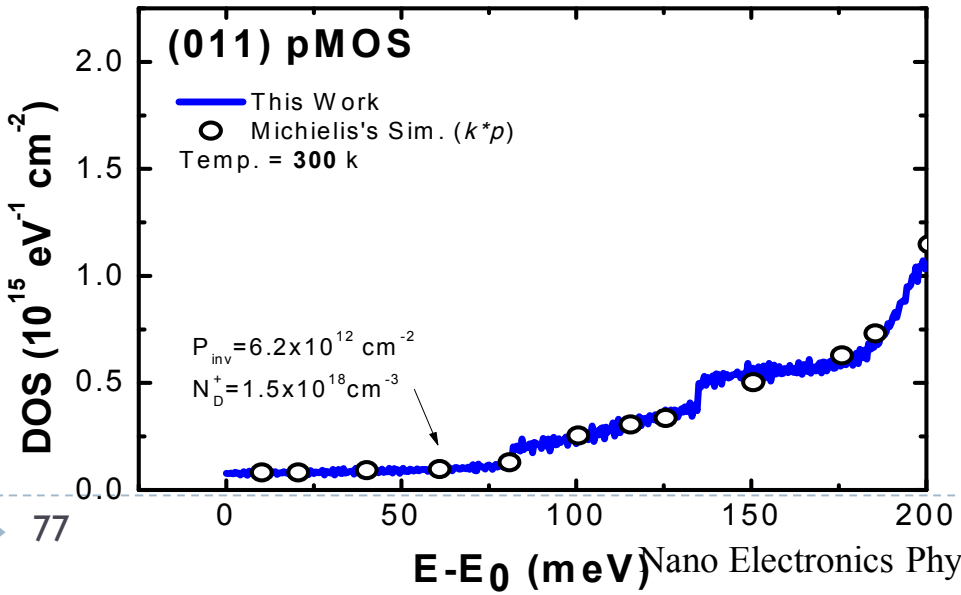

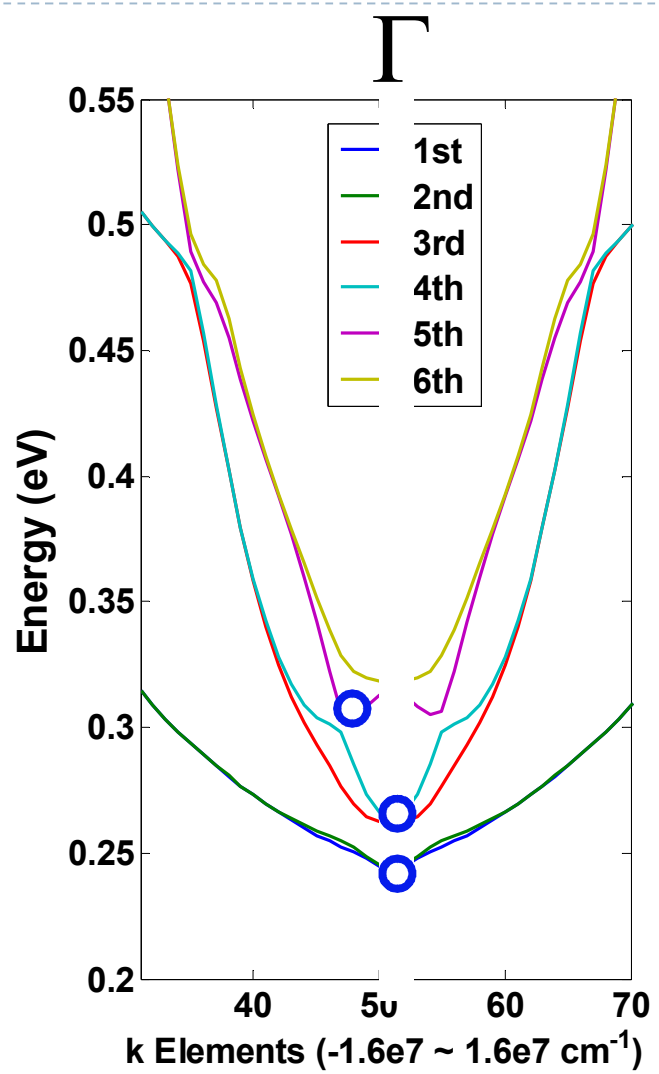

p-MOSFETs for (001)

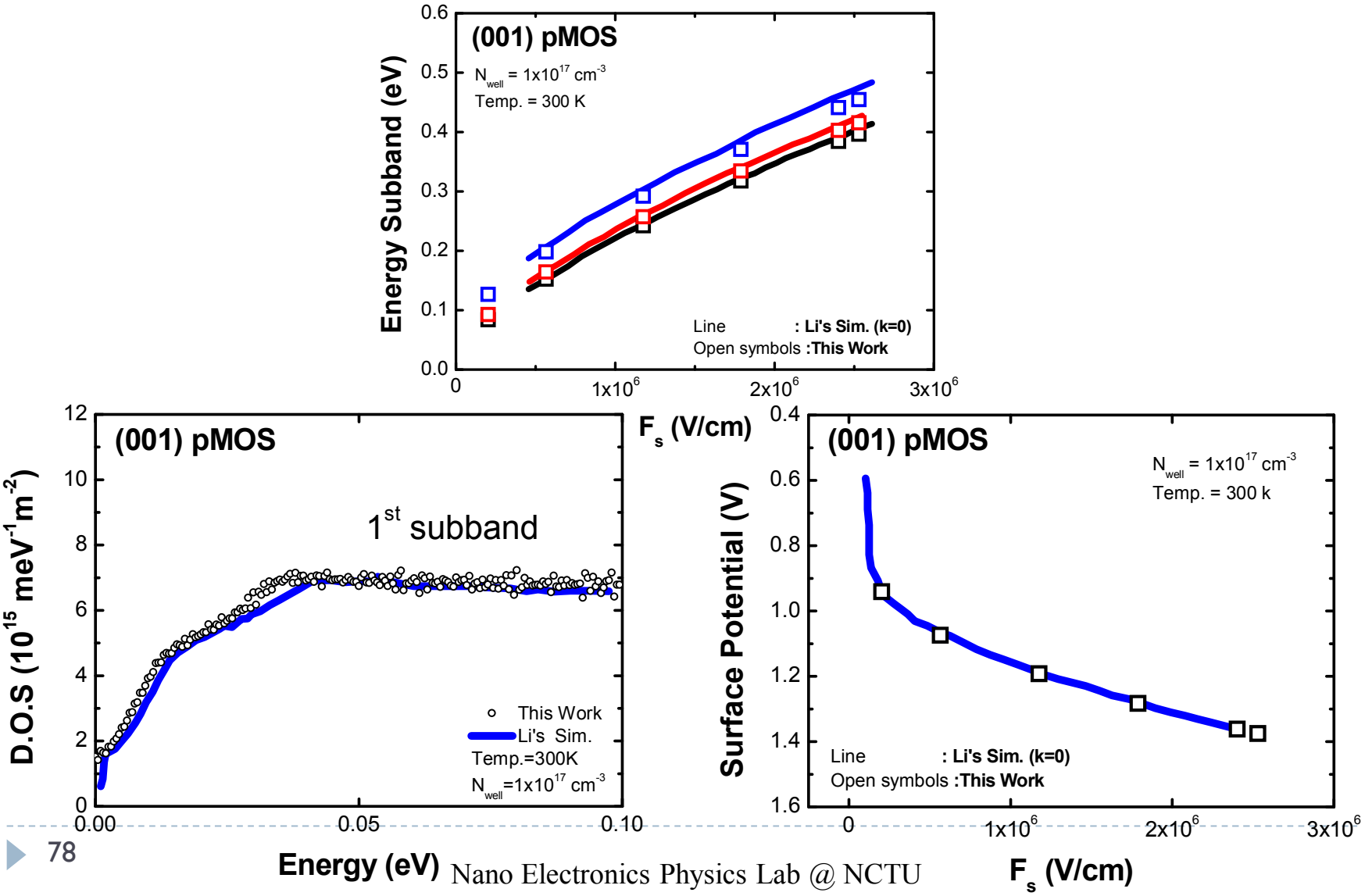

Subband and m_{DOS} Comparison

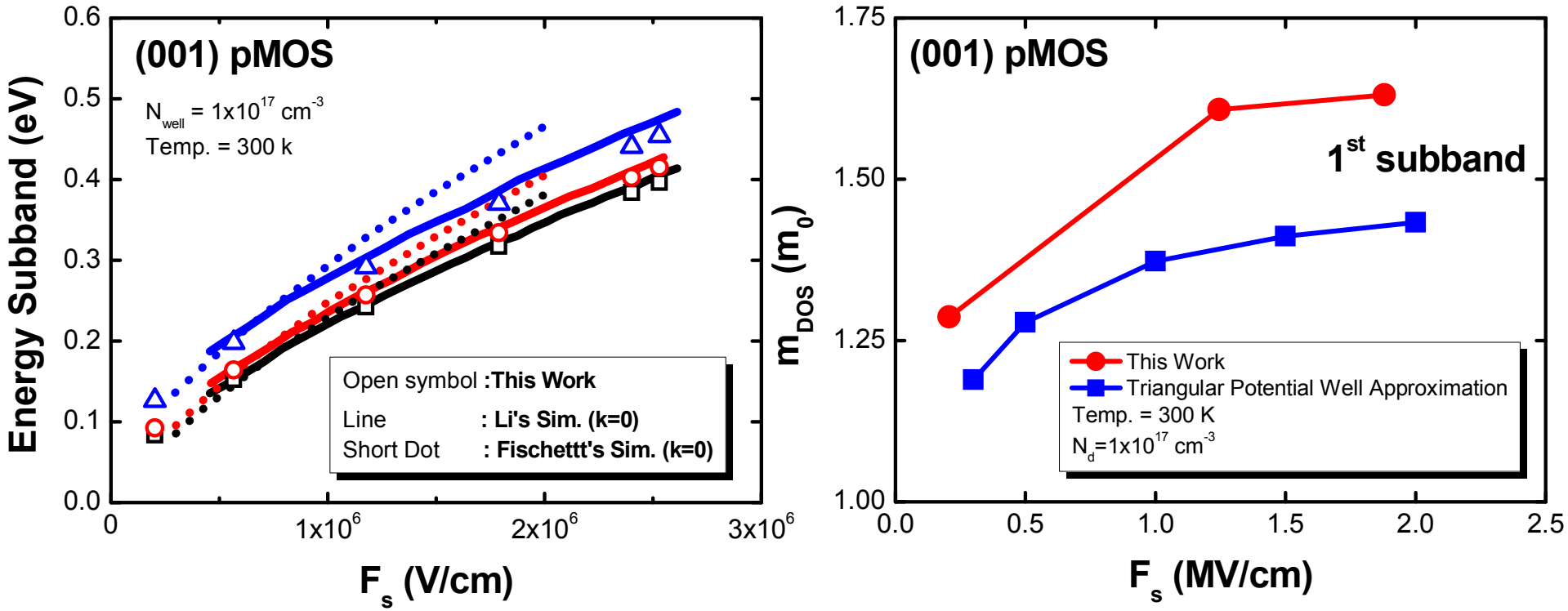

CPU Calculation Time

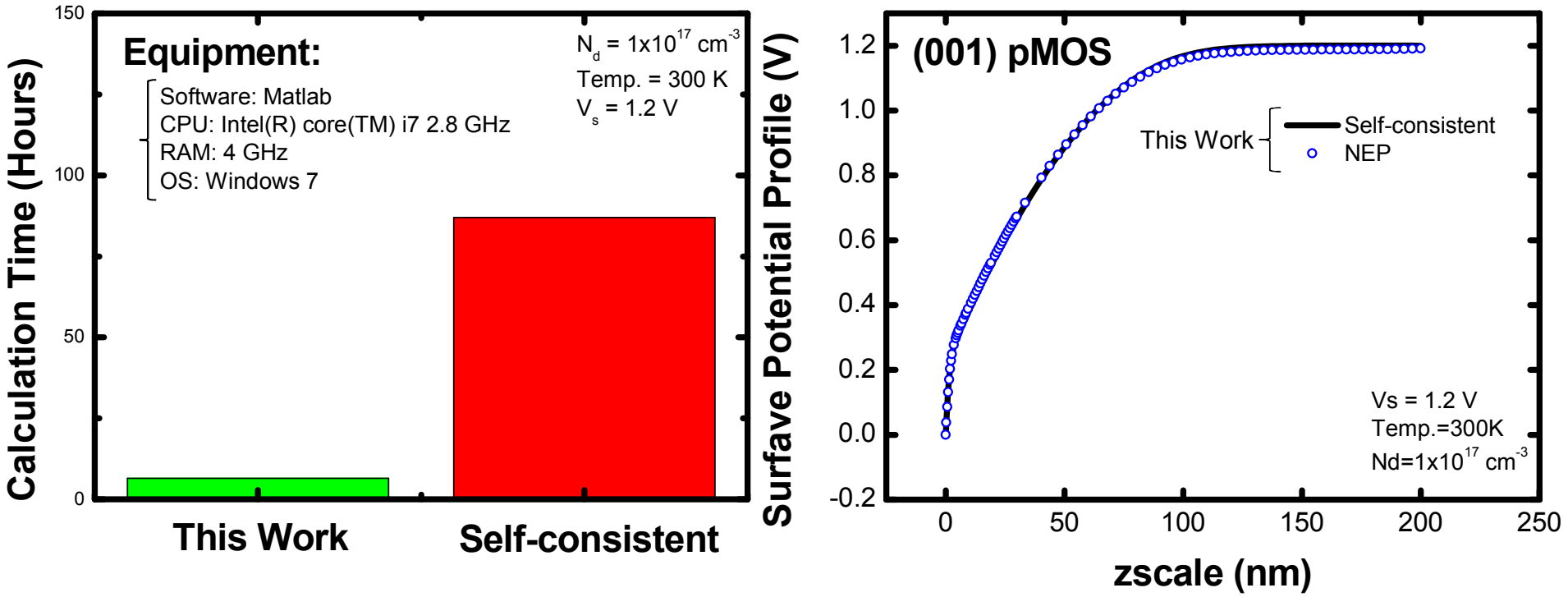

Outline

- Introduction
- Numerical Technique and Physical Theory
- Quantum Simulator NEP for the Two-dimensional Inversion-layers
- Hole Mobility
- **Simulation Results and Discussion**
  - n-MOSFETs
  - p-MOSFETs with Triangular Potential Well Approximation
  - Efficiently Boosted Model in p-MOSFETs
  - Density-of-States and Quantization Effective Mass
  - Mobility
- Conclusion

Density-of-States and Quantization Effective Mass in different temperatures (30, 77, 153, 300 K)

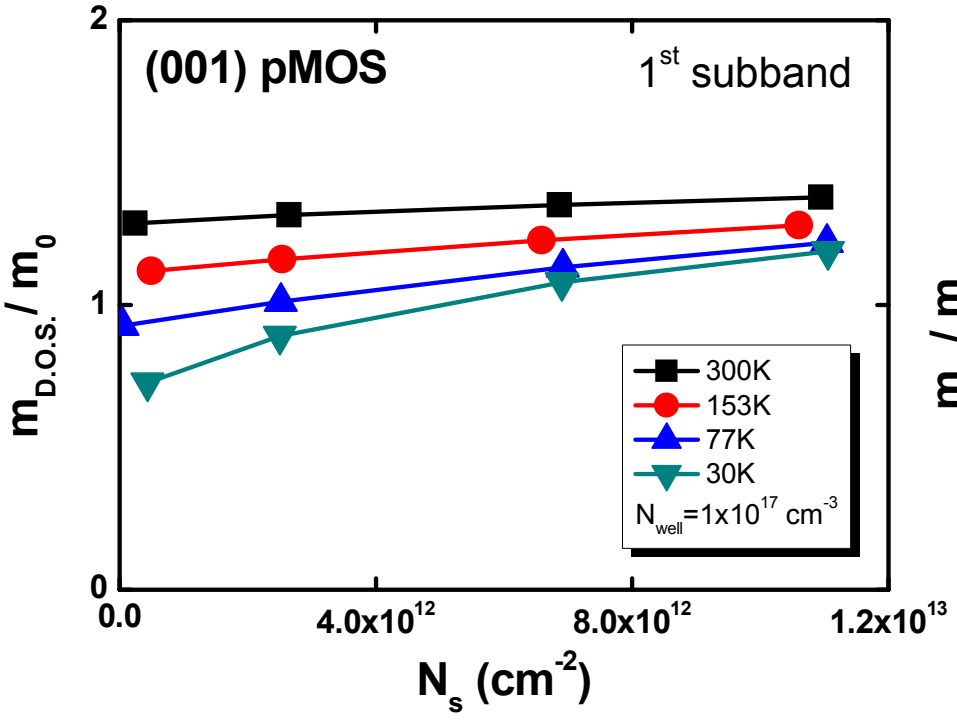

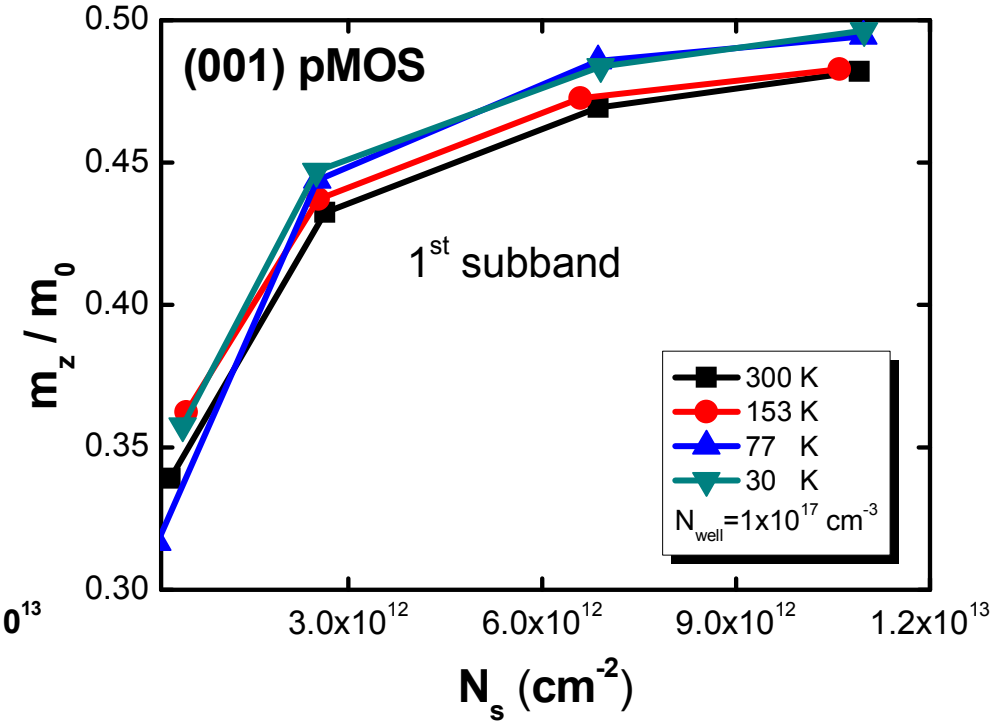

Density-of-States and Quantization Effective Mass
with strained effect (Biaxial tensile, Uniaxial compressive)

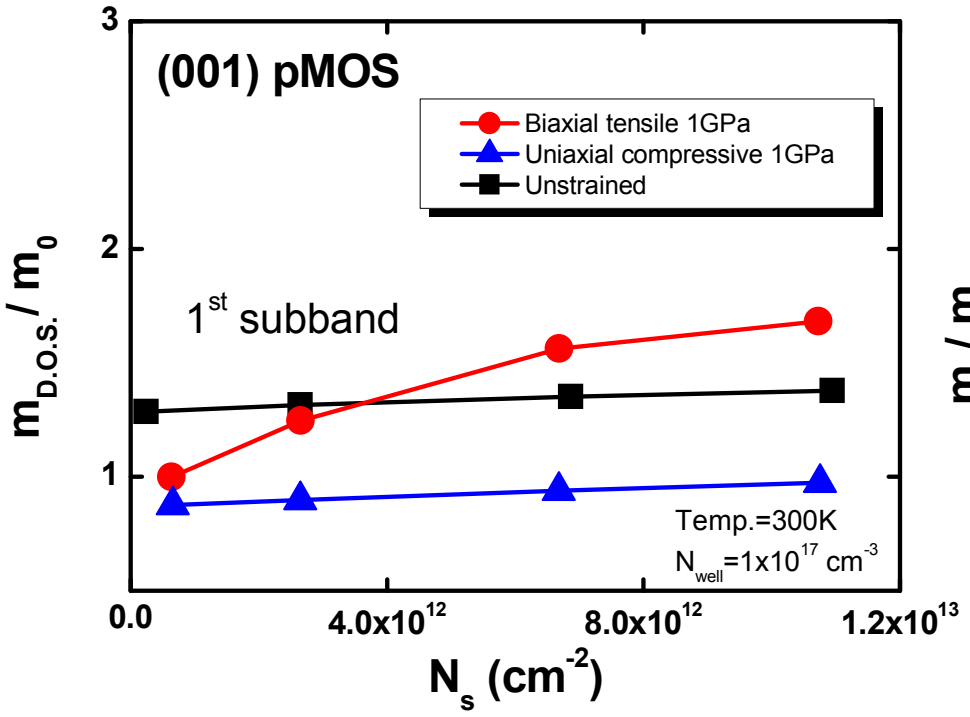

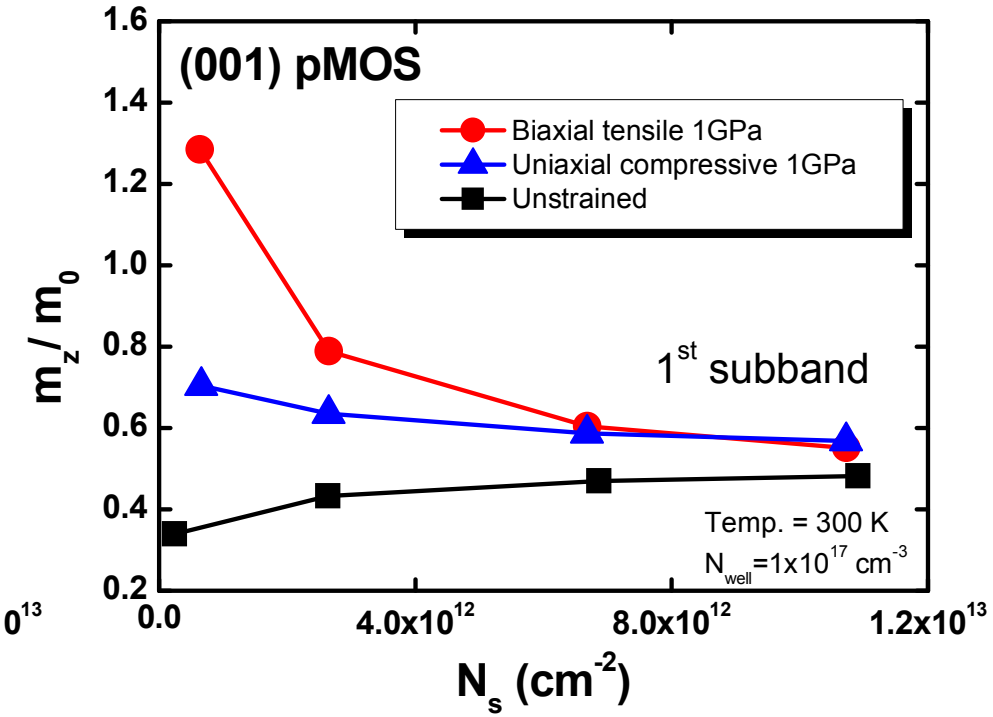

Effective Mass of Density-of-States and Cyclotron

The metal work function for aluminum is 4.26 eV

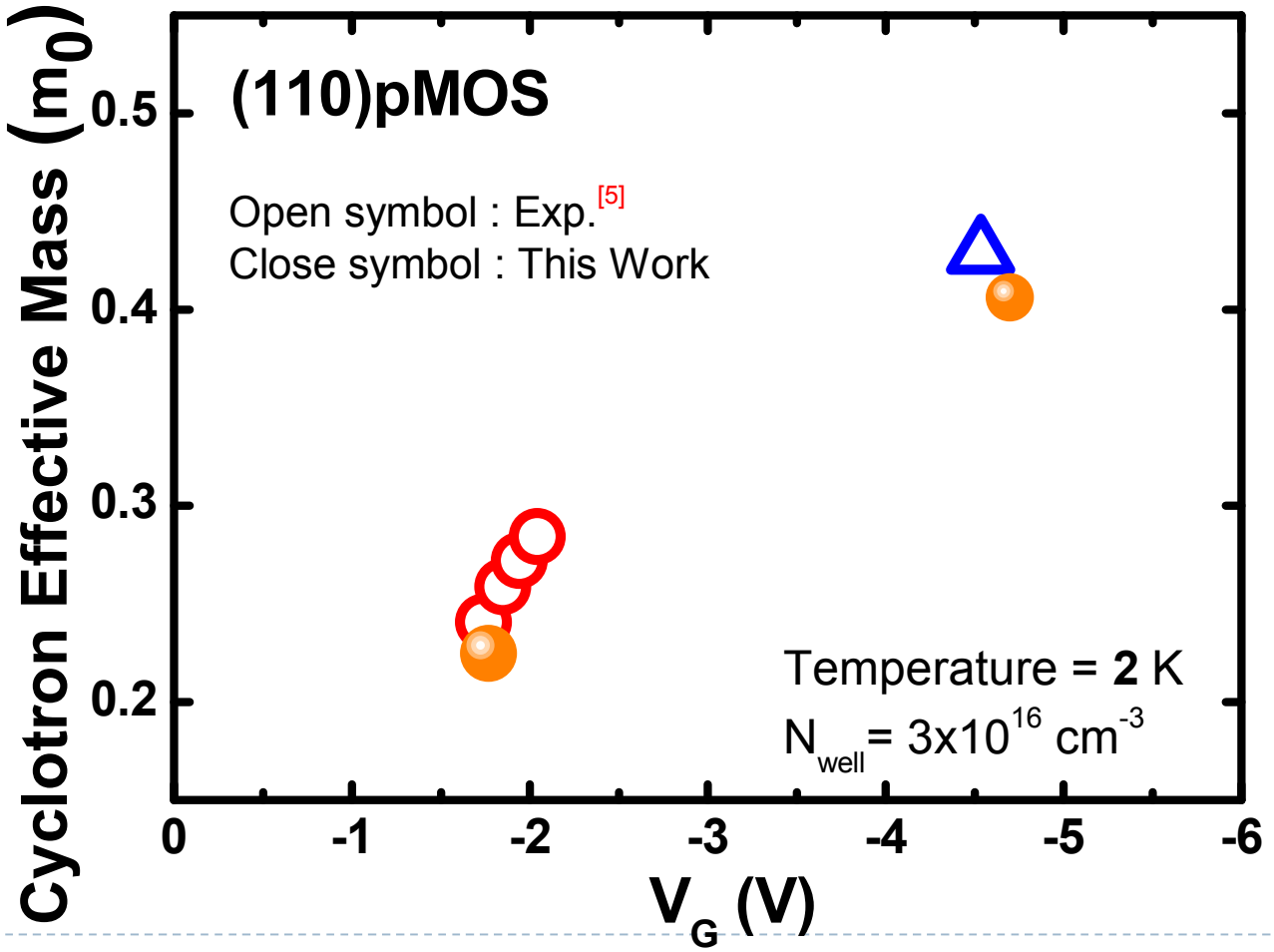

Outline

- Introduction
- Numerical Technique and Physical Theory
- Quantum Simulator NEP for the Two-dimensional Inversion-layers
- Hole Mobility
- **Simulation Results and Discussion**
  - n-MOSFETs
  - p-MOSFETs with Triangular Potential Well Approximation
  - Efficiently Boosted Model in p-MOSFETs
  - Density-of-States and Quantization Effective Mass
  - Mobility
- Conclusion

Phonon and Surface Roughness scattering rate

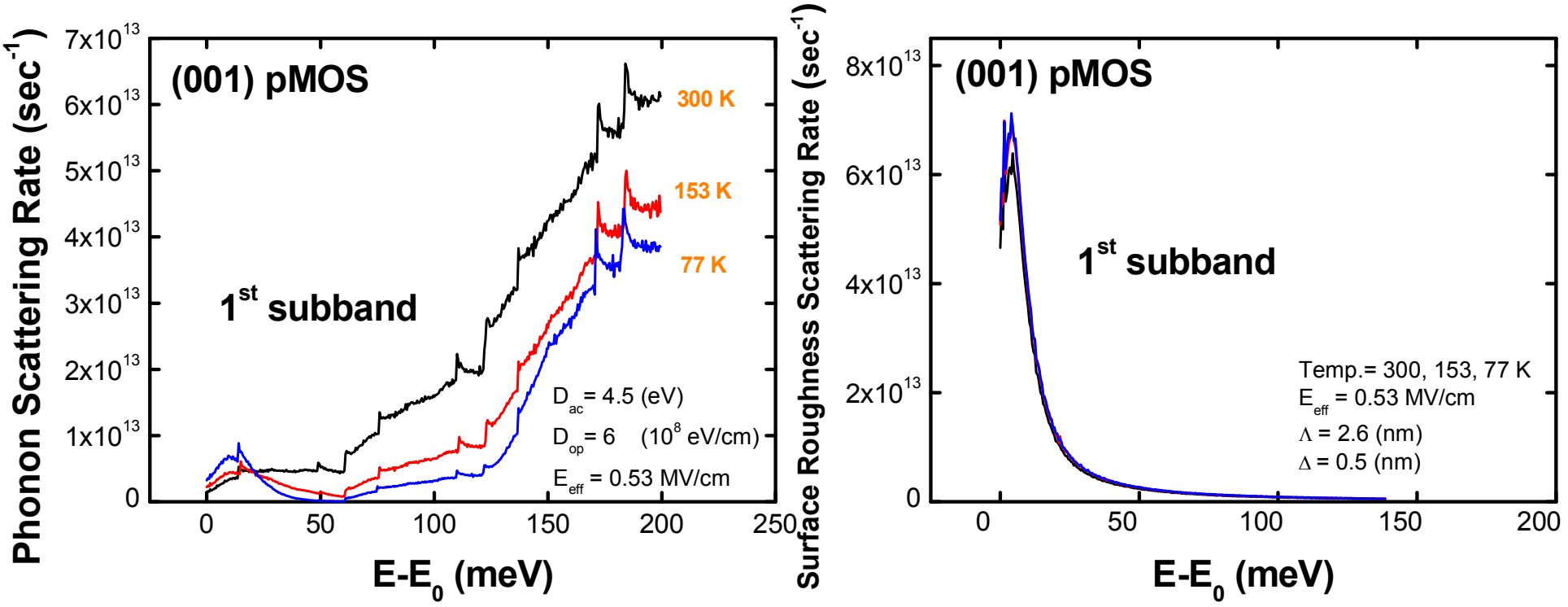

Mobility comparison with Experiments.

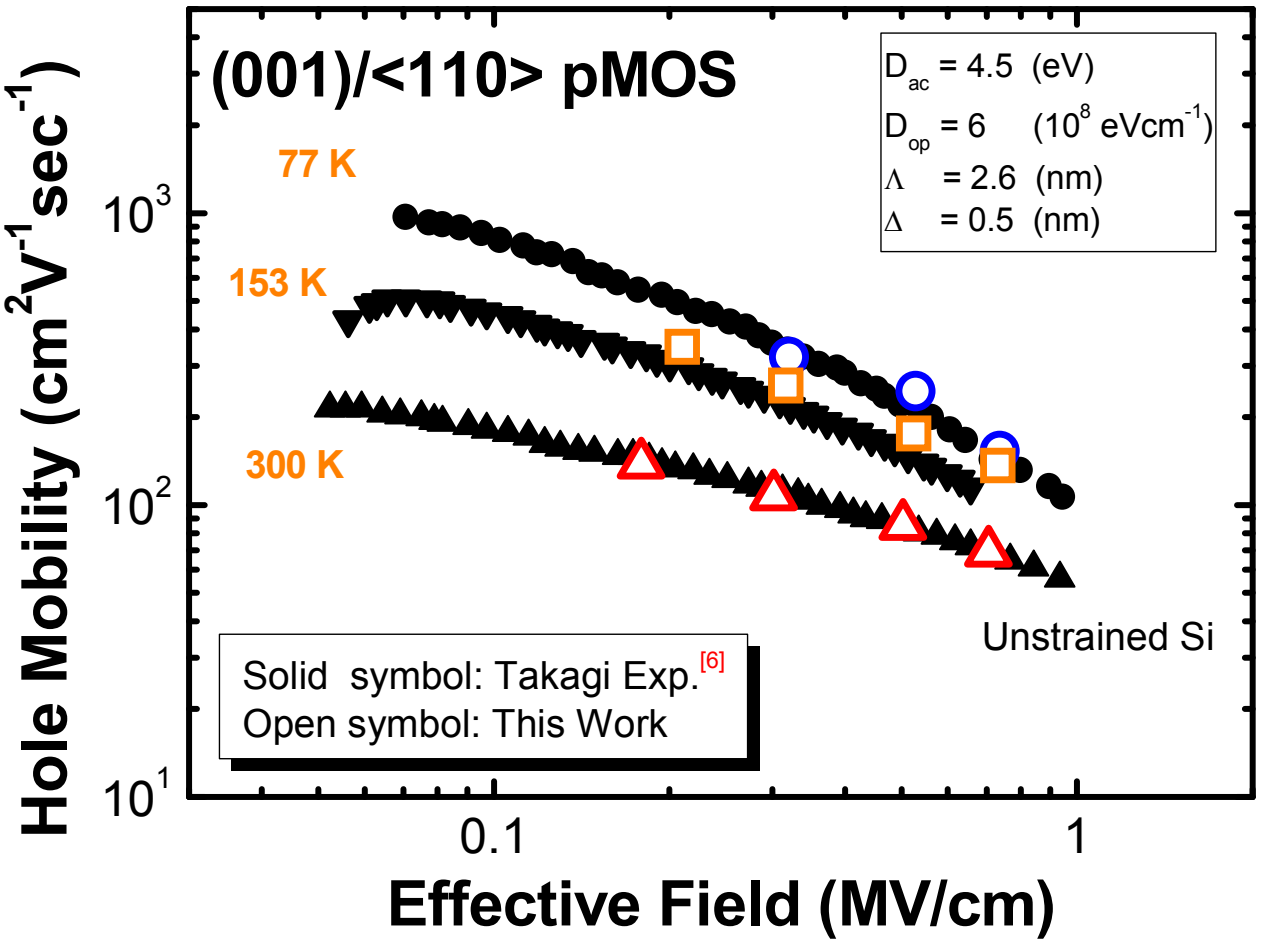

Table I:
Band parameters and Deformation potential

Parameter	This Work	Thompson[2]	Fischetti[4]	Li[7]
γ_1	4.22	4.22		4.285
γ_2	0.39	0.39		0.339
γ_3	1.44	1.44		1.446
a (eV)	2.46	2.46	2.1	
b (eV)	-2.1	-2.1	-2.33	
d (eV)	-4.8	-4.8	-4.75	
Δ (eV)	0.044	0.044		0.044

Table II:
Scattering and Physical parameters

Parameter	This work (001)	Fischetti[3],[4] (001) (011) (111)	Michielis[15] (001)	Oberhuber[20] (001)
Optical energy $\hbar\omega$ (meV)	61.2	61.2	61.2	61.2
Crystal density ρ (g/cm^3)	2.329	2.33		
Sound velocity u_l (m/s)	9040	9000		
Optical phonons D_{op} (10^8 eV/cm)	6	13.24	11.5	7.63
Acoustic phonons D_{ac} (eV)	4.5	7.12	5.6	5
Surface Roughness Λ (nm)	2.6	2.6	2.6	0.2
Surface Roughness Δ (nm)	0.5	0.4	0.55	0.5

Outline

- Introduction
- Numerical Technique and Physical Theory
- Quantum Simulator NEP for the Two-dimensional Inversion-layers
- Hole Mobility
- Simulation Results and Discussion
- **Conclusion**

Conclusion

- We have completed the self-consistent method for solving Schrödinger and Poisson equations to simulate a more realistic environment in n/ p-MOSFETs.
- Efficiently boosted NEP in p-MOSFETs to avoid intolerable calculation time.
- The ionization rate has been taken into account for low temperature condition (~ 2 K).
- The hole mobility parameters can be extracted by the best curve-fitting in the experimental data.

References

[1] D. Vasileska, D. K. Schroder and D.K. Ferry, "Scaled silicon MOSFET's: Part II - Degradation of the total gate capacitance," *IEEE Trans. Electron Devices*, vol. **44**, no.4, pp. 584-587, April 1997.

[2] Y. Sun, S. E. Thompson, and T. Nishida, "Physics of strain effects in semiconductors and metal-oxide-semiconductor field-effect transistors," *J. Appl. Phys.*, vol. **101**, no. 10, p. 104503, May 2007.

[3] M. V. Fischetti, Z. Ren, P. M. Solomon, M. Yang, and K. Rim, "Six-band $k \cdot p$ calculation of the hole mobility in silicon inversion layers: Dependence on surface orientation, strain, and silicon thickness," *J. Appl. Phys.*, vol. **94**, no. 2, pp. 1079-1095, Jul. 2003.

[4] M. V. Fischetti and S. E. Laux, "Band structure, deformation potentials, and carrier mobility in strained Si, Ge, and SiGe alloys," *J. Appl. Phys.*, vol. **80**, no. 4, pp. 2234-2252, Aug. 1996.

[5] Tsunaki Takahashi, Gento Yamahata, Jun Qgi, Tetsuo, Shunri Oda and Ken Uchida, "Direct observation of subband structures in (110) pMOSFETs under High magnetic field: Impact of energy split between bands and effective masses on hole mobility," *IEEE International Electron Devices Meeting (IEDM) International*, pp. 477-480, Dec. 2009 (Baltimore, MD).

[6] Shin-ichi Takagi, Akira Toriumi, Masao Iwase and Hiroyuki Tango, "On the universality of inversion layer mobility in Si MOSFET's: Part I—Effects of substrate impurity concentration," *IEEE Trans. Electron Devices*, vol. **41**, no. 12, pp. 2357-2362, Dec. 1994.

[7] Tony Low, M. F. Li, Y. C. Yeo, W. J. Fan, S. T. Ng and D. L. Kwong, "Valence band structure of ultrathin silicon and germanium channels in metal-oxide-semiconductor field-effect transistors," *J. Appl. Phys.*, vol. **98**, no. 2, p. 024504, July. 2005.

[8] R. Winkler and A. I. Nesvizhskii, "Anisotropic hole subband states and interband optical absorption in [*mmn*]-oriented quantum wells," *Phys. Rev. B*, vol. **53**, no. 15, pp. 9984-9992, April 1996.

[9] Frank Stern, "Self-consistent results for n-type Si inversion layers," *Phys. Rev. B*, vol. **5**, no. 12, pp. 4891-4899, June 1972.

[10] A. M. Cruz Serra and H. Abreu Santos, "A one-dimensional, self-consistent numerical solution of Schrődinger and Poisson equations," *J. Appl. Phys.*, vol. **70**, no. 5, pp. 2734-2738, Sep. 1991.

[11] Sze, *Physics of Semiconductor Devices*, John Wiley & Sons Inc., p. 22.

[12] Shinya Yamakawa, Hiroaki Ueno, Kenji Taniguchi and Chihiro Hamaguchi, "Study of interface roughness dependence of electron mobility in Si inversion layers using the Monte Carlo method," *J. Appl. Phys.*, vol. **79**, no. 2, pp. 911-916, Jan. 1996.

[13] S. Takagi, J. L. Hoyt, J. J. Welser, and J. F. Gibbons, "Comparative study of phonon-limited mobility of two-dimensional electrons in strained and unstrained Si metal-oxide-semiconductor field-effect transistors," *J. Appl. Phys.*, vol. **80**, no. 3, p. 1567, Aug. 1996.

[14] Tony Low, Yong-Tian Hou and Ming-Fu Li, "Improved one-band self-consistent effective mass methods for hole quantization in p-MOSFET," *IEEE Trans. Electron Devices*, vol. **50**, no.5, pp. 1284-1289, May 2003.

[15] Marco De Michielis, David Esseni, Y. L. Tsang, Pierpaolo Palestri, Luca Selmi, Anthony G. O'Neill and Sanatan Chattopadhyay, "A semianalytical description of the hole band structure in inversion layers for the physically based modeling of pMOS transistors," *IEEE Trans. Electron Devices*, vol. **54**, no.9, pp. 2164-2173, Sep. 2007.

[16] M. Uchida, Y. Kamakura, and K. Taniguchi, "Performance enhancement of pMOSFETs depending on strain, channel direction, and material," in *Proc. SISPAD*, 2005, pp. 315-318.

[17] S. E. Thompson, G. Sun, Y. S. Choi, and T. Nishida, "Uniaxial-process-induced strained-Si: Extending the CMOS roadmap," *IEEE Trans. Electron Devices*, vol. **53**, no. 5, pp. 1010-1020, May 2006.

[18] E. X. Wang, P. Matagne, L. Shifren, B. Obradovic, R. Kotlyar, S. Cea, M. Stettler, and M. D. Giles, "Physics of hole transport in strained silicon MOSFET inversion layers," *IEEE Trans. Electron Devices*, vol. **53**, no. 8, pp. 1840-1851, Aug. 2006.

[19] Y. Sun, S. E. Thompson, and T. Nishida, "Physics of strain effects in semiconductors and metal-oxide-semiconductor field-effect transistors," *J. Appl. Phys.*, vol. **101**, no. 10, p. 104503, May 2007.

[20] R. Oberhuber, G. Zandler, and P. Vogl, "Subband structure and mobility of two-dimensional holes in strained Si/SiGe MOSFETs," *Phys. Rev. B, Condens. Matter*, vol. **58**, no. 15, pp. 9941-9948, Oct. 1998.

[21] C. Y. Hsu, C. C. Lee, Y. T. Lin, C. Y. Hsieh, and M. J. Chen, "Enhanced hole gate direct tunneling current in process-induced uniaxial compressive stress p-MOSFETs," *IEEE Trans. Electron Devices*, vol. **56**, no. 8, pp. 1667-1673, Aug. 2009.

[22] Kuo-Nan Yang, Huan-Tsung Huang, Ming-Chin Chang, Che-Min Chu, Yuh-Shu Chen, Ming-Jer Chen, Yeou-Ming Lin, Mo-Chiun Yu, Simon M. Jang, Douglas C.H. Yu and M. S. Liang, "A physical model for hole direct tunneling current in p^+ poly-gate pMOSFETs with ultrathin gate oxides," *IEEE Trans. Electron Devices*, vol. **47**, no. 11, pp. 2161-2166, Nov. 2009.

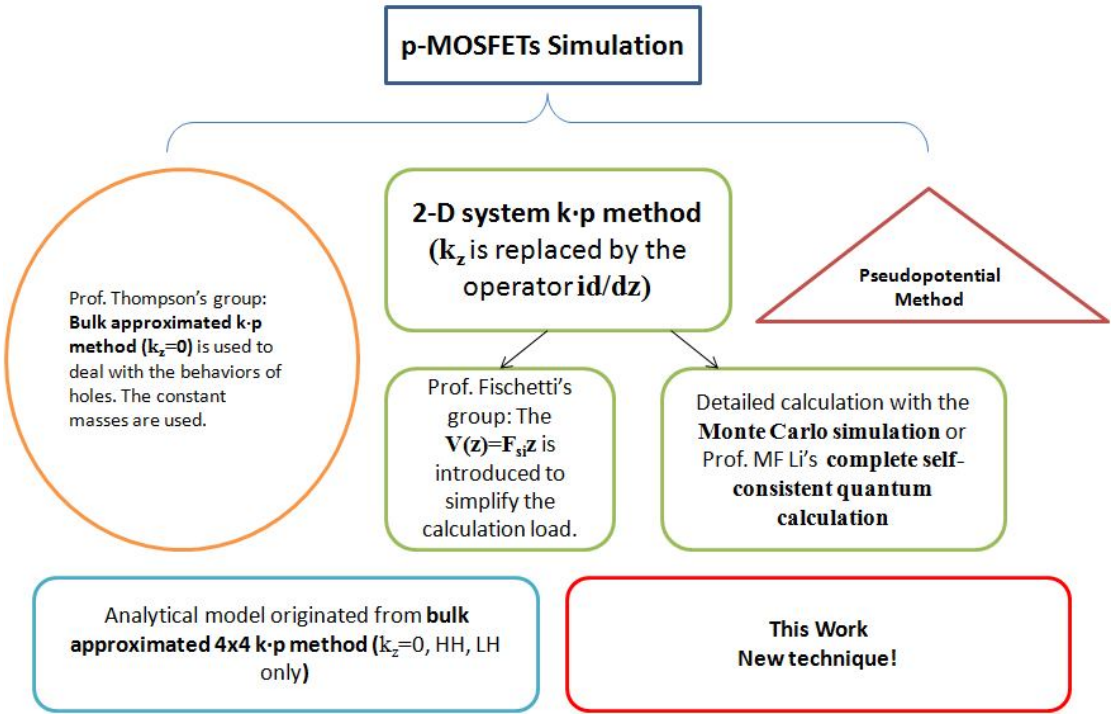

Figure 1.1. Categorizing the researches to date for exploring the two dimensional hole gas behaviors.

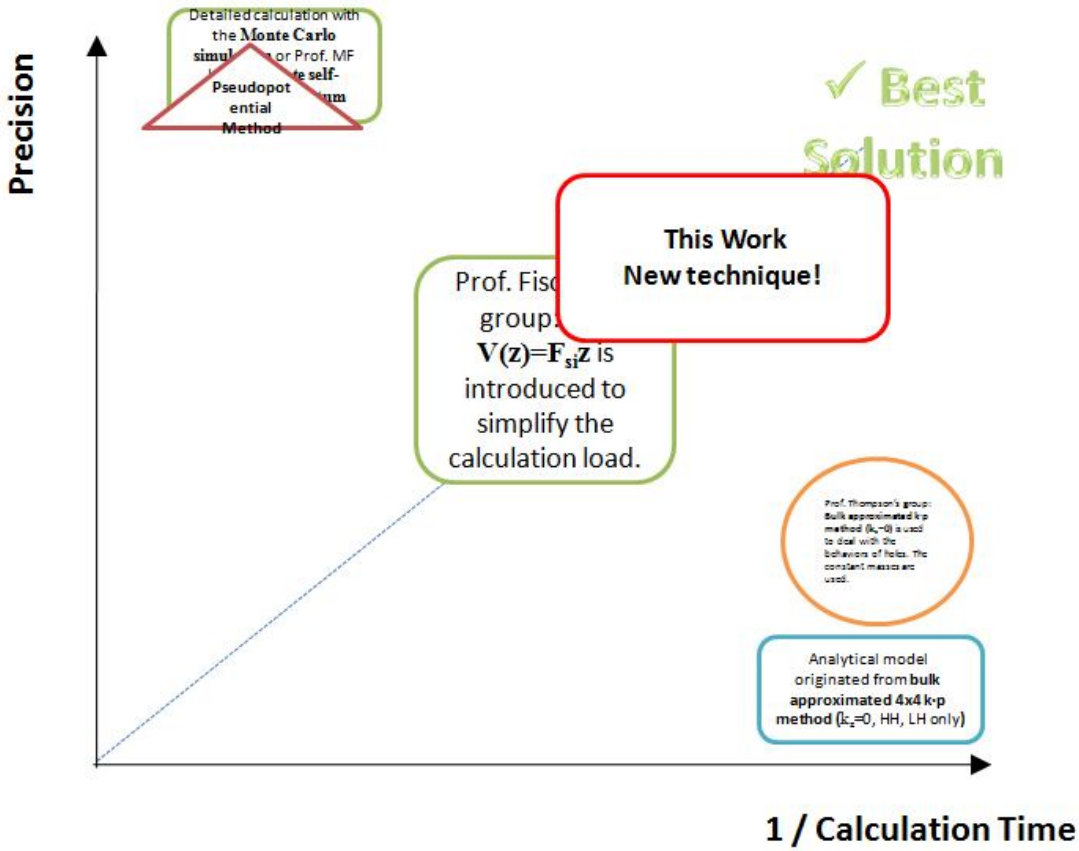

Figure 1.2. Efficiency and calculation time comparison.

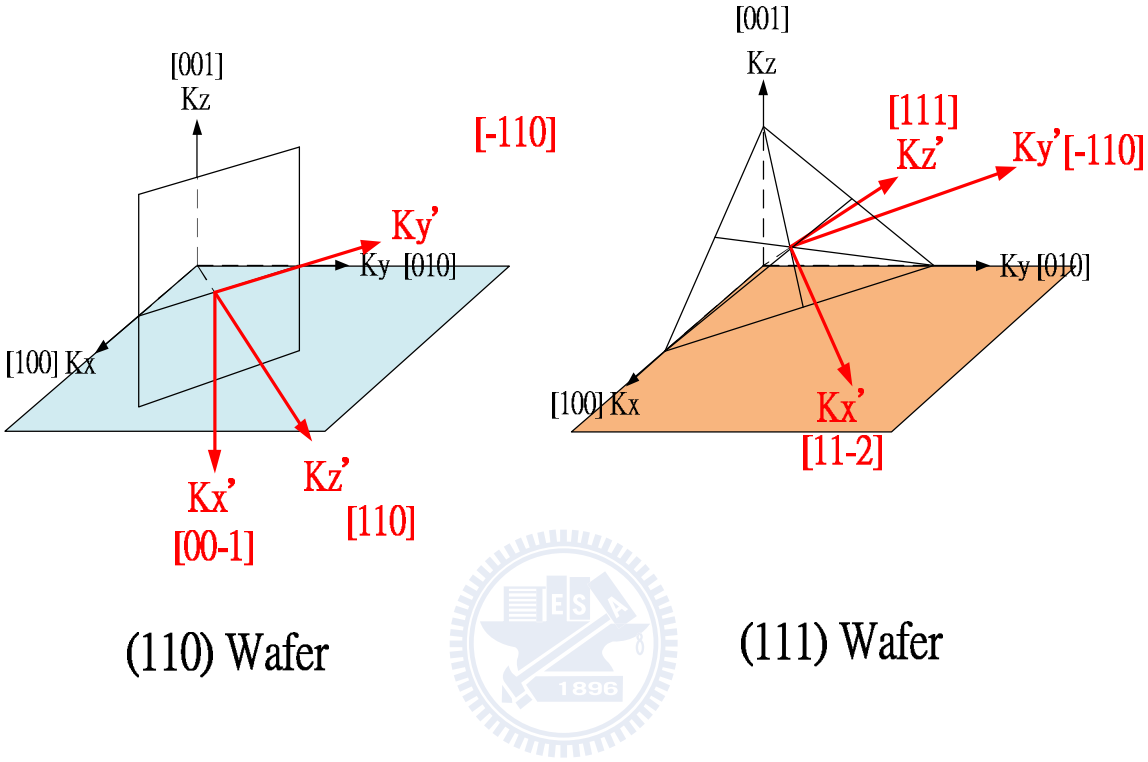

Figure 2.2.2.1. Symmetry-adapted coordinate systems that are used in this work.

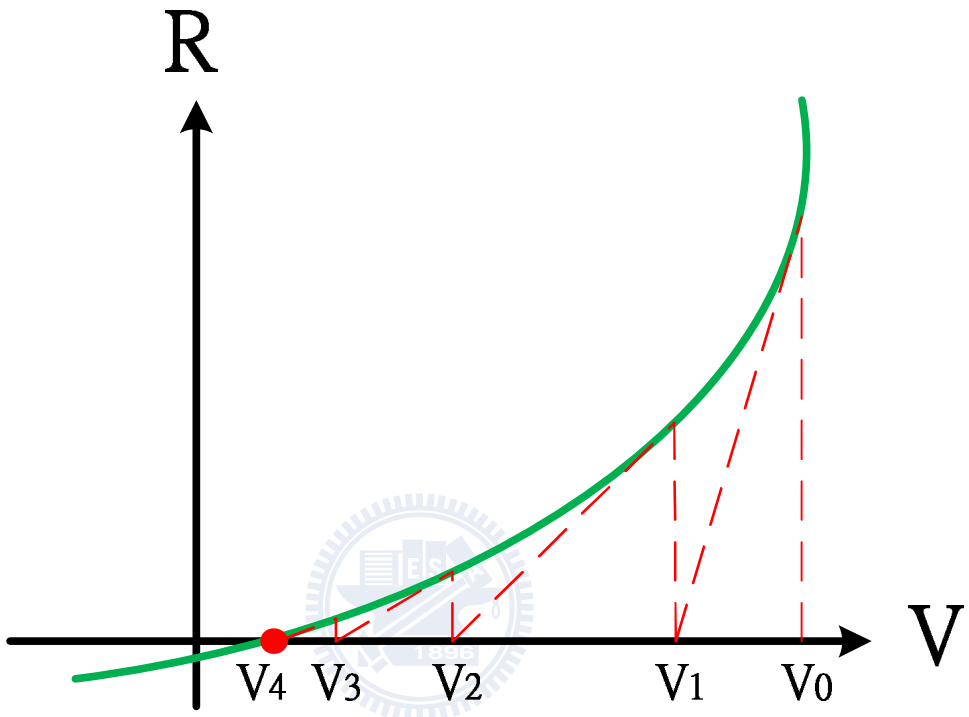

Figure 2.2.3.1. The concept of performing the Newton-Raphson method.

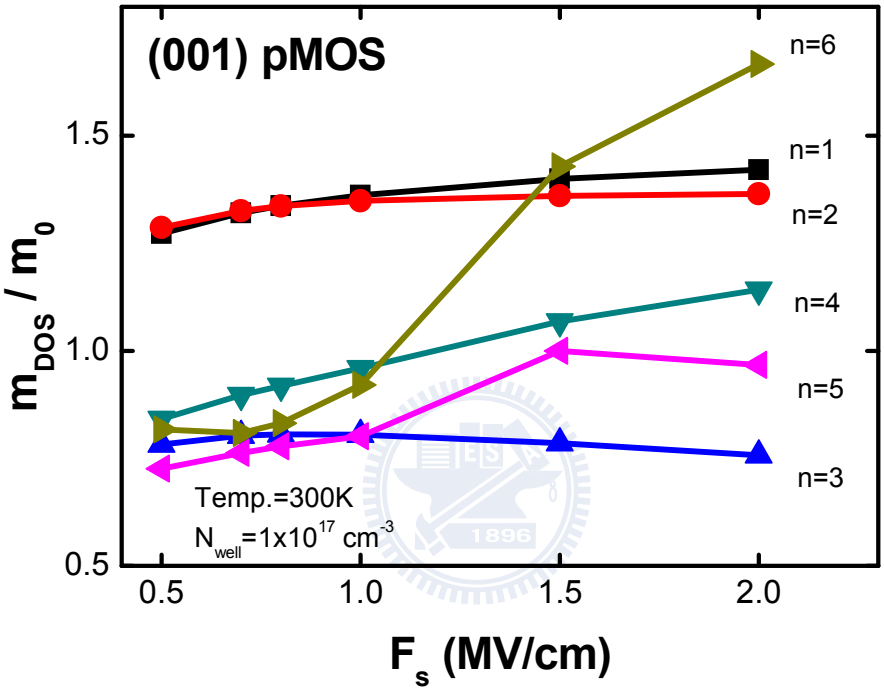

Figure 2.4.2.1. Density of states effective mass of each subband by triangular potential approximation.

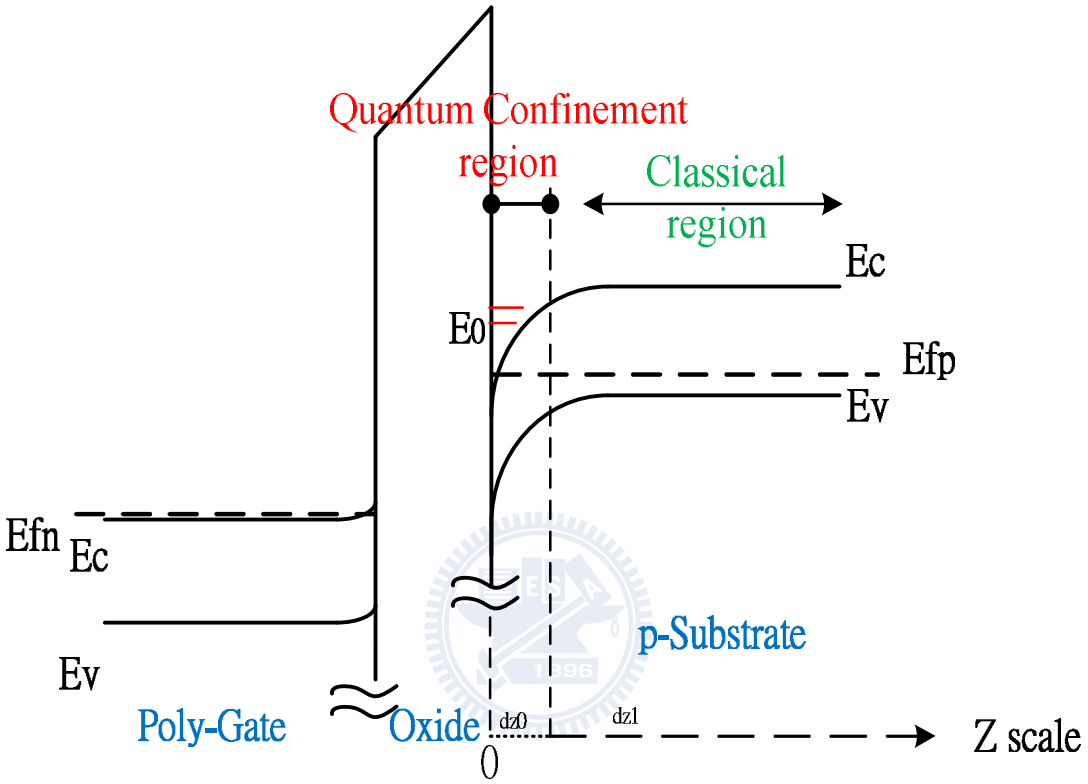

Figure 3.1.1. The schematic band diagram in a poly gate/SiO_2/p-substrate system.

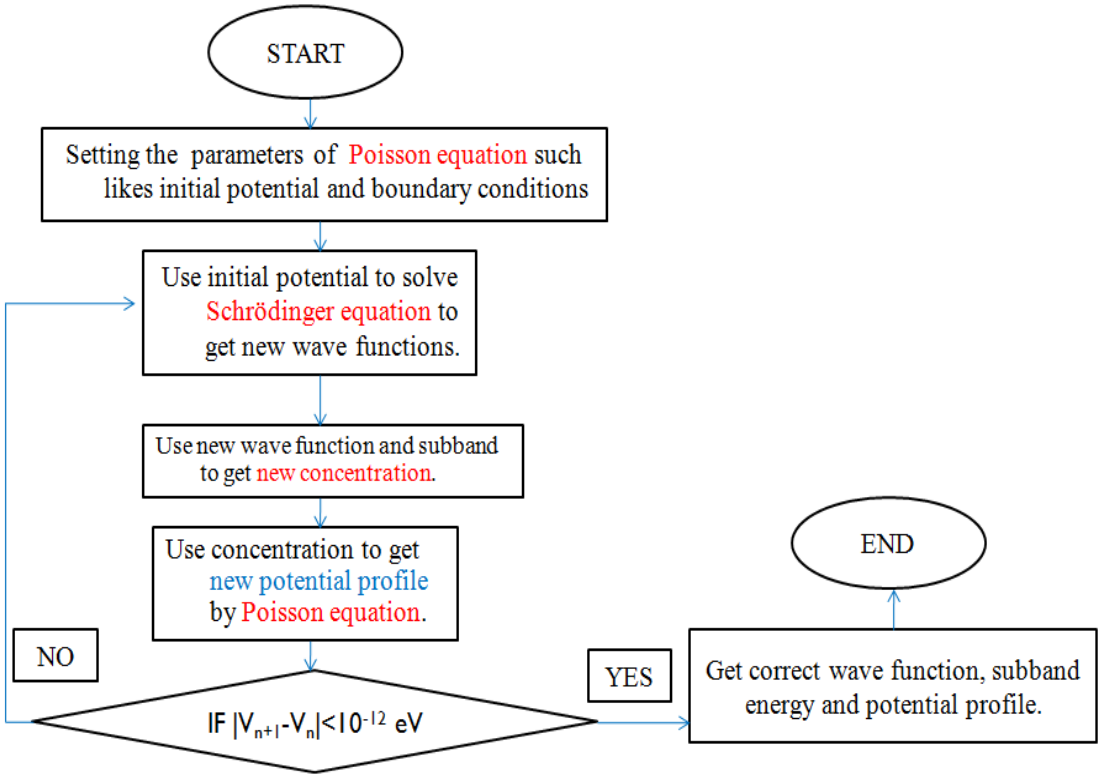

Figure 3.1.2. The flow chart of the self-consistent procedure.

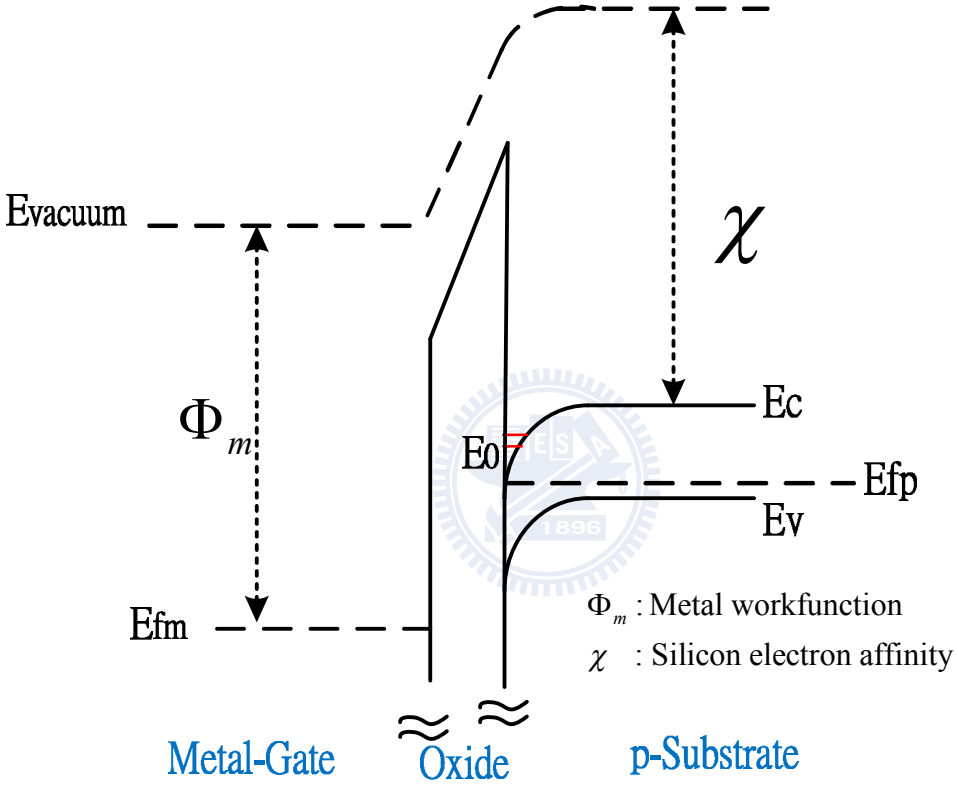

Figure 3.1.3. The energy band diagram in a metal/SiO_2/p-Si system.

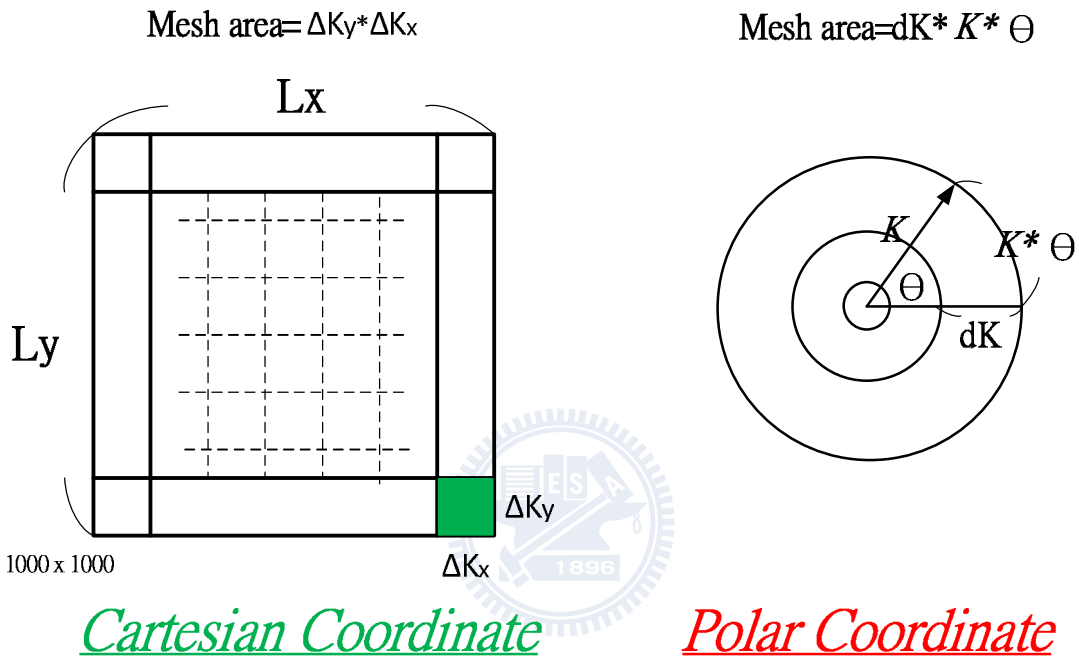

Figure 3.2.1. Meshes for the polar coordinate and Cartesian coordinate.

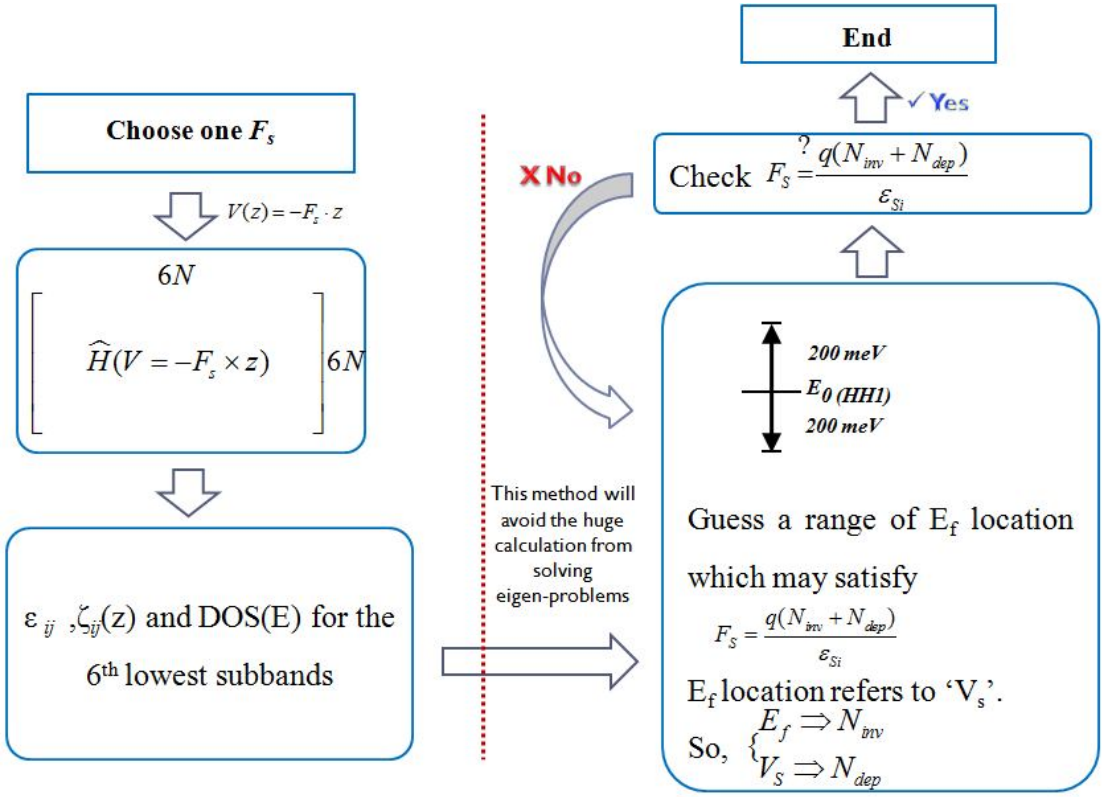

Figure 3.2.2. The flow chart for this work by triangular potential approximation.

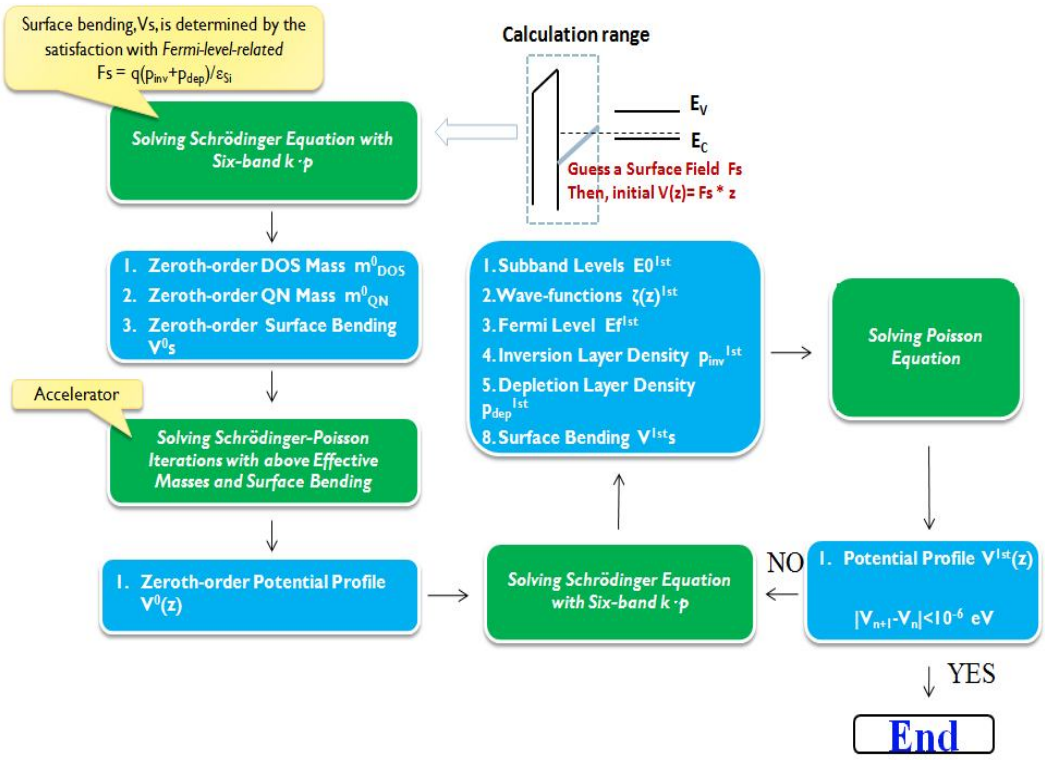

Figure 3.3.1 The flow chart of new technique. (***The First-order Modification***)

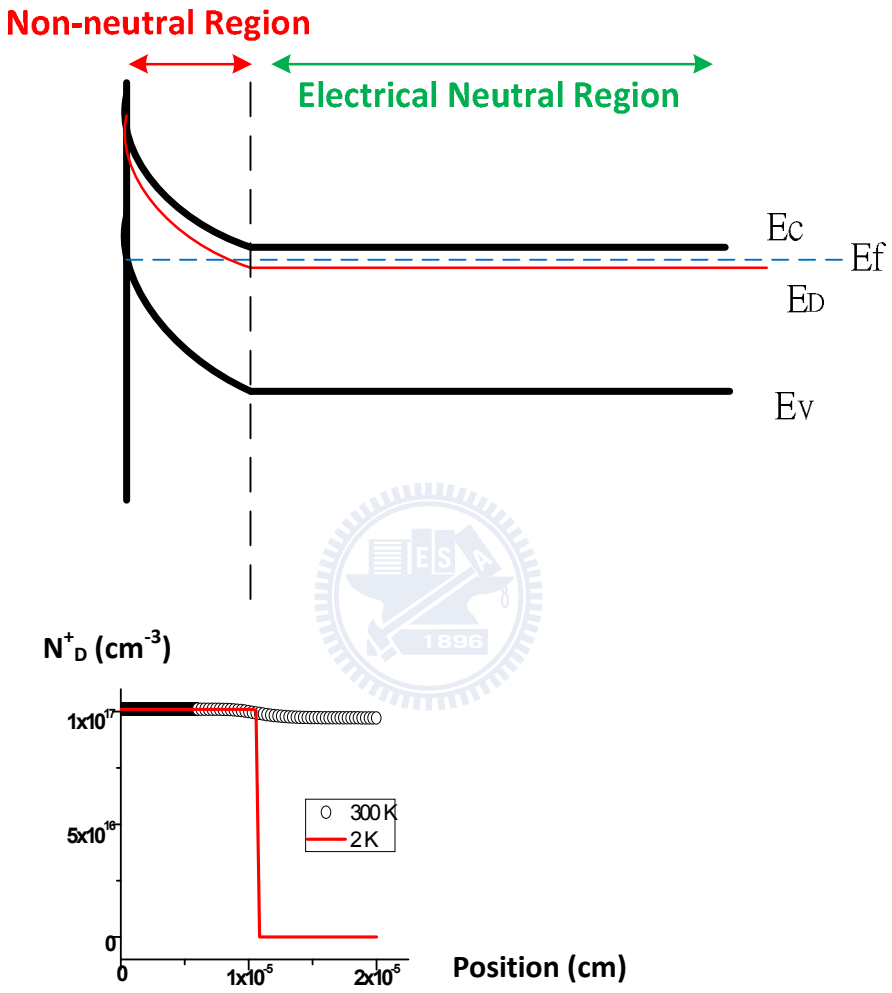

Figure 3.4.1 Impurity ionization rate and band diagram at extremely low temperature about 2 K.

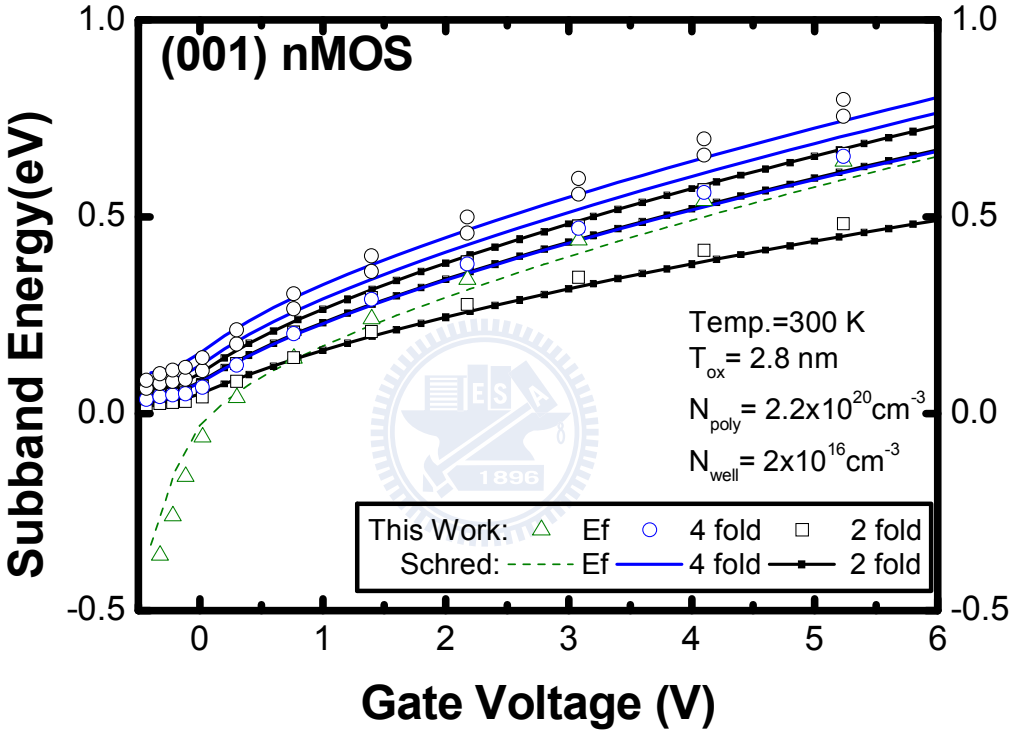

Figure 5.1. Subband level versus gate voltage in n-MOSFETs.

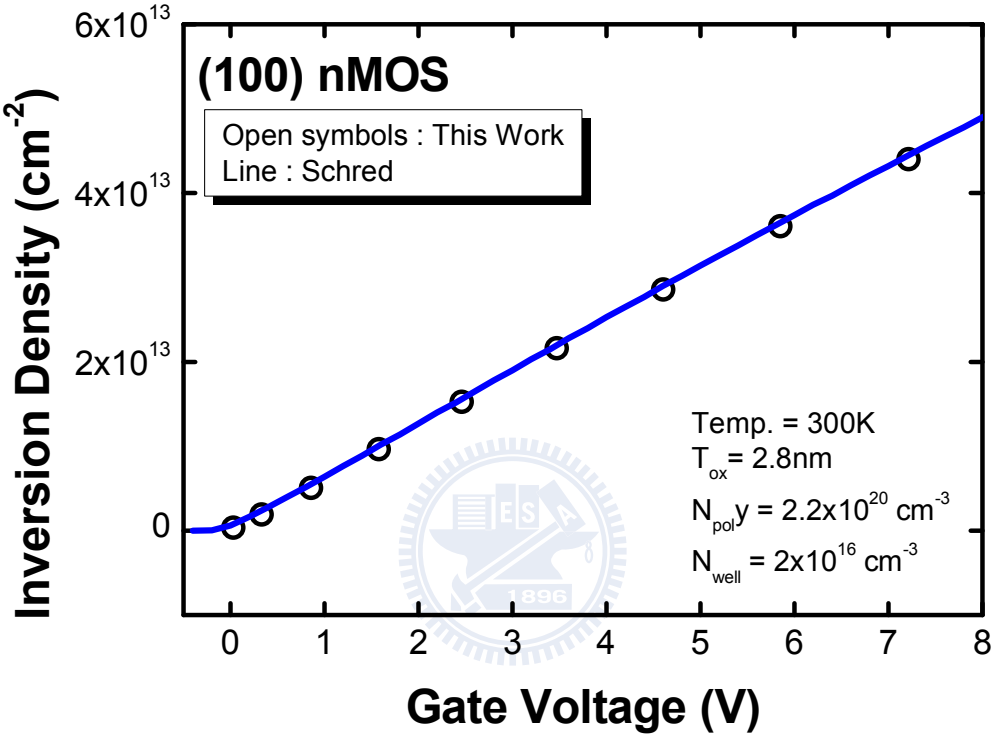

Figure 5.2. Inversion density versus gate voltage in n-MOSFETs.

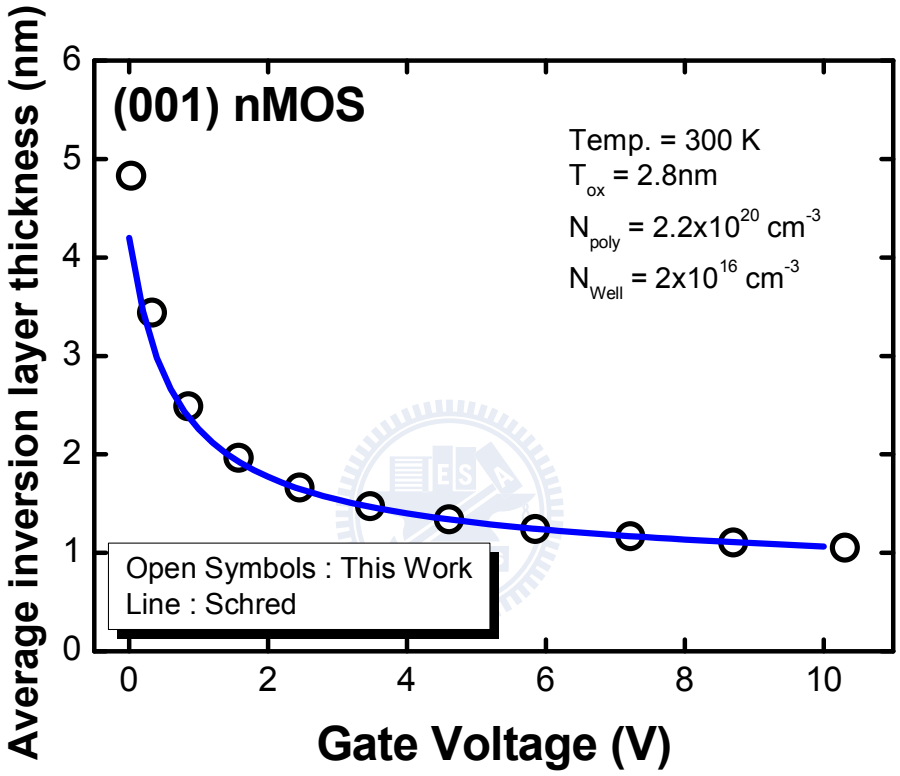

Figure 5.3. Average inversion layer thickness versus gate voltage in n-MOSFETs.

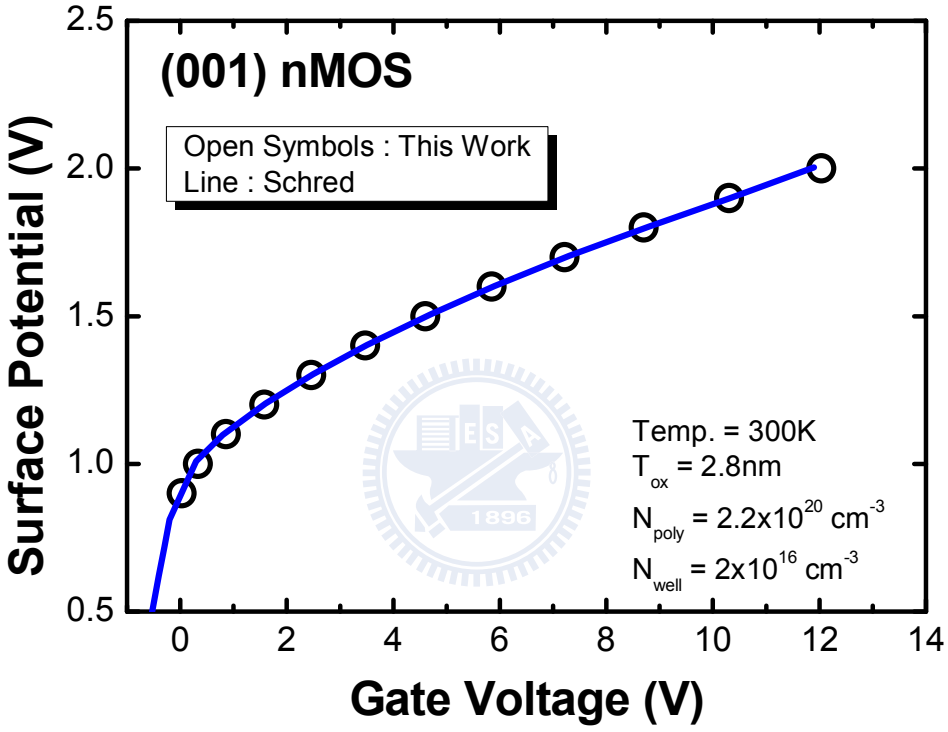

Figure 5.4. Surface potential versus gate voltage in nMOSFET.

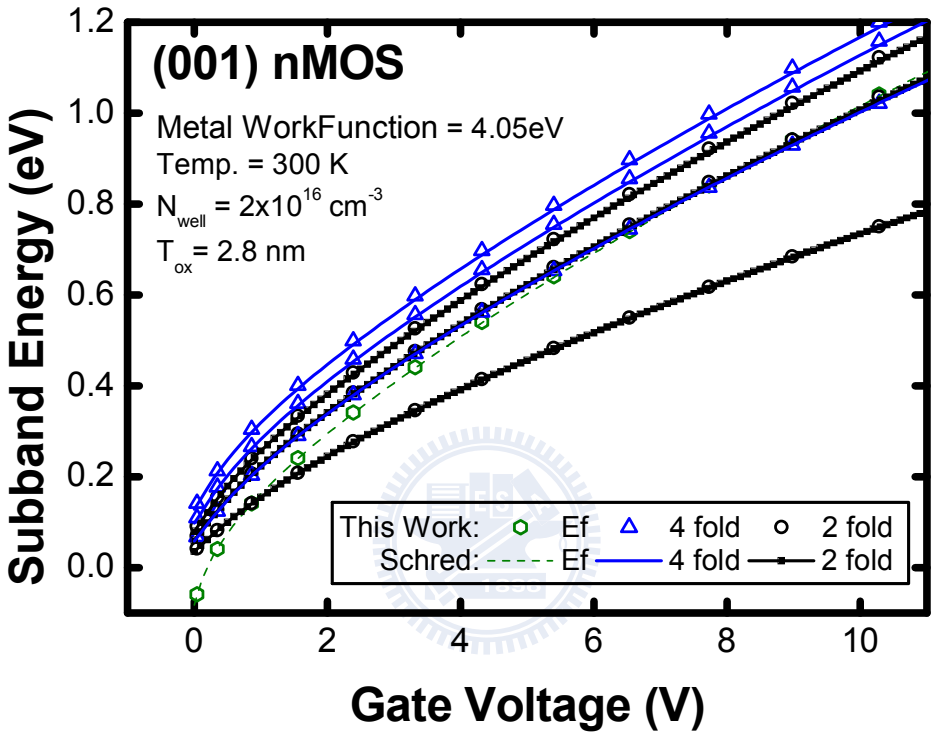

Figure 5.5. Subband energy versus gate voltage in metal gate n-MOSFETs.

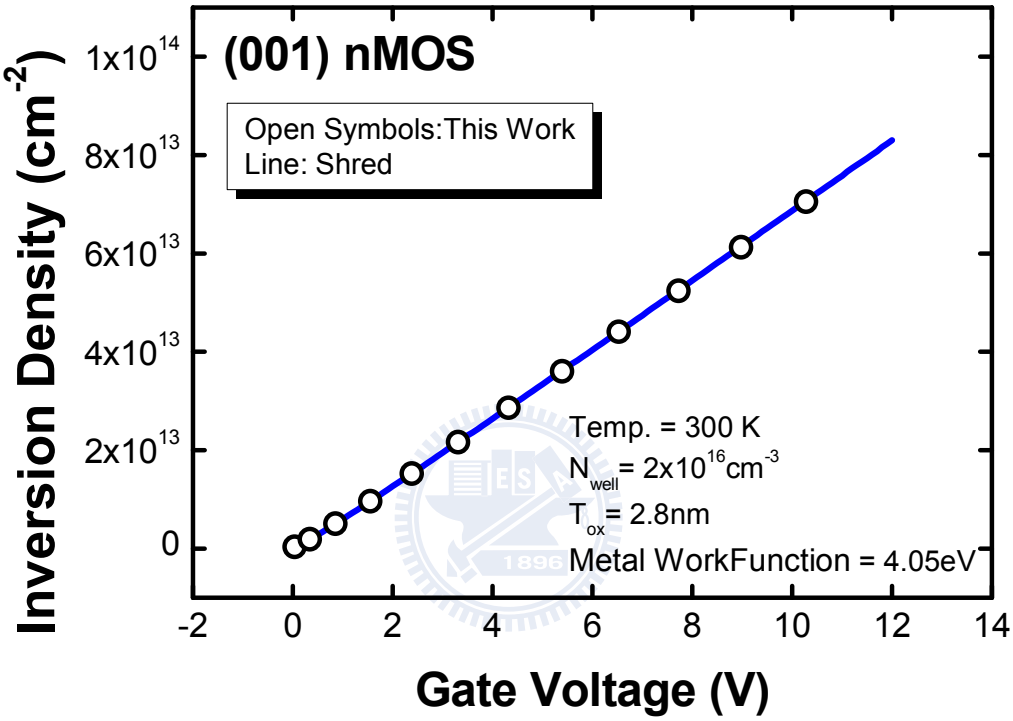

Figure 5.6. Inversion density versus gate voltage in metal gate n-MOSFETs.

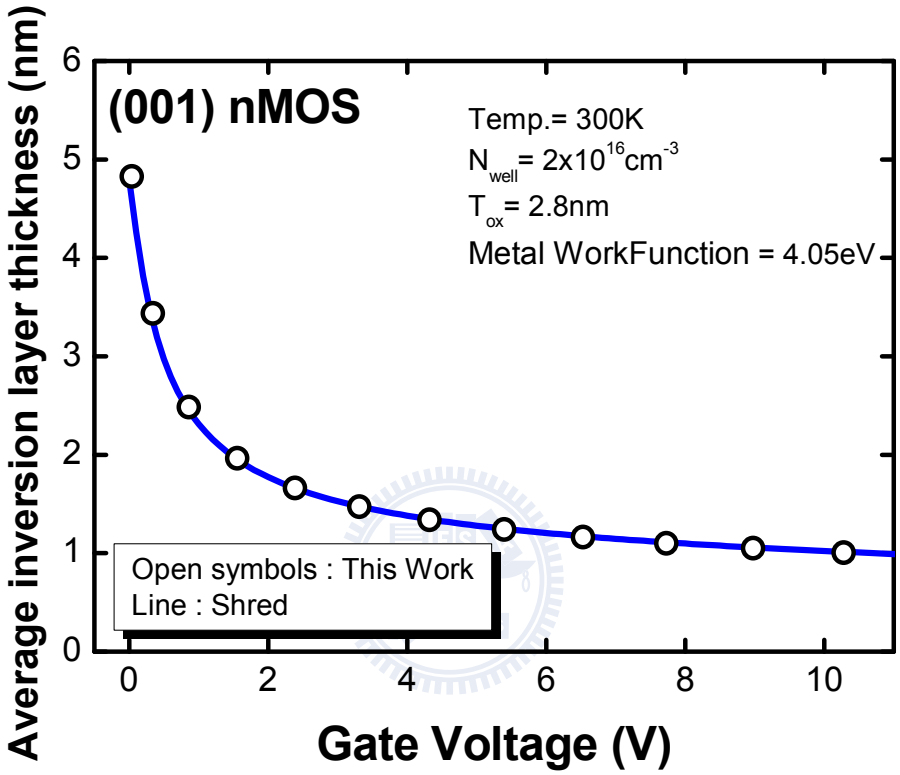

Figure 5.7. Average inversion layer thickness versus gate voltage in metal gate n-MOSFETs.

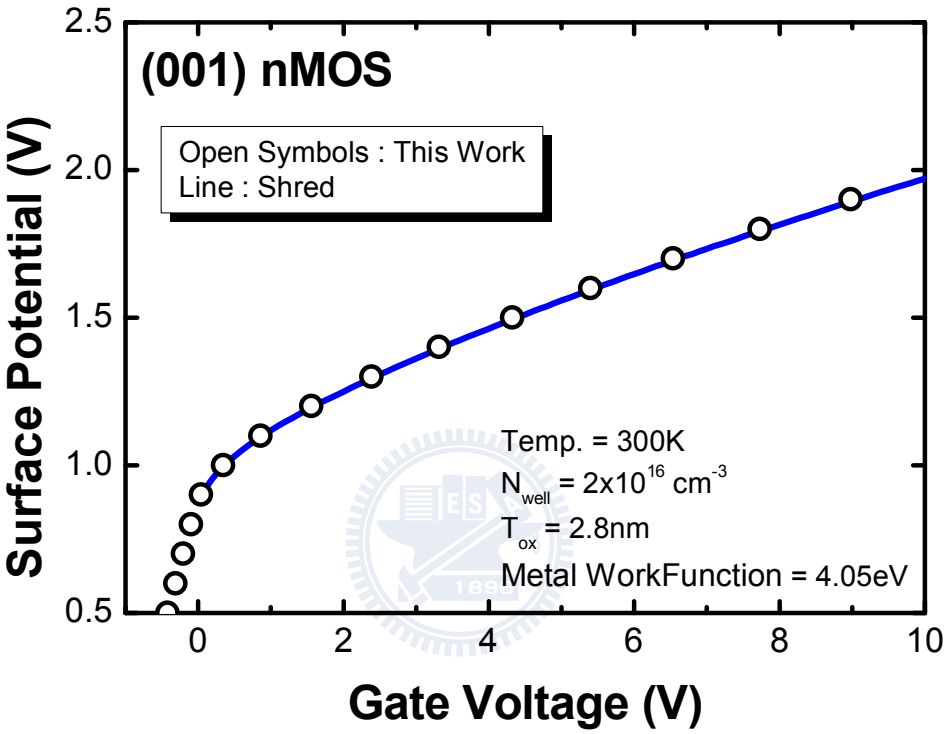

Figure 5.8. Surface potential versus gate voltage in metal gate nMOSFET.

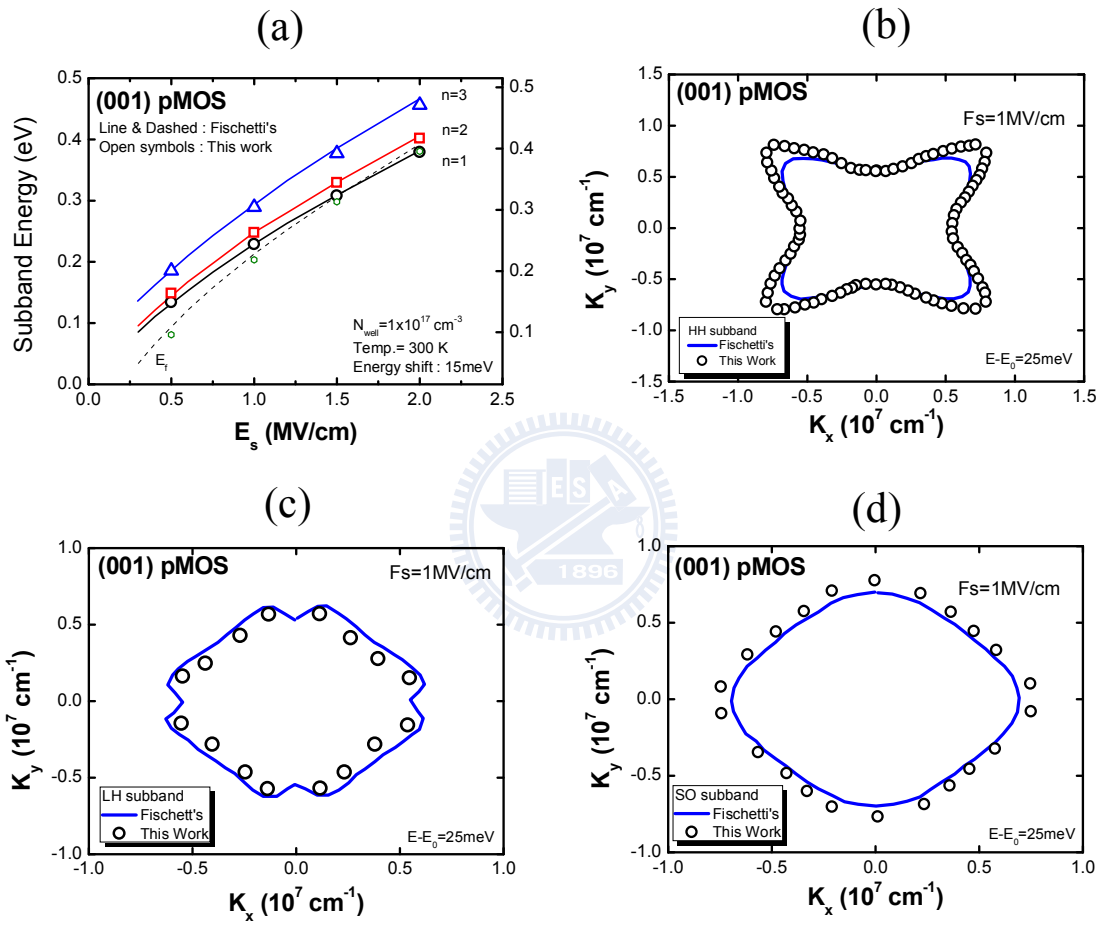

Figure 5.9. Subband energy (a) and equienergy lines (b)-(d) in the lowest–lying HH, LH and SO subbands for the (001) surface compared with Fischetti's [3]. The doping concentration is 1×10^{17} cm^{-3} and temperature is 300 K. It is noticd that our subband energy is higher than Fischetti's about 15meV.

(a)

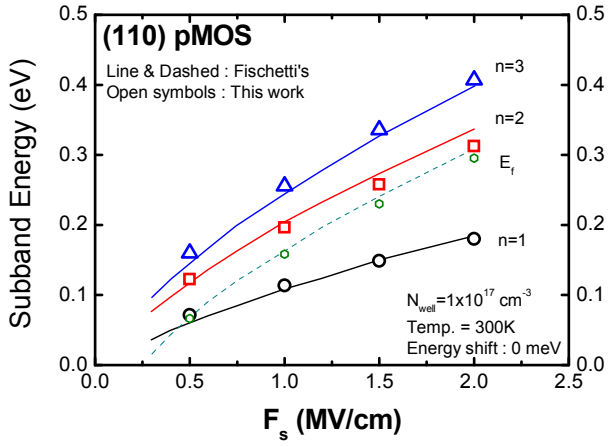

(b)

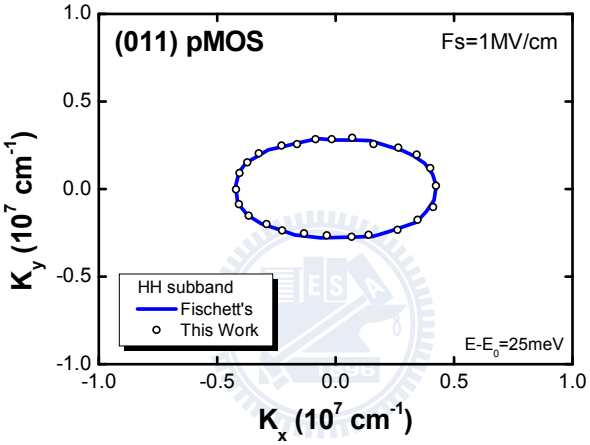

(c)

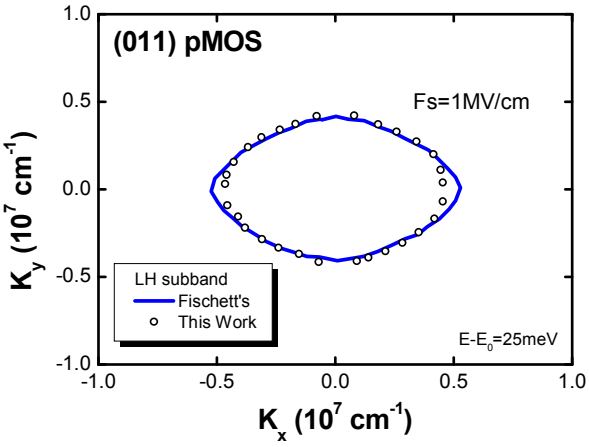

Figure 5.10. Subband energy (a) and equienergy lines (b) and (c) in the lowest–lying HH and LH subbands for the (011) surface compared with Fischetti's [3]. The doping concentration is 1×10^{17} cm^{-3} and temperature is 300 K.

(a)

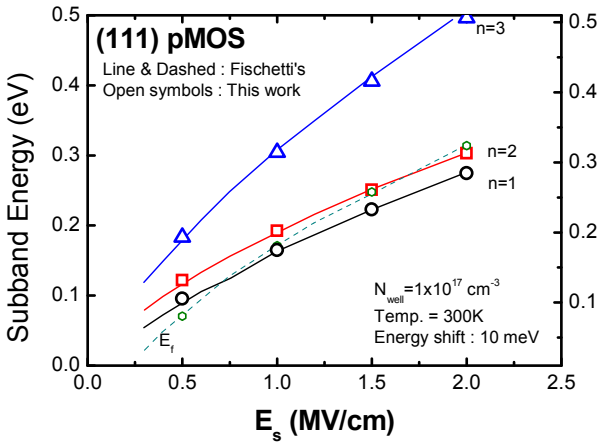

(b)

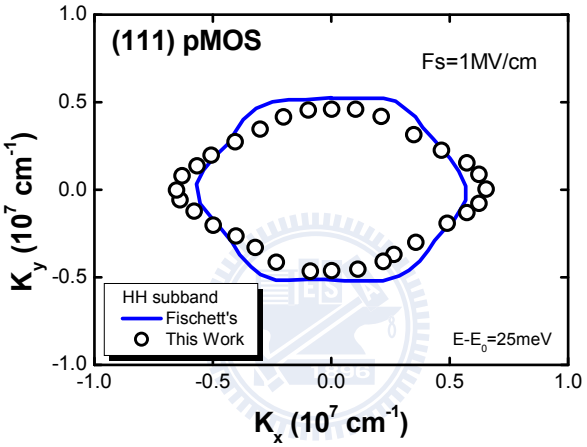

(c)

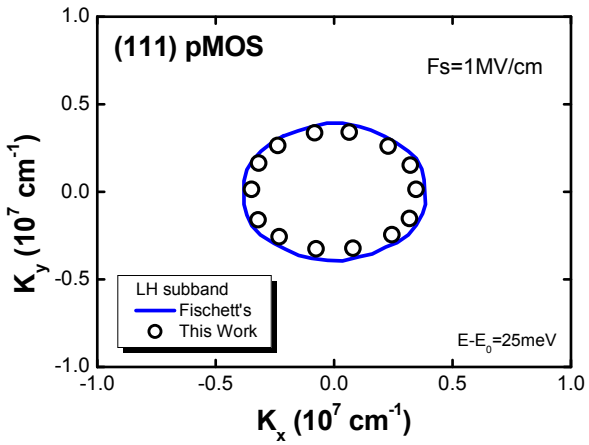

Figure 5.11. Subband energy (a) and equienergy lines (b) and (c) in the lowest –lying HH and SO subbands for the (111) surface compared with Fischetti's [3]. The doping concentration is 1×10^{17} cm^{-3} and temperature is 300 K. It notices that our subband energy is higher than Fischetti's [3] about 10meV.

(a)

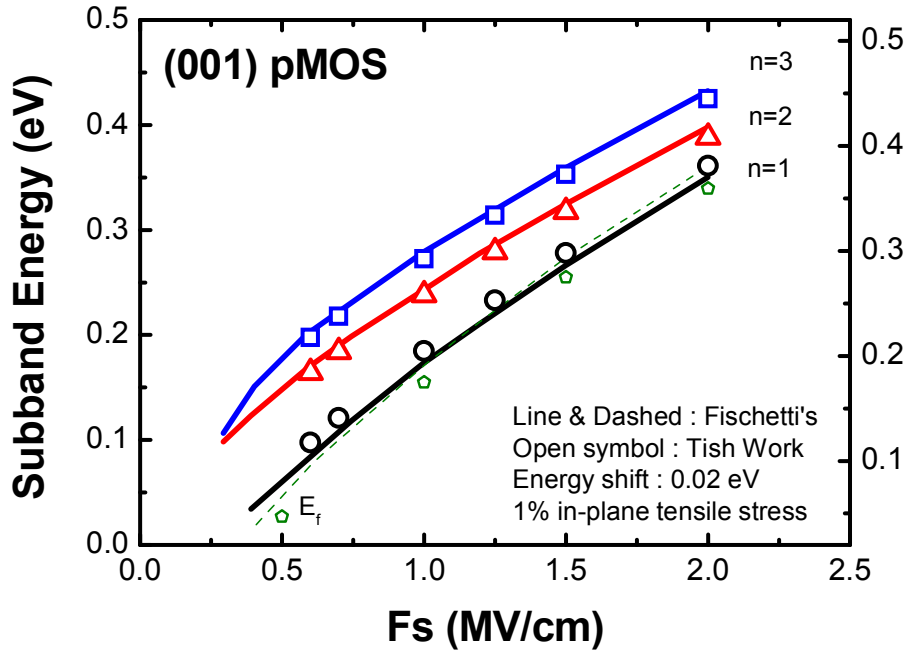

(b)

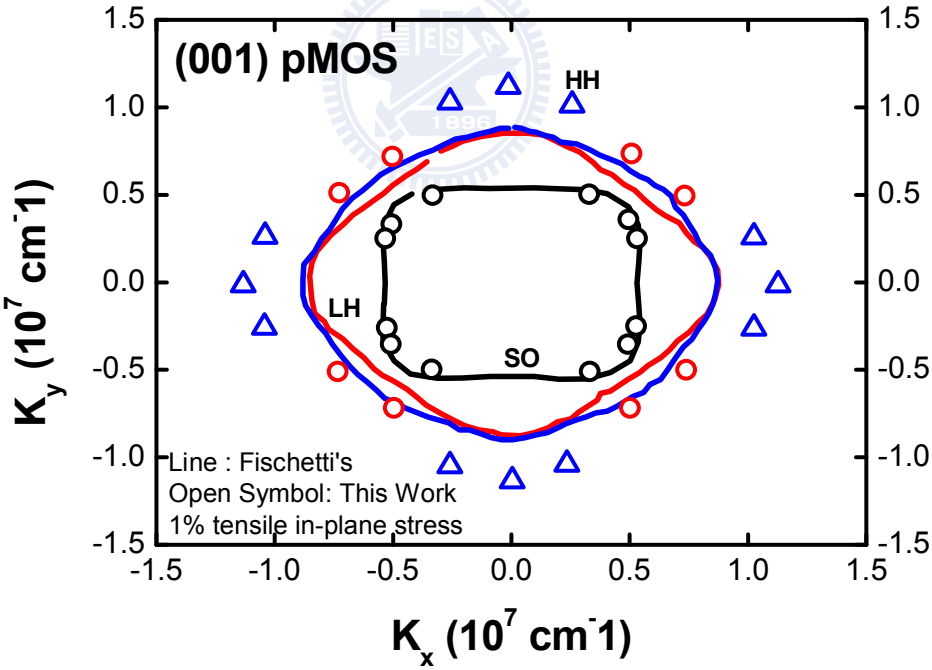

Figure 5.12. Energy of the subbands (a) and equienergu lines (b) in the lowest-lying HH, LH and SO subbands for the (100) surface with 1% of tensile in-plane stress applied on the (x,y) plane. It notices that our subband energy is higher than Fischetti's [3] about 20meV.

(a)

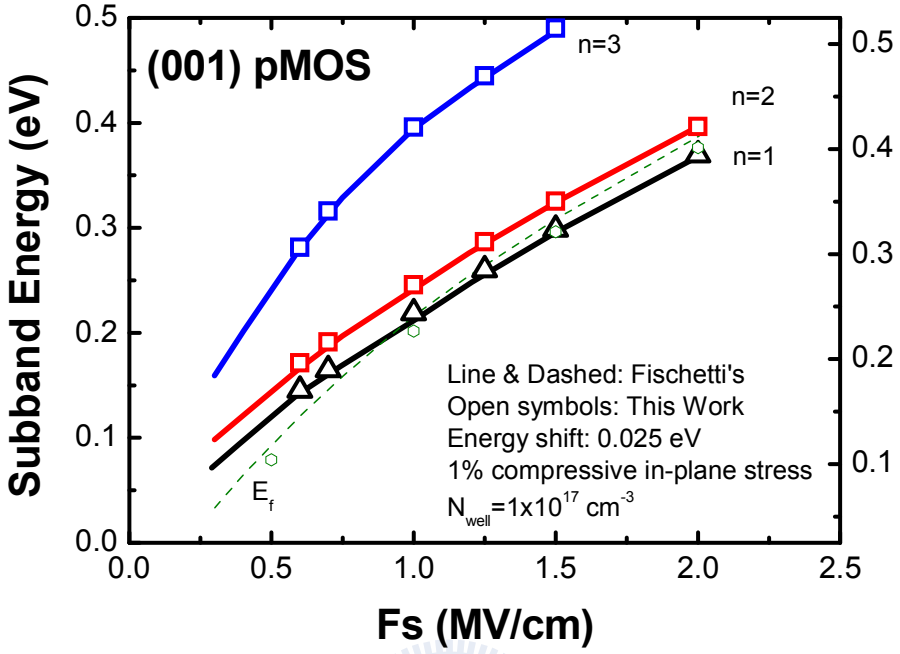

(b)

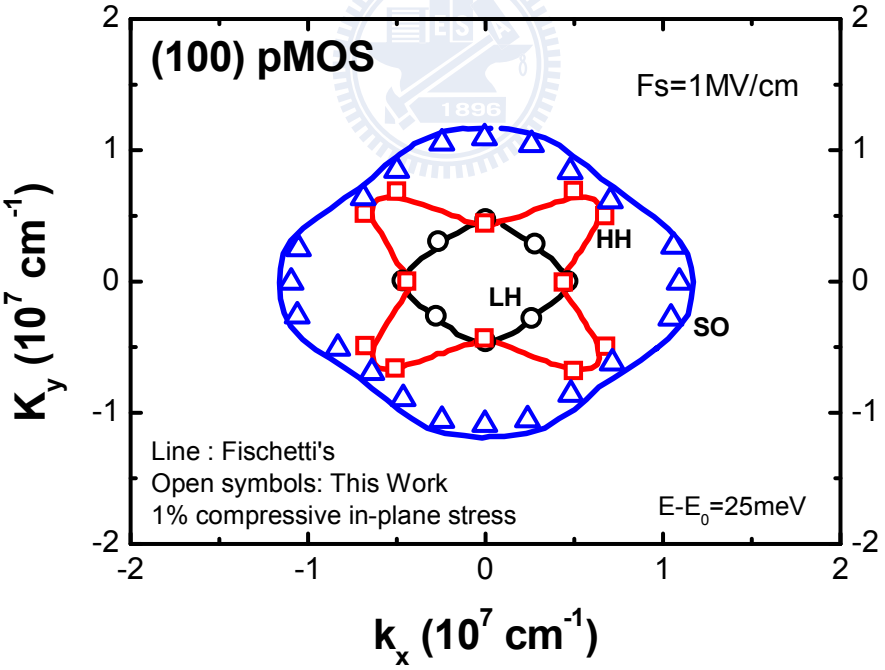

Figure 5.13. Energy of the subbands (a) and equienergu lines (b) in the lowest-lying HH, LH and SO subbands for the (100) surface with 1% of compressive in-plane stress applied on the (x,y) plane. It notices that our subband energy is higher than Fischetti's [3] about 25meV.

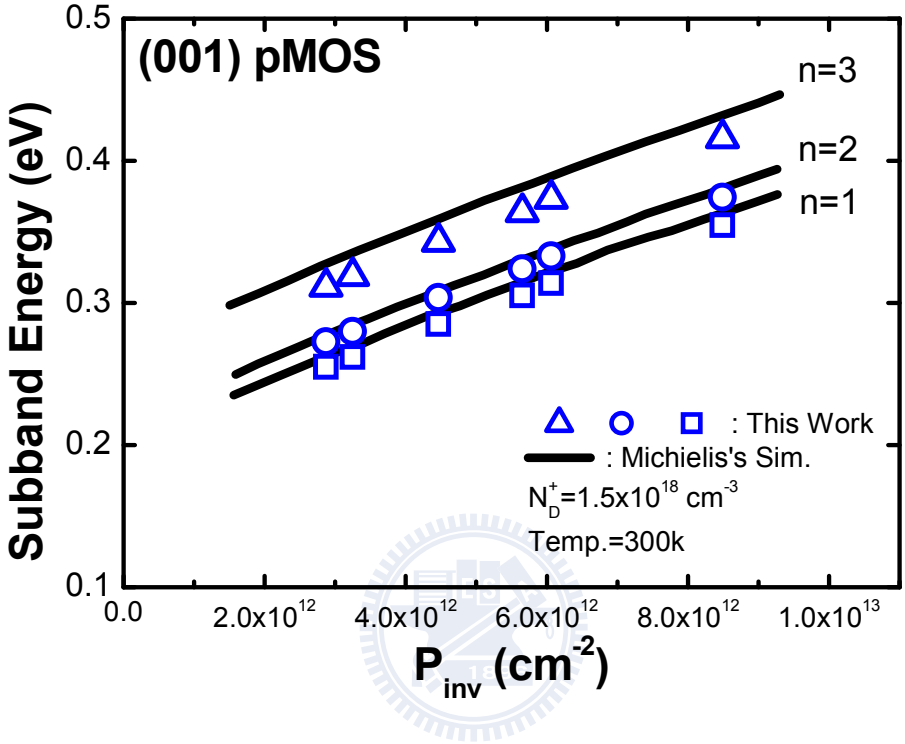

Figure 5.14. Energy of the subbands for the (001) surface by our new model compared with Michielis's simulation results [15].

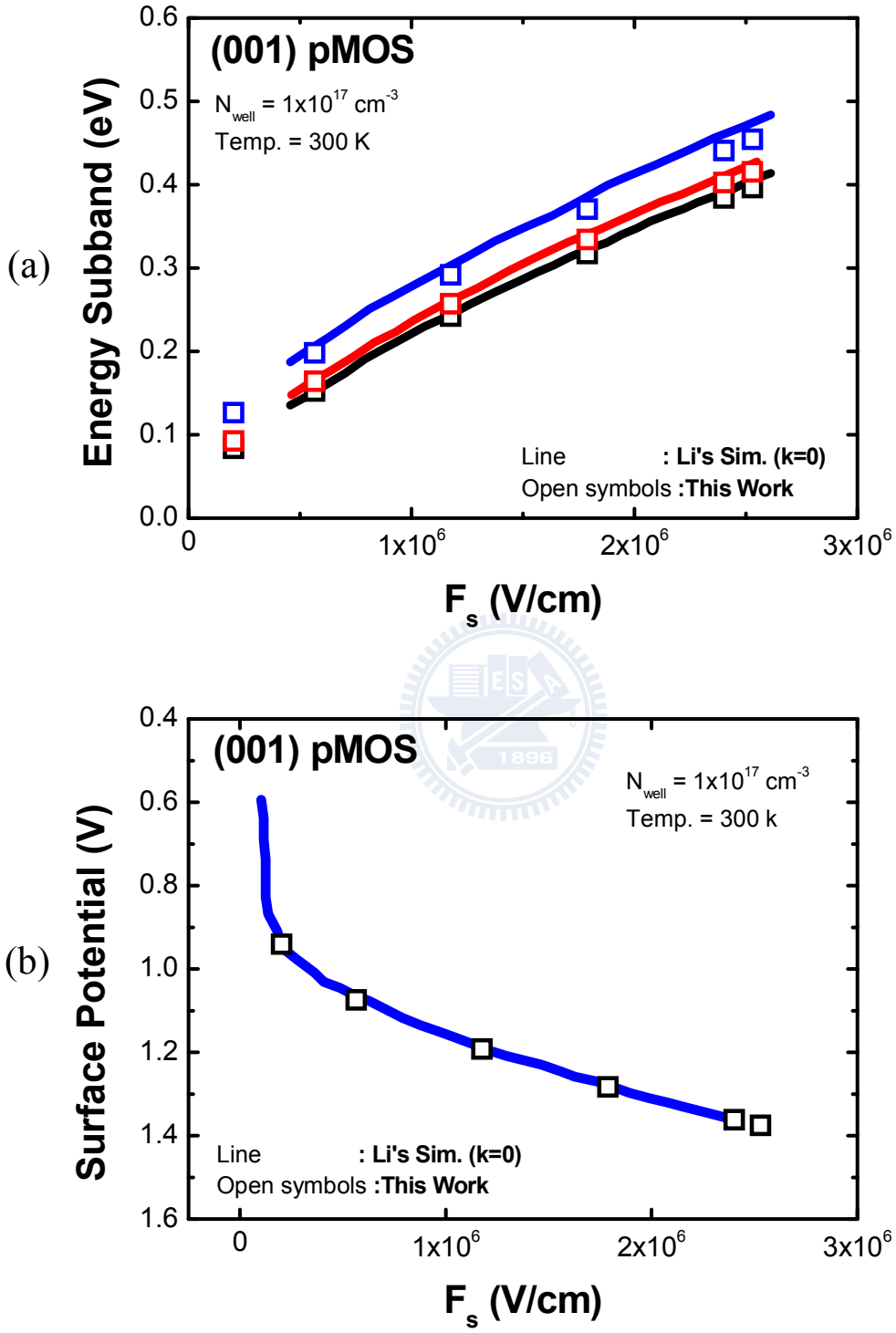

Figure 5.15. Subband energy (a) and surface potential versus electric field (b) for (001) surface in our new model compared with Li's simulated results [14].

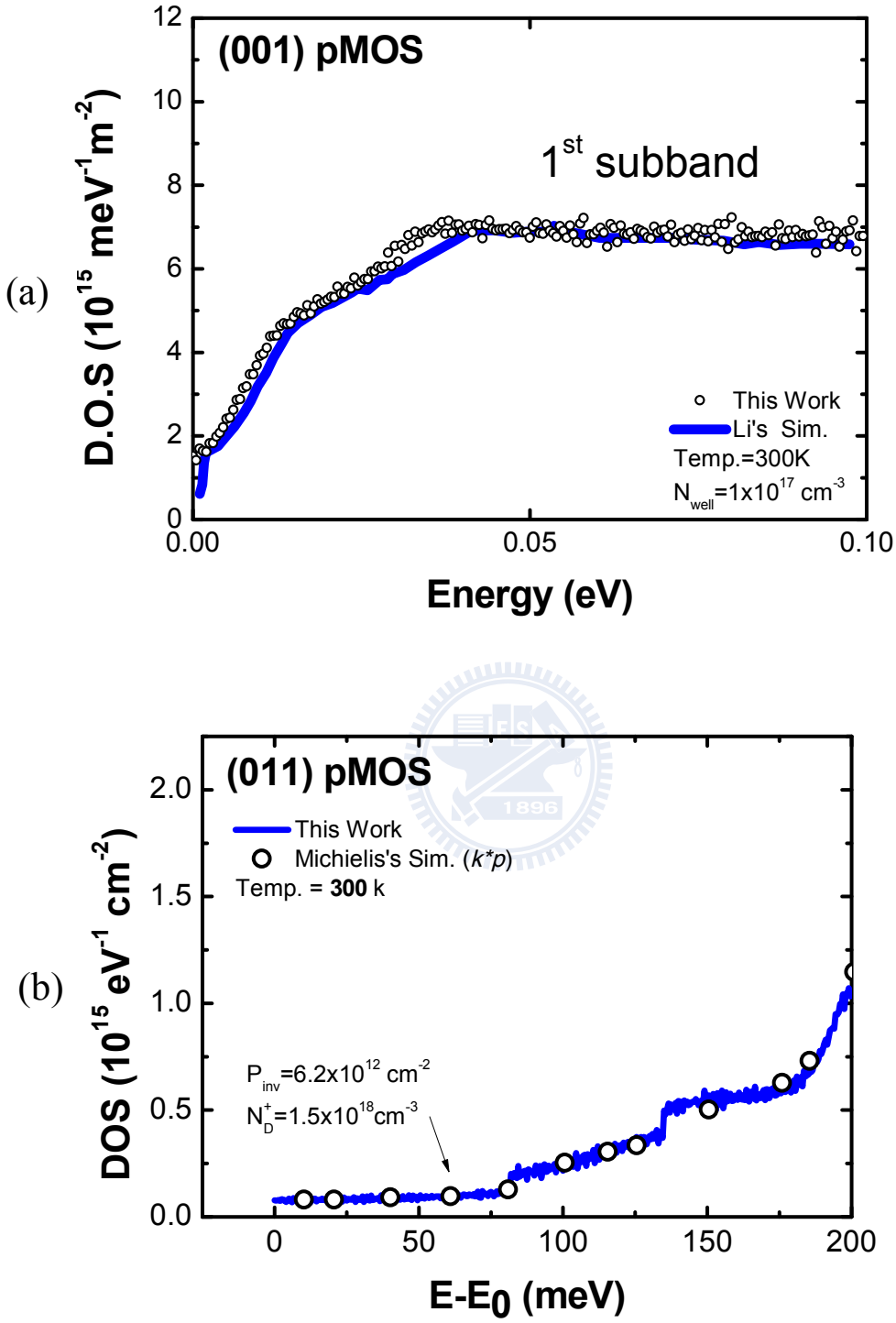

Figure 5.16. Density of states distribution for (a) (001) surface with 1st subband and (b) (110) surface. The former result is compared with Li's [14] and the latter is compared with Michielis's [15].

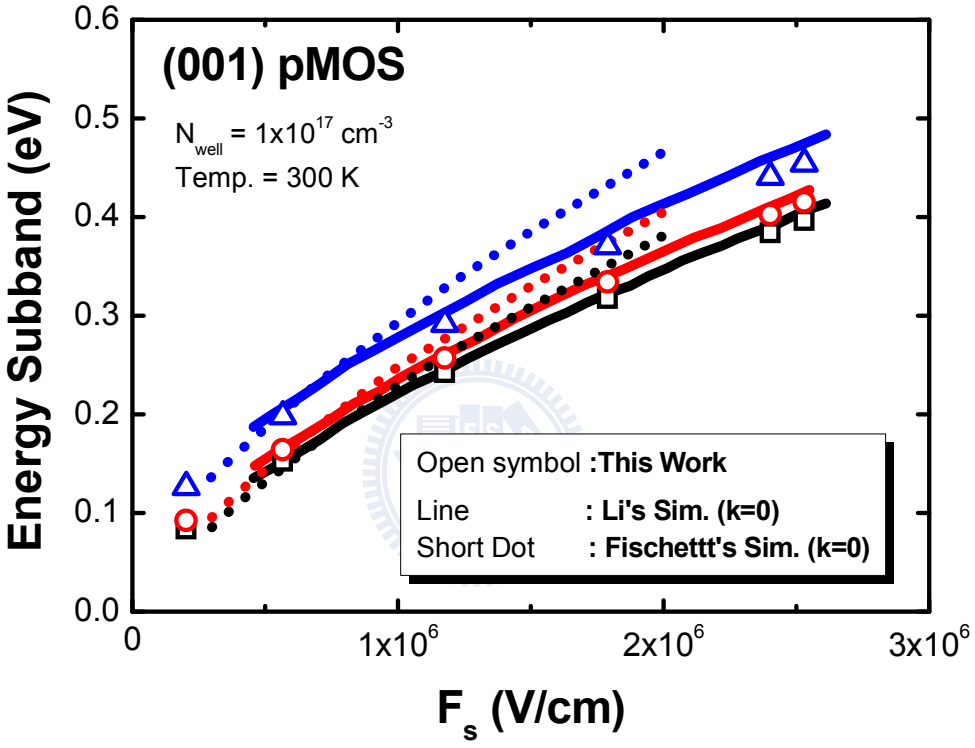

Figure 5.17. Comparison subband levels for three techniques: triangular potential approximation, self-consistent method, and this work.

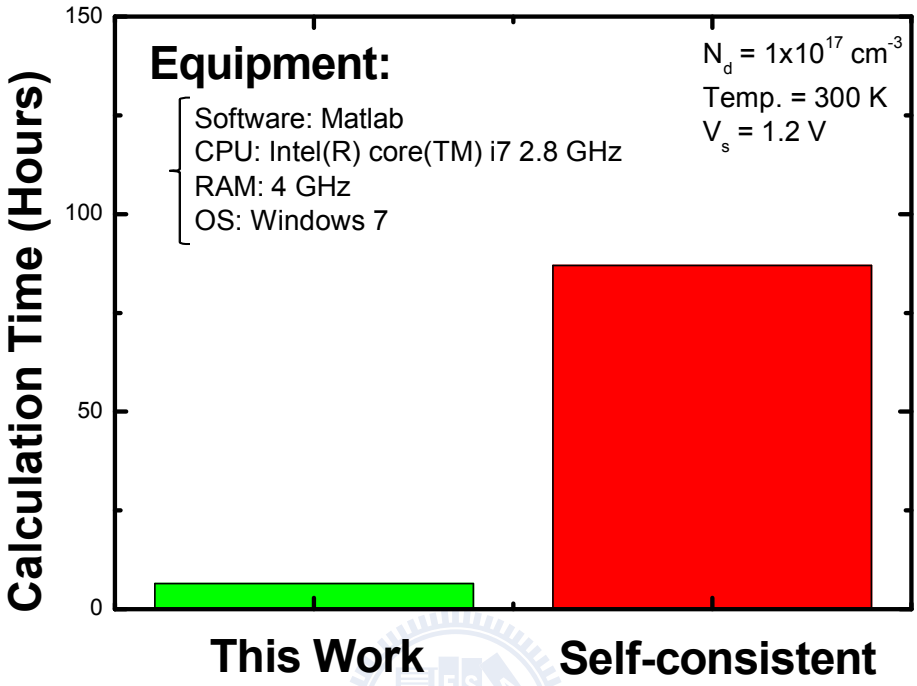

Figure 5.18. The calculation time compare this work with conventional self-consistent method.

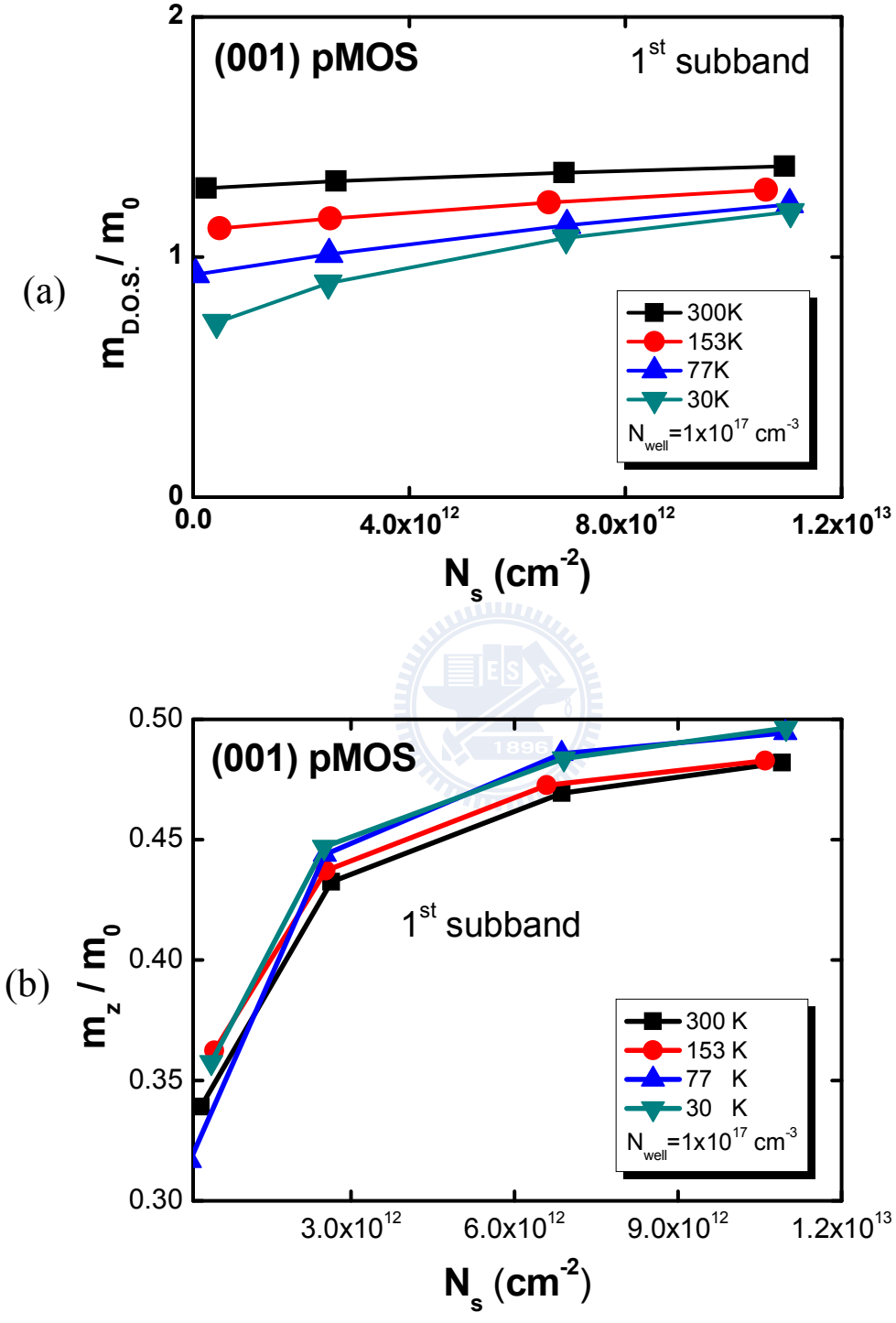

Figure 5.19. Density of states effective mass (a) and quantization effective mass (b) at different temperatures for the 1st subband. Substrate doping is 1×10^{17} cm^{-3}.

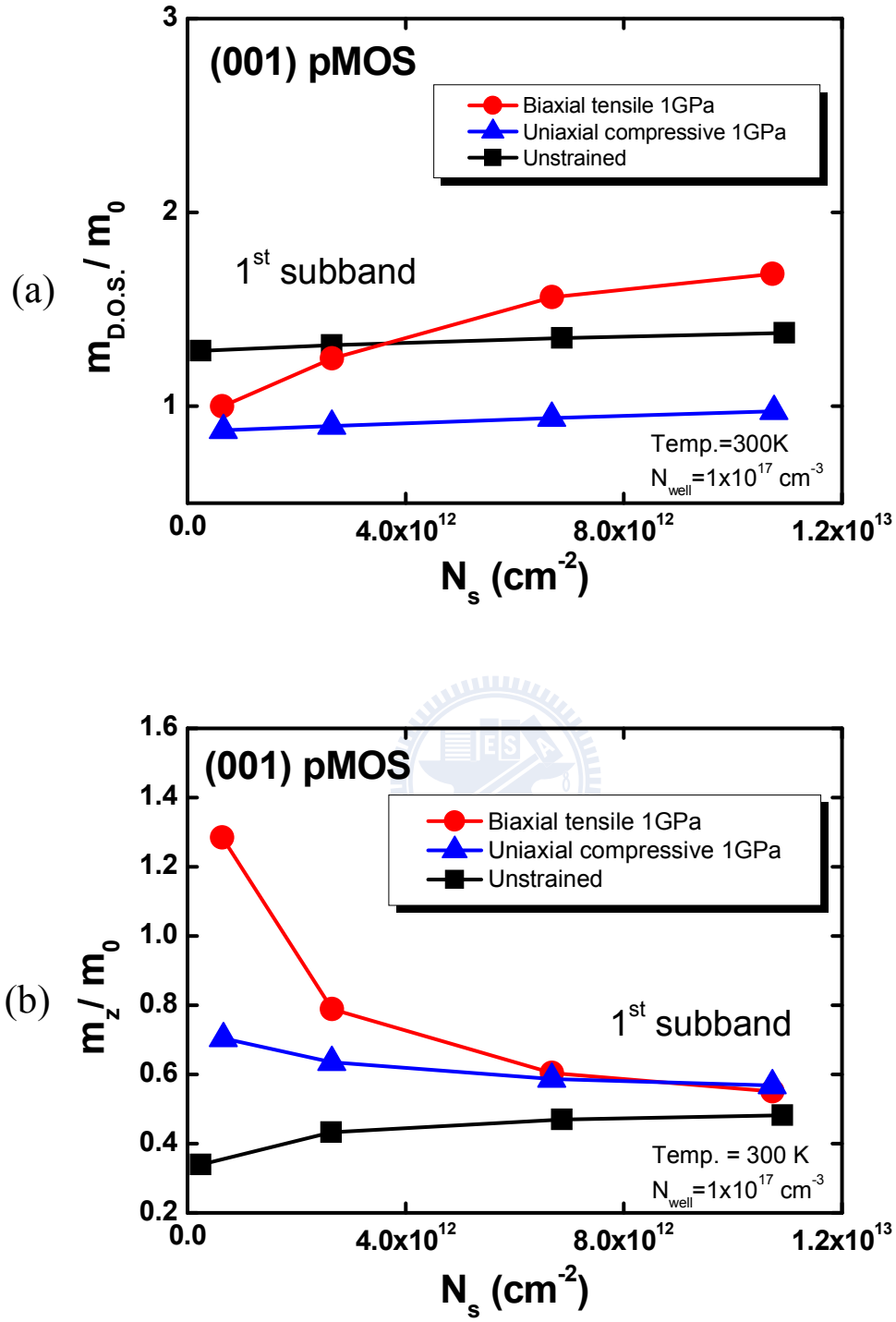

Figure 5.20. Density of states effective mass (a) and quantization effective mass (b) with biaxial tensile 1 GPa and uniaxial compressive 1G Pa for the 1st subband. Substrate doping is 1×10^{17} cm^{-3} and temperature is 300 K.

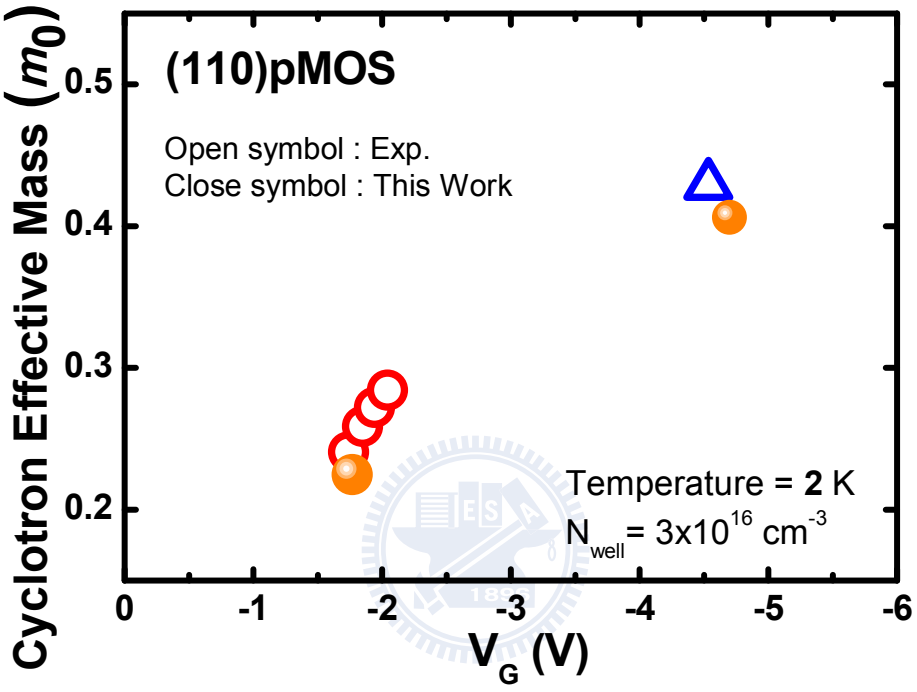

Figure 5.21. The simulation results and comparison with the experimental values by SdH oscillation analysis [5]. The temperature is 2 K, the substrate doping is 3×10^{16} cm^{-3} and the metal work function for aluminum is 4.26 eV.

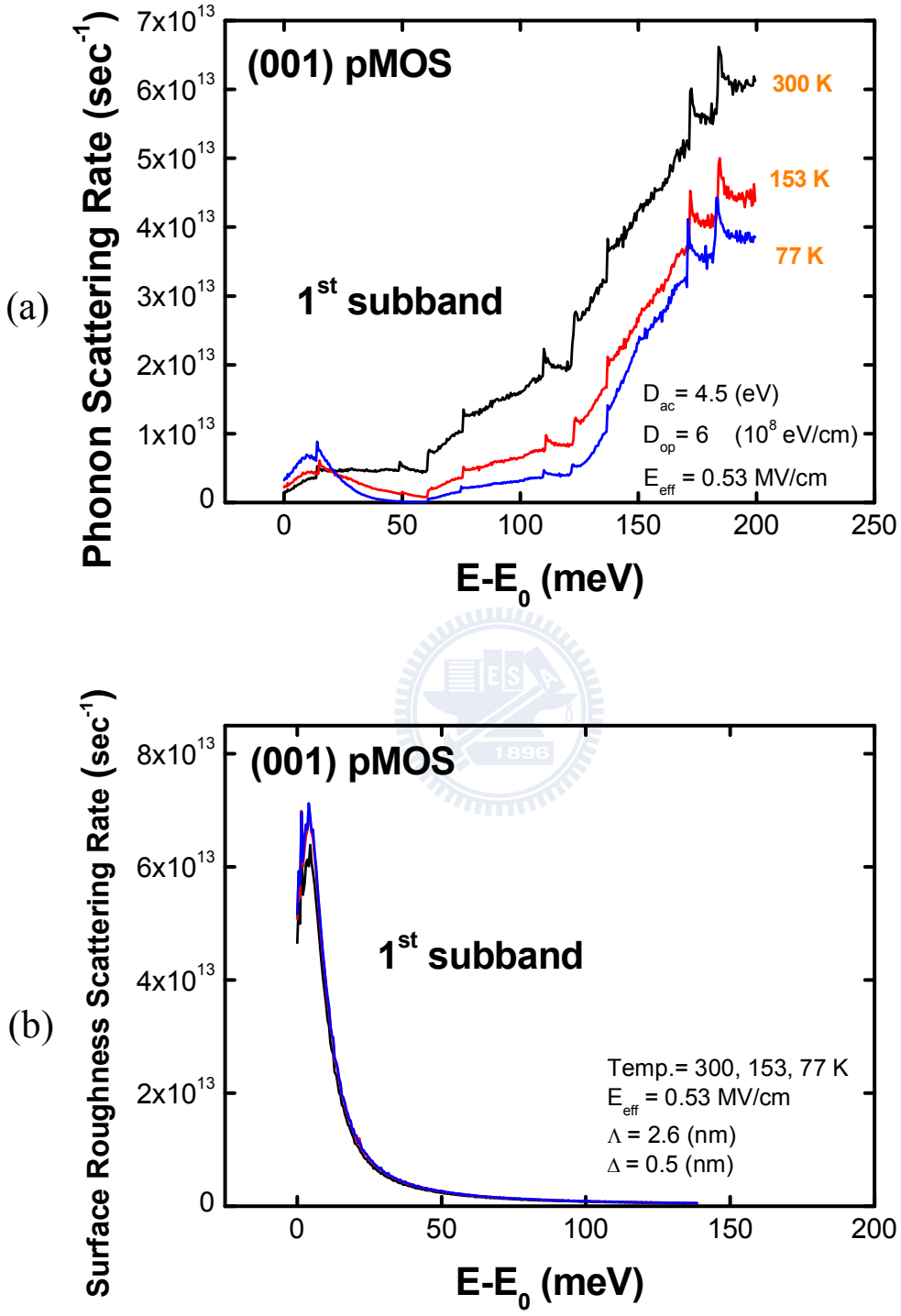

Figure 22. The phonon (a) and surface roughness (b) scattering rate for the 1st subband at different temperatures and the effective field is 0.5 MV/cm.

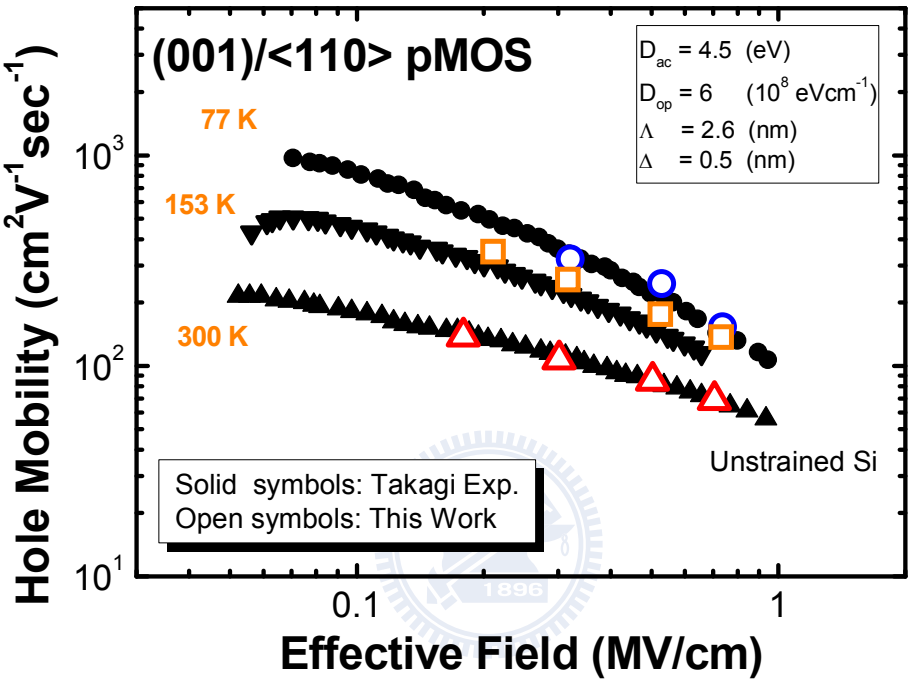

Figure 5.23. The simulation results by EMA and comparing with the experimental data of Takagi [6] for three different temperatures of 77K, 153K and 300K

Parameter	This Work	Thompson[2]	Fischetti[4]	Li[7]
γ_1	4.22	4.22		4.285
γ_2	0.39	0.39		0.339
γ_3	1.44	1.44		1.446
a (eV)	2.46	2.46	2.1	
b (eV)	-2.1	-2.1	-2.33	
d (eV)	-4.8	-4.8	-4.75	
Δ (eV)	0.044	0.044		0.044

Table I. Comparison of the used hole band parameters and deformation potentials for silicon.

Parameter	This work (001)	Fischetti[3],[4] (001) (011) (111)	Michielis[15] (001)	Oberhuber[20] (001)
Optical energy $\hbar\omega$ (meV)	61.2	61.2	61.2	61.2
Crystal density ρ (g/cm^3)	2.329	2.33		
Sound velocity $\boldsymbol{u_l}$ (m/s)	9040	9000		
Optical phonons $\boldsymbol{D}_{\text{op}}$ (10^8 eV/cm)	6	13.24	11.5	7.63
Acoustic phonons $\boldsymbol{D_{ac}}$ (eV)	4.5	7.12	5.6	5
Surface Roughness Λ (nm)	2.6	2.6	2.6	0.2
Surface Roughness Δ (nm)	0.5	0.4	0.55	0.5

Table II. Hole scattering and physical parameters for Si used in this work, along with the comparison with the values recently reported in the literature.